Université catholique de Louvain

École polytechnique de Louvain (EPL)

Modeling with Robotran the autonomous electrical taxi and pushback operations of an Airbus A320

Dissertation presented by
Stéphane QUINET

for obtaining the Master's degree in
Electro-mechanical Engineering *Option(s): Mechatronics*

Supervisor(s)
Paul FISETTE , Bruno DEHEZ

Reader(s)
Francis LABRIQUE, Matthieu DUPONCHEEL

Academic year 2016-2017

Acknowledgements

Before getting to the heart of this master thesis, I wish to take the time to thank the many people that supported me in this project of going back studying at 26 years old and making it possible to combine both my passion for flying and for acquiring new technical knowledge.

I would like to thank my master thesis supervisors, Pr. Paul Fisette and Pr. Bruno Dehez for their support and for the approval to work on this proposed subject. It was a chance to be supported by people with such an open-mindedness and eagerness to discover new technical fields. Their understanding of my challenging situation and their flexibility was greatly appreciated.

I would especially like to thank Nicolas Docquier for the many hours spent at correcting the Robotran-Simulink interface Windows version, my algorithms and for the countless advises that he provided all along the year. Thanks to the assisting staff of the department, Aubain Verlé, Olivier Lantsoght, Quentin Docquier for their technical inputs and support. Finally, thank you very much to UCL university staff for their understanding and their support during those 5 years.

After those 5 challenging years combining University and my airline pilot job, it is time to thank the most important person who makes all of this possible, my companion, Carole Aerts. She truly believed in the success of this uneasy undertaking since the first day. She supported all the difficult times and I could honestly say that I would not have passed through all this without her day-to-day support, motivation and determination.

A special thanks to my mother and my father as well as the rest of my family and friends for their support and continuous trust in my capacities. A special thank you to my father, who unbelievably, 40 years after his studies, could answer technical questions within a few minutes, on a variety of technical engineering subjects.

I wish to thank the other students too, friends I should say, for providing me with all the notes of the lectures I missed due to my one week-on one week-off scheduled pilot job and all the hours they took to explain the missed items.

Thanks to all my friends and colleagues who understood my situation and who supported me every day and every flying night. Special thanks to Jean-François de Bie and Frédéric Breuls for their help and last minute cockpit data and pictures.

Thanks to my employer and especially to the Brussels Branch staff, Peter Derom, Kathleen De Keukeleere, Marie-Hélène Cox, Alexandra Horvath, Pierre De Naeyer and Rony Palmans for their support during all those years. Thanks to Carl Moyson for his ground engineer advices. Thanks to CSD staff for schedule flexibility with a special thanks to Steve Adcock.

Contents

Abbreviations and symbols

- APU : Auxiliary power unit
- ATC : Air traffic control
- BSCU : Brake and Steering Control Unit
- CG : Center of Gravity
- DH : Decision Height
- DOF : Degree of Freedom
- DOW : Dry Operating Weight
- ICR : Instant center of rotation
- KTS : Knots, nautical miles per hour (1kts = 1.852 km/h = 0.514 m/s)
- LDG : Landing or landing gear
- LVP : Low Visibility Procedure
- MAC : Mean Aerodynamic Chord (see definitions)
- MTOW : Maximum Take-Off Weight
- NWS : Nose wheel steering
- PM : Permanent Magnet
- RVR : Runway Visual Range (see definitions)
- RWY : Runway
- TWY : taxiway
- ULD : Unit Load Device or aircraft containers
- VHF : Very High Frequency

Definitions :

- Aircraft : Airplane.
- Mean Aerodynamic Chord : The average distance between the leading and trailing edge of the wing.

- Nose Datum : On commercial aircraft, all positions are based on an aircraft reference point called the datum. It is most of the time positioned at the front end of the aircraft nose.
- Pushback (truck) : The truck pushing the aircraft out of its parking position. It is also used to tow an unused aircraft from one position to another on the airport (e.g. for parking space optimization or to bring it into the hangar).
- Runway Visual Range : visibility measured in the runway axis direction,
- Runway 25 : Runway axis aligned with the heading 250° in regard to the Magnetic North.
- Taxi (verb) : To follow the taxiway.
- Taxiway : The road between the runway and the gate/stand at the terminal.

List of Figures

List of Tables

Introduction

Nowadays, commercial flights are close to a full automation while several means of transport already made the move (e.g. metro, train). Civilian transport airplanes offer the possibility to fly in a fully automated mode from a few seconds after take-off to the exit of the runway - down to 60 knots- after landing. However, three flight sequences are not covered yet by an automated solution : the take-off, the taxi and the pushback.

While passenger traffic increased from a few million passengers in 1950 to 3.7 billions in 2016 at worldwide level [33, 34], this trend is expected to continue with forecasts ranging from 4.1% annual growth by 2034 (IATA) [35] to 4.5% by 2042 (ICAO) [36]. Besides passengers, freight traffic is also growing with an estimated 4.2% annual growth rate by 2042 [36]. To cope with this rising demand, airports expand their infrastructures where possible but most airports being nearly saturated and nearby cities, they firstly look at new ways to run their air activities.

Further, another concern for airports and aviation in general is to relentlessly enhance safety on the ground and in the air. When looking at detailed figures, we observe that the first source of accidents relates to the *runway safety*, which was responsible for more than 50 accidents in 2016 [37]. Combined with *ground safety* it represents about 2/3 of the accidents [37].

Finally, each year flights are delayed, cancelled or diverted to alternate airports because weather conditions are so bad that airports cannot ensure a safe taxi on the ground. This impacts global traffic and causes revenue losses, that could be avoided if taxiing was allowed in any weather conditions.

The subject of this work, being the automation of taxi and pushback, perfectly fits with this overall need for an optimized aircraft ground traffic sequencing at existing airports, via a better control of time spacing between planes. It also brings a potential answer to the other objectives like enhanced safety requirements, air traffic continuity in low visibility weather conditions and can even contribute to ecological concerns.

This work is a global approach of the subject and will give an overview of basic aviation notions, vehicles dynamics, 3D-modelling with Robotran, controls on speed, direction and electrical motors and finally, it will review several other operational impacts. It should be understood as a working base for future potential studies.

It's time to leave, please fasten your seat belts and prepare for take-off...
We wish you a very pleasant flight.

Chapter 1 : Fundamentals of aircraft ground operations

As a passenger on a commercial flight, you arrive at the airport via the *landside* part. This includes the road or railway station you took to reach the airport, the terminal where you need to check in and any other place like shops, restaurants or leisure areas where you can get to before being subject to a security control. The *landside* part of the airport can thus be accessed by anyone, being a passenger or not.

After security clearance, you get into the part of the airport called *airside*. This is a highly secured area of the airport, including again a series of shops, restaurants and lounges where you can walk while waiting for your flight as a passenger. More importantly, the airside also consists in all the activities and areas relating to airplane operations, where planes park, taxi, take off and land and where personnel members and crews operate a series of missions to run the airport.

In this chapter, we will focus on a number of aviation fundamentals to master in order to understand the developments done in this work. Therefore, we will introduce the organization set up at the airside, the way aircraft traffic is managed, the procedures applied in case of low visibility and two other notions which will be useful in the scope of this project.

1.1 Airport airside organization

The airside of any airport is divided into 3 main areas :

- **The Apron**, which refers to the area where aircraft[1] park. Parking stands are mostly foreseen around terminals but also exist on specific (bigger) platforms built further away.
- **The Runway**, which refers to the *road* where planes take-off and land and is used in both directions depending on the wind direction and the wind tolerance of the wings.
- **The Taxiway**, which refers to any path connecting the aprons with the runways. The taxiway is characterized by its yellow line on the ground, guiding pilots through the airport.

Each of these areas is under the supervision of dedicated air traffic controllers (ATC), having a specific radio frequency (VHF) and an exclusive call-sign. The call-signs for these 3 areas are respectively *Apron*, *Tower* and *Ground* but on most airports, the aprons and the taxiways are controlled on a single VHF frequency with the unique call-sign *Ground*. These call-signs are used by pilots to call out to controllers and to communicate with them (see section 1.2).

[1]Plural of aircraft = aircraft

1.1.1 Apron

Being the area where planes park, the apron is at the same time the place where most activities around the plane can take place. Many vehicles move in the apron within the aircraft close vicinity to accomplish several missions : refuelling, providing catering, servicing toilets or operating plane maintenance. This is without considering ground operation cars (e.g. going to check the runway state), crew and passenger buses or high loaders and tractors with dollies used to bring cargo containers and passenger luggage to the aircraft.

In brief, this area is very busy and needs to be carefully managed in order to avoid accidents. For that purpose, namely to avoid any unintended incursion of vehicles aforementioned when the aircraft is moving or has its engines running, a safe area is defined. This area is delimited by red lines painted on the tarmac (1.1) and a complementary sign is given by the red beacons - the red flashing lights at the top and the bottom of the airplane fuselage - which when switched on, indicate to the ground personnel that the aircraft has its engines running or is moving and, in other words, represents a potential hazard (Figure 1.2). In this latter case, no vehicle nor person is allowed to enter the safe area.

Figure 1.1: B777 surrounded by ground equipment. The dollies with containers are placed behind the safety area red limit lines[1]

Figure 1.2: B787 beacons warn ground crews that the aircraft is under motion and/or taht engines are running [1]

1.1.2 Runway

Used by planes to take off and land, each runway has intrinsic characteristics defined when cast which determine the types of aircraft that will be welcomed on it. Both the type of floor and the length of the runway define which planes can use it. For very light aircraft (propeller aircraft), grass or soil is sufficient to support the plane and the runway length ranges from 600m to 1km. For jet aircraft, asphalt or concrete is used to cover the ground and these aircraft require average runway lengths of 2,5 to 3,5km.

To reach the runway or to vacate it, aircraft need to follow taxiways. As for all movements on the airport, a clearance needs to be granted by the *Tower* for the aircraft to be authorized to enter the runway. In the meantime, the plane waits at a specific place on the taxiway called the *holding point*. To confirm the oral answer of the controller and avoid runway incursions potentially resulting in some fatal accidents, a red line of directional lights has been installed at most airports. When illuminated, pilots cannot cross them, when they disappear, this means they got the authorization to proceed.

Some specific procedures need to be applied to get to the runway in case of low visibility weather (i.e. fog, mist). In these situations, the holding point is moved backwards to a point which is more remote from the runway, the so-called *CAT II/III Holding point*. This is a safety margin but also a way to avoid interferences with the radio navigation system guiding the airplane to the ground, that has to provide high accuracy in such weather conditions for the ILS signal (i.e. Instrument landing system signals VHF). More information will be provided in section 1.2.3.

In Figure 1.3, the runway is at the top right corner. You can observe several lines of red lights (detailed design shown in Figure 1.4) which inform about clearance (not ok) status.

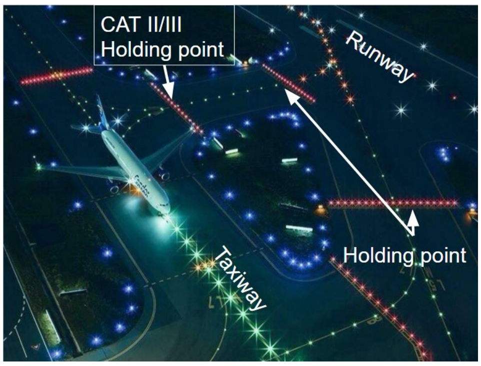

Figure 1.3: Runway protected by red light lines on the normal and high speed taxiways [2]

Figure 1.4: Ground directional lights installed at holding points, on the taxiway. [2]

1.1.3 Taxiway

All taxiways are marked by continuous yellow central line, which allows to easily recognize them. This yellow line is the visual indication to pilots to guide them on the ground, letting the nose wheel travel on it. At regular intervals, green directional lights are placed on this central line to help pilots seeing it at night or in low visibility weather conditions. Furthermore, the boundaries of the taxiways are illuminated by blue lights as you can see in Figure 1.3.

As explained in the previous point (4.1.2) taxiways guide pilots to and from runways. Those are either perpendicular to the runway or secant with an angle of about 45°. Pilots mostly use perpendicular 90° taxiways to take off, at low speed (max. 15 knots). However, secant 45° taxiways are often used when landing, to make a quicker runway exit (max. 50 knots allowed). This is a genuine potential lever of time management on the ground.

1.2 Traffic management

All movements on an airport are strictly codified. Several very detailed procedures need to be followed, in order to reach the most optimized, safe and clear behaviors from planes, vehicles and people involved on the ground. These procedures, implying a succession of clearances, have a main impact on aircraft traffic sequencing, namely distances and time to leave between planes, and the capacity of an airport to welcome aircraft. Let us have a look at these procedures.

1.2.1 Departure sequence procedure

In commercial operations, the first clearance to request at ATC on the *Delivery* frequency relates to the authorization to leave the stand. When this first clearance is granted, pilots contact the *Ground* or *Apron* frequency to receive a *push back clearance*. Once obtained, they swithc the beacons (Figure 1.2) on and the aircraft is pushed out of the apron area by the push back truck onto the taxiway (Figure 1.5). In the meantime, pilots start the aircraft engines.

Once on the taxiway with the engines running and the push-back truck disconnected, pilots contact the *Ground* frequency to obtain the taxi clearance. During this step, they receive the route to follow on the taxiway in order to reach the active take-off runway. This clearance is a sequence of letters identifying the different taxiways, visible on the airport chart in Figure 1.6). For a better understanding through the VHF radio's, those letters are pronounced according to the aviation alphabet [38] (e.g. from stand 408 in London Heathrow in Figure 1.6, "T-S-SB3": "Proceed via Tango, Sierra, Sierra-Bravo-3 to hold short from runway 27 Left"). In case of converging traffic, one aircraft will give way to the other as instructed by ATC. It will stop at the clearance limit, which can be at the holding point of a runway or anywhere on the airport in case of traffic sequencing (e.g. "Hold short of taxiway Sierra and give way to Boeing 737 of British Airways").

The pilots then follow the taxiways, being powered by the engines which are continuously pushing the aircraft forward (i.e. with the idle thrust). The brakes installed on the main gear wheels are used to slow down the aircraft when needed and the nose wheel steering is employed to steer the plane. Let us now deep-dive into the ways to steer a plane on the ground, which we will need to know for the development of our mechanical part in this work.

Figure 1.5: two technologies of push-back trucks : pushing with a tow-bar (top) or lifting the aircraft nose wheel (bottom) [1]

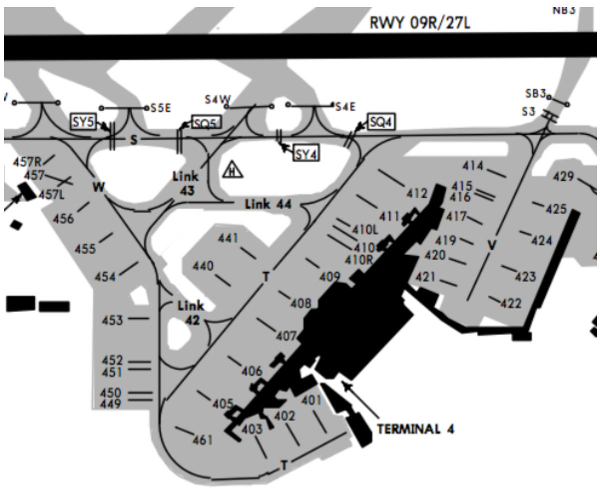

Figure 1.6: Part of London Heathrow Jeppesen chart used by pilots [3]

1.2.2 Arrival sequence procedure

To be authorized to land, a clearance needs to be obtained from the *Tower* frequency. If it is not granted, pilots need to turn around following specific pre-defined routes. Once on the ground just after landing, a plane vacates the runway via a high speed taxiway and pilots switch from the *Tower* to the *Ground* radio frequency. The air traffic controller then provides the taxi clearance and indicates all the taxiways pilots have to follow to reach their stand.

At the stand, a marshaller (i.e. an airport employee who guides the aircraft into the stand with his wands-handheld illuminated beacons) guides the pilot up to the nose wheel stop position that pilots cannot see themselves (i.e. the nose wheel is most of the time a few meters behind the cockpit). Nowadays, electronic marshalling devices display the distance remaining to the stop position on a screen as well as a lateral guidance information.

1.2.3 Low Visibility Procedure - LVP Operations

In this section, we will see that procedures are adapted when wheather conditions deteriorate, which immediately affect aircraft traffic flow on the airport. Both the airport infrastructure and the crew training determine the possibility to carry on airline activity in such circumstances.

By nature, and coming from the roots of aviation, flying can be done visually which means, without any guidance instrument. This can be done under very good weather conditions concerning the ceiling (i.e. the cloud base elevation above an airport) and the visibility. More specifically, nowadays, visual flying is authorized when visibility is higher than 5 km and there is more than 1500 feet of ceiling. Even if less applicable to commercial operations, small and leisure aviation use visual flying a lot.

When weather conditions fall down and indicators drop below these minimum thresholds, pilots have to be qualified to do both the approach and the landing - manually or automatically - with the help of an instrument guidance system (i.e. pilots need to be instrument rated *IR*). This kind of approach is referred as *CAT I* and is the most used in commercial operations. A ***CAT I* approach** can be started with a minimum visibility or Runway Visual Range (RVR) of 550m and has to be stopped in any case if the runway is not in sight at 200 feet, namely when the ceiling is below that height. This height is called the *decision height (DH)*, where pilots need to make the decision to land or not. If the approach has to be aborted, pilots perform a *go-around* and climb back at a specific height where they follow a determined track, which can bring back to the airport within a given time frame (weather conditions could have improved in the meantime) or divert to an alternate airport .

Guidance instrument: Let us now look at the guidance instruments used in such poor weather conditions (or at night, when visual flying is of course impossible). The most used guidance system is called *ILS*, standing for Instrument Landing System. This system provides a track and a slope guidance down to the runway. The track signal or *LOC* signal is sent from the localiser antenna located at the end of the runway. The slope signal or *Glide* signal is sent from an antenna placed abeam the touchdown zone of the runway. The track signal is displayed to the pilots on their primary flight display (PFD) via an horizontal and a vertical magenta diamond moving on a fixed doted white scale (e.g. in Figure 1.7, on the PFD instrument we can see that the aircraft is on track but a little bit below the glide slope, the magenta diamond representing the position of the slope). The visual indication of the slope is provided by another equipment called *PAPI* for *Precision Approach Path Indication* build with 2x4 directional lights (i.e. a white and a red light for each of the four positions orientated at different angles from the ground). Four red lights means too low, Four white lights means too high and two red-two white means on the glide. The PAPI system is visible in Figure 1.8 on the left hand side of the runway.

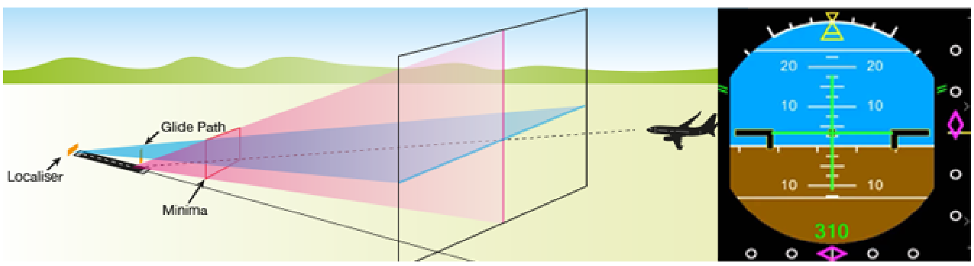

Figure 1.7: ILS signal schematic and the PFD instrument seen by pilots with the localiser and glide references show through both magenta diamonds [4]

Sometimes the weather is not even good enough for a successful CAT I approach (e.g. heavy fog). In that case a **fully automated approach from *CAT II/CAT III*** has to be performed. The difference with CAT I approaches is that even the flare (inflection point created by going slightly up just before touching the runway) needs to be done automatically, which is not the case in CAT I. To be able to proceed to CAT II/III approaches, there are specific requirements :

- The aircraft needs to be equipped with automatic landing capabilities
- The crew - captain and co-pilot - needs a specific qualification. This in order to be able to take over commands at anytime if a system fails
- The airport needs to have a precise landing system (ILS) and a specific approach light system (i.e. approach lights forming a carpet in front of the runway like in Figure 1.8)
- The airport needs to have bigger protection zones around the runway in order to avoid ILS signal distortions, in other words, a second holding-point more distant from the runway than the normal holding-point (i.e. for CAT I condition). For that reason, this second holding-point is also referred as to *CAT II/CAT III holding point*, visible in Figure 1.3.

In these CAT II/ III fully automated approaches, we still distinguish 4 different types, which differ in the accuracy and complexity of their related aircraft systems. Going from the lowest to the highest requirements, 3 approaches are used today : CAT II , CAT IIIA and CAT IIIB. As explained in CAT I approaches, CAT II/ III approaches can start with a proper RVR value and continued until the DH, minimums varying according to the type of approach (see Table 1.1). The last approach category CAT IIIC - not available yet - is defined by ICAO as a *precision instrument approach and landing with no DH and no runway visual range limitations* [32]. This approach is purely theoretical as even if it can already be applied in the air, once on the ground, pilots have to taxi their aircraft manually to the terminal. In a limit case (no visibility), they are not able to follow the taxiway central line to reach their stand, as the cockpit of a commercial aircraft is at 3 to 12m above the ground. This is why aircraft need a minimum visibility to land.

Besides categorized approaches and specific related trainings, some additional safety measures are applied when low visibility is observed. For example, when visibility is below 400m (LVP operation), an increased distance is foreseen and applied between aircraft on the ground. One aircraft per taxiway section is allowed to avoid ground collisions. These safety measures drastically increase delays. In normal circumstances, the separation between aircraft behind each other is insured visually by the pilots. Unfortunately, it is sometimes difficult to estimate visually the distance between the wing tip and the obstacles. There are famous ground collisions linked to that issue (e.g. Air France A380 plane collides with Delta CRJ at JFK - 12/04/2011 - video [39]).

Approach	minimum DH (feet)	minimum RVR (m)
CAT I	200	550
CAT II	100	300
CAT IIIA	no DH	200
CAT IIIB	no DH	75
CAT IIIC	**no DH**	**no RVR**

Table 1.1: EASA Approach criteria based on ICAO Annex6, 9^{th} edition, July 2010 [32]

Figure 1.8: Runway approach lights approved for LVP operations. [1]

1.3 The nose wheel steering

There are three different ways to orientate the nose wheel. The schematic is visible in Figure A.1

1. Pilots can use **the hand steering wheels** (i.e. each of them have an individual handle placed at each side of the cockpit as seen in Figure 1.12). On earlier aircraft models, a pulley system was installed as torque multiplier between the handle and the nose wheel steering actuator. Nowadays with the fly-by-wire system (i.e. replacement of mechanical transmissions and cables by electrical wires for weight saving) [40], an electrical *black box* called Brake and Steering Control Unit (BSCU) is used to control the nose wheel steering angle through a hydraulic actuating cylinder. When using the hand wheels steering, the nose wheel can be rotated up to an angle of 75°.[5]

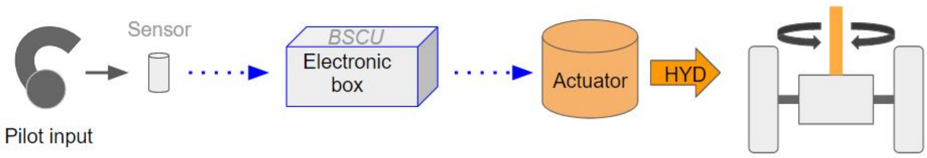

Figure 1.9: From pilot input on the steering wheel to the nose gear motion

2. Pilots can also use **the rudder feet pedals**. When pushing on these pedals, they induce a motion of the rudder (i.e. control surface on the vertical area of the tail to control the rotation around the yaw axis) but also a very small rotation of the nose wheel. With a full rudder application, the nose wheel steering can reach a maximum rotation angle of 6°.[5] This is thus not used solely to direct the plane but as a complementary help in certain circumstances.

3. A third way to steer the aircraft is used **during push-back operations**. In this case, pilots are not controlling the direction but the guidance is rather done by a push-back team member. Indeed, the plane also needs to be guided when leaving its stand and being pushed back to the taxiway. In that case, **the steering system is deactivated** and the free nose wheel is then controlled by the push-back truck position in respect to the aircraft.

Concretely, the deactivation is initiated via a lever on the towing electrical box, placed on the nose landing gear. This electrical box informs the BSCU about the deactivation. The ground crew (i.e. the push-back team member which keeps continuous radio contact with the cockpit crew during the push-back) blocks the lever in the towing position with a safety pin until the push-back is completed (i.e. the lever is moved as shown in Figure 1.10 to align the 2 holes marked by the blue squares through which the safety pin will be inserted). Before the taxi, once the push-back truck is disconnected and the aircraft is ready for taxi, the ground crew shows the safety pin to the pilots to ensure them that the steering system is back in the active mode.

In this deactivation mode, the nose wheel can be turned up to an angle of 95°.[5]

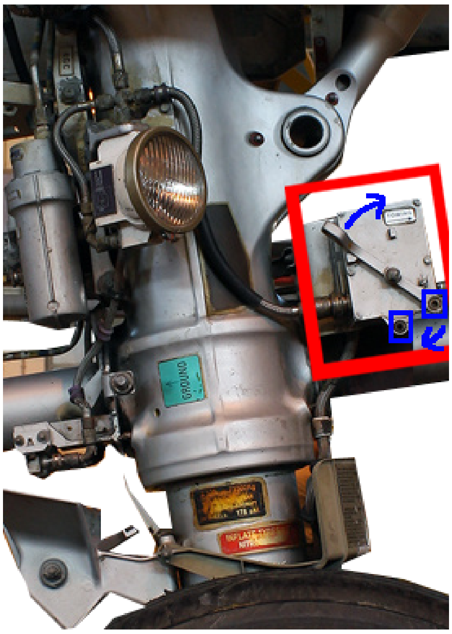

Figure 1.10: Steering system deactivation electrical box and its lever [1]

The angle values stated in these 3 situations are applicable for the Airbus A320 and are a function of the ground speed and the origin of the input signal (i.e. pilot's hand wheels or rudder pedals) as illustrated in Figure 1.11. An electrical control eases the implementation of such functions on A320 to avoid an increase in mechanical stress with speed.

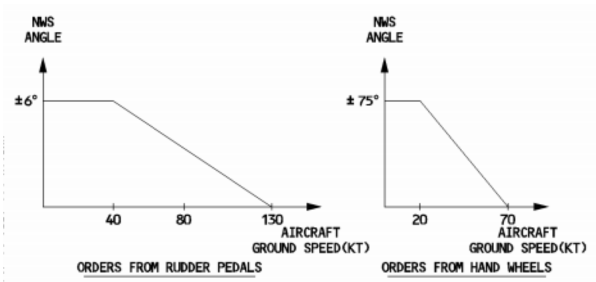

Figure 1.11: A320 nose wheel steering angle limit functions [5]

Figure 1.12: A320 hand wheel steering [6]

1.4 Deicing

In this section, we are going to introduce a very specific subject, that as you will see in chapter 8, could have a very useful role in our work.

During the winter, snow or ice can accumulate on the wings and on the fuselage of the aircraft. This accumulation has a double impact on climb/flight performance : it increases the weight of the aircraft and it modifies the shape of the wing. For that purpose, a deicing with or without anti-icing has to be performed [41]. The deicing principle is to remove the accumulation with a warm fluid (i.e. mix of water and glycol) and anti-icing is to protect the surface for a certain period of time, the holdover time (HOT) [42]. The HOT varies with the outside temperature, the type and the rate of precipitation and the type of fluid used. Tables are used by pilots to see how many minutes they have between the end of the deicing process and the take-off. If the HOT is passed, a new deicing has to be performed.

This deicing process (Figure 1.13) is either performed on the stand before push back or just before take-off on a special platform close to the take-off runway (Figure 1.14). This platform will be particularly interesting later on in this thesis, let us keep it in mind.

Figure 1.13: B777 on the deicing platform [7]

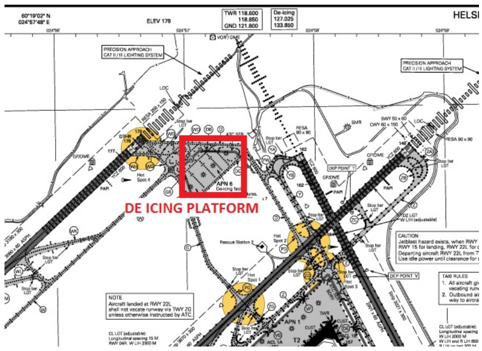

Figure 1.14: Deicing platform at Helsinki, close to runway 22R holding point [8]

1.5 APU engine start

On the parking spot, aircraft electrical systems are powered by an external generator, the so-called *ground power*. Before to be pushed out of the stand, the pilots start an auxiliary power unit (APU) which is a small jet engine placed in the tail of the aircraft (Figure 1.15). The main characteristic of this jet engine is that its reduced size permits a start on batteries. Once started, it powers the aircraft electrically and supplies hot air to the air conditioning unit. Thus, the *ground power* can be disconnected.

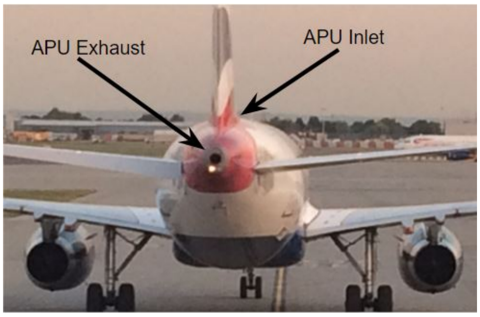

Figure 1.15: APU inlet and exhaust: A320

During the pushback, the air conditioning is stopped. The air provided by the APU has to be used to start the main engines. Indeed, those ones are too large to be started on batteries. Once all the engines are running, the APU is switched off. The air conditioning is switched on again, but this time the air is provided by the engines.

1.6 The reasons for an automated taxi and pushback integrated system

The main objective of this automated taxi and pushback integrated system is to improve the aircraft capabilities in low visibility operations, e.g. to be able to operate CAT IIIC approaches, and to reduce aircraft separation on ground.

Other non negligible positive safety, economical and ecological aspects have to be highlighted:

1. Better traffic flow management on the ground due to precise taxi timing estimation
2. Reduction of the waiting time at the holding point with the engines running
3. Cost and delay reduction by the suppression of push back trucks
4. Safety improvement and ground collision incidents or accidents reduction
5. Reduced workload for pilots, e.g. possibility to start engines during the taxi (in the case of electrical taxi system)

As for in-flight autopilots, this system should be constantly monitored and easily deactivated by pilots in case of unattended behavior. It is only an additional tool to be used by the crew to reduce workload and improve safety, operational performances and fuel saving.

Chapter 2 : Fundamentals of Vehicle Dynamics

2.1 Objectives of Vehicle Dynamics

The main objective of Vehicle Dynamics is to analyze the dynamical behavior of ground vehicles. This can be done with several objectives, among which improving the performance of vehicles, their stability, their safety and the comfort they can offer to their passengers.

Manufacturers typically define the required levels or thresholds to reach on such criteria. To achieve this, they notably work on the geometry of some parts of the vehicle, adapt the stiffness and damping coefficient of the suspensions, change the position of the centres of gravity, the position of the wheels and adjust their orientation.

Indeed, when the dynamic analysis of a car in quasi-static equilibrium is performed (e.g. in a constant radius turn at constant speed), the mass transfer, the resulting forces, the vibrations and the stability can be closely observed. In a second phase, their values are compared with the ones expected (targets) and corrective actions are taken to compensate when necessary.

In short, all these engineering analyses already allowed great enhancements and continue to largely improve the efficiency, performance and safety of ground vehicle operations. They also are the roots of automated systems developed for vehicles such as aircraft (auto-brakes and anti-skid system illustrated in figure 2.1) or for vehicles most of us drive every day (e.g. ABS, ESP illustrated in figure 2.2, Cruise control, Electronic brake systems, etc...).

Figure 2.1: Aircraft autobrake selector equivalent to ABS [9]

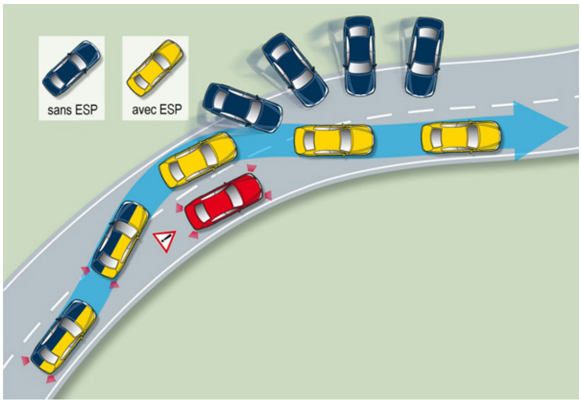

Figure 2.2: ESP behavior studied through vehicle dynamics analysis [10]

2.2 Ground vehicle definitions and characteristics

In this part of the chapter, the basic mechanical definitions and concepts required to understand the upcoming sections, applied to aircraft, will be introduced.

2.2.1 Axes, angles and characteristic dimensions

As the aircraft has 6 degrees of freedom, i.e. 3 translations and 3 rotations, three axes exist. These are set up within the scope of this work as drawn in figure 2.3.

The roll axis : A motion around x axis creates a so-called roll angle ϕ. During ground operations, namely pushback and taxi, the variation of ϕ - linked to the turns taken - is the one passengers feel the most, the intensity depending on the main gear suspensions characteristics.

The pitch axis : A motion around y axis induces a so-called pitch angle γ which is influenced by the nose wheel suspension. When the aircraft accelerates, an upward variation of the pitch is observed and oppositely while braking.

The yaw axis : A motion around z axis initiates a so-called yaw angle ψ which does not have a significant influence on ground dynamics.

The wheelbase is the distance along the x axis between the nose wheel and the main wheels (Figure 2.4). This length has an influence on the turning radius and on the directional control in case of a differential drive configuration (i.e. a free nose wheel and two sets of driving wheels on the main gear providing the motion torque and the directional control).

The track is the distance along the y axis between the left and the right main landing gear[1]. It has an influence on the roll behavior in turns.

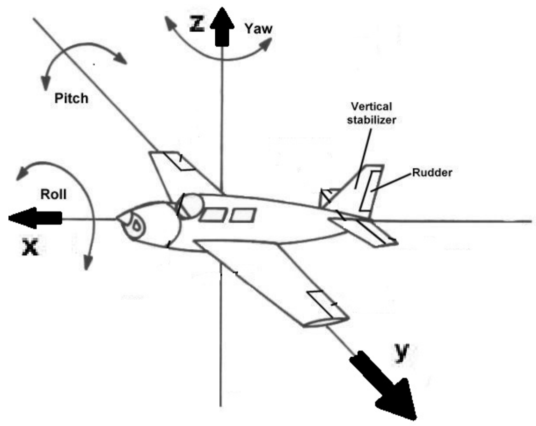

Figure 2.3: The aircraft axis and angles [2]

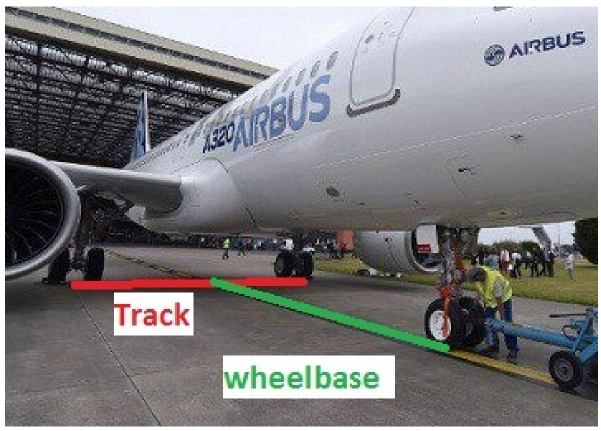

Figure 2.4: The wheelbase and the track [2]

The caster angle is the angle between the steering axis and the vertical axis of the steered nose wheel, i.e. between the pivot line and the vertical axis passing through the ground-wheel contact point. By convention in Vehicle Dynamics, this angle is positive when the extension of the steering axis crosses the ground in front of the ground-wheel contact point (Figure 2.5) [12].

[1]The word *landing gear* or *gear* is referring to the whole mechanism sustaining the aircraft wheels. It can be confusing with the engineering meaning of a *gear*, composed of two toothed wheels, e.g. used in a (speed) reducer.

A positive caster angle provides an auto-stabilizing effect (e.g. the front wheel of a bicycle). Indeed, if the wheel is not aligned with the direction of the aircraft motion, a lateral force appears on the wheel at the contact patch (Figure 2.6). This force acts behind the pivot axis leading to a self-aligning torque. However, this auto-stabilizing effect increases the force needed to turn the wheel out of the aligned position so that more force is needed to turn.

In case of a neutral or zero caster angle, a self-aligning torque still exists when the wheel is rolling because the resulting lateral force is also acting slightly behind the centre of the contact patch due to the elastic deformation of the rubber tire as illustrated in figure 2.7.

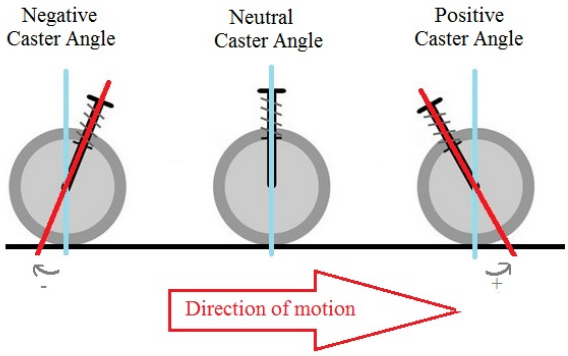

Figure 2.5: The caster angle, positive, neutral or negative[11]

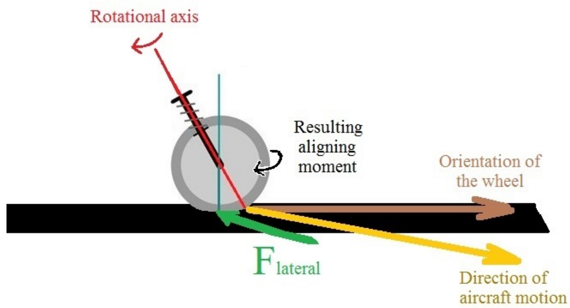

Figure 2.6: The auto-stabilising effect of a positive caster angle

2.2.2 Road-tire contact patch

The shape of the contact patch depends on the tire type (Radial or Bias) as illustrated in figure 2.8. Compared to the bias design, the radial tire has a wider footprint but has a shorter length. This is due to its flexible thinner sidewalls, offering a better grip. The flexibility of the sidewalls offers a better comfort at high speed by filtering the high frequencies developed by the pavement irregularities. On the other hand, the bias tire supports higher loads but its smaller contact patch reduces the grip and is less adaptable for higher power transmissions needed for a high speed braking phase at landing or during a rejected take-off. For those reasons mainly, most of today's aircraft and cars are equipped with radial tires.

When the wheel is aligned with the direction of travel of the vehicle, the contact patch of a rolling tire is not fully sticking to the road. An area with a mix of adherence and slip is present, i.e. a mix of pure rolling, where $F_{long} < \mu F_n$ [2], and pure slip, where $F_{long} = \mu F_n$. This longitudinal force is increasing from the front to the back along the contact patch. Once the force reaches $F_{long} = \mu F_n$, the tire element at that point on the contact patch starts to slip. The slip area starts from that point up to the back.

When the wheel is not aligned with the direction of travel of the vehicle, the rubber of the tire within the contact patch can be associated to an elastic material experiencing shear stresses inducing lateral forces. When the shear stress reaches $\tau = \mu\sigma$ [3], the tire starts slipping and the tire progressively takes back its initial shape (indicated by the green area in figure 2.7). In a standard configuration, the front of the contact patch is in full adhesion (Brown area in figure 2.7), the shear stress is starting from zero at the leading point and increases gradually until it

[2] Coulomb law: $F_{long} = F_t$ is the transverse force, μ the coefficient of friction and F_n the normal force [43]
[3] This behavior is the local expression of the Coulomb law $F_t = Flat = \mu F_n$.

reaches its limit (peak point, indicated by the red line in Figure 2.7).

Due to the shear stress shape, when the tire is not aligned with the wheel centre velocity, i.e. the direction of the vehicle motion, the resulting lateral force is acting at a point backward of the contact patch leading to a self-aligning torque (Figure 2.7). The position of F_{lat} induces an aligning torque, the so-called self-aligning torque of the tire M_{yaw}, regardless of the caster angle value.

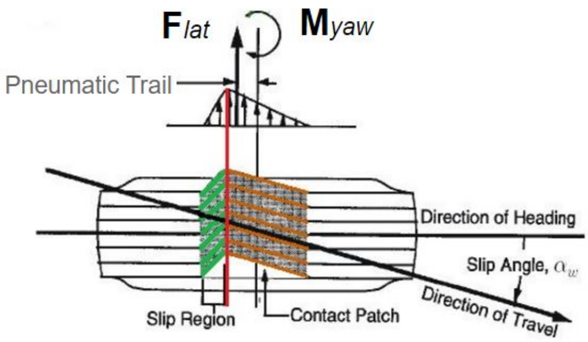

Figure 2.7: The self-aligning torque [12]

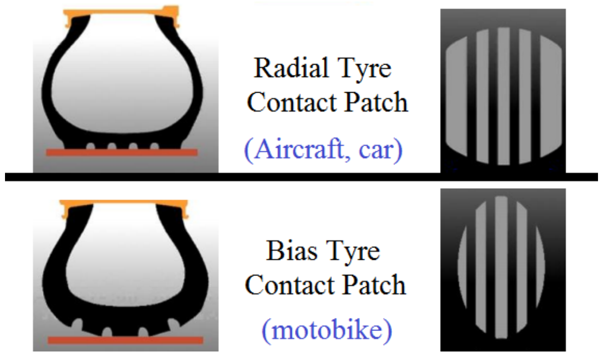

Figure 2.8: Difference tire type contact patch. Aircraft are equipped with Radial tire [13]

2.3 Tire model

The tire is the most important part to be considered in a ground vehicle dynamics analysis or simulation. Indeed the longitudinal and lateral motion of the vehicle are influenced by the tire contact forces and torques. Let us describe the 3 forces and the 3 torques applying on the tire:

- F_x, the longitudinal force
- F_y, the lateral force
- F_z, the vertical or radial force
- M_x, the tilting torque
- M_y, the rolling resistance torque
- M_z, the self-aligning torque

The way to determine those forces and torques can be achieved via an accurate dynamic friction model. Some of their components can be neglected depending on the desired objectives (e.g. M_x in most cases or even F_y on pure longitudinal analysis). In this paper, we will describe the useful tire models required for the purpose of our study.

2.3.1 Wheel/tire model characteristics

The wheel radius deflects under the aircraft weight (F_z). This deflection is referred to as δ in figure 2.9 and equals to the difference between the radius of the uncompressed wheel (R) and the instantaneous distance between the centre of the wheel and the ground (r_δ). This deflection will have an important role in the determination of the forces and torques because the tire can be reasonably modeled as a spring-damper system in the radial direction.

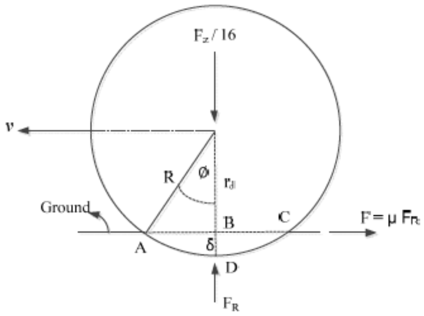

Figure 2.9: Deflection illustration [14]

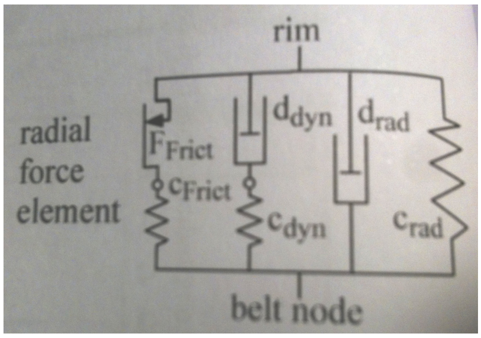

Figure 2.10: Complex tire model [15]

Radial spring-damper system

In more complex radial models (i.e. vertical axis), the tire spring-damper system can be divided into 2 subsystems [15]. One corresponds to the steady state characteristics, the second one takes the dynamic effects into account. In addition, if the rim is considered in the model, a dry friction-stiffness model (c_{Frict}) between the rim and the tire acts sporadically, as represented on the left side of figure 2.10. To simplify this complex model, with the objective to minimize the computing time, it is a best practice for simulation purposes to only use a simple spring system and to simply neglect the radial damping.

$$F_z = k_x \delta \tag{2.1}$$

Tire radial stiffness experiments

In order to find k_x, some experiments were performed on Airbus A300-600 Dunlop radial tires. The following assumptions were established :

- The aircraft is equipped with 10 identical tires with identical inflation pressures ($200[psi] = 13.79[bar]$) carrying each 1/10 of the aircraft load (W in [N]), i.e. $F_z = \dfrac{W}{10}$
- The tire inflation is neither subject to atmospheric pressure variations nor to temperature variations.
- Each data is the mean value of the deflection measured on 2 wheels from the left main landing gear (bogie of 4 wheels).
- The measurement accuracy is half a centimetre. This huge assumption is resulting from the low quality of the measurement tool that could be brought in the vicinity of the aircraft without any security restrictions.

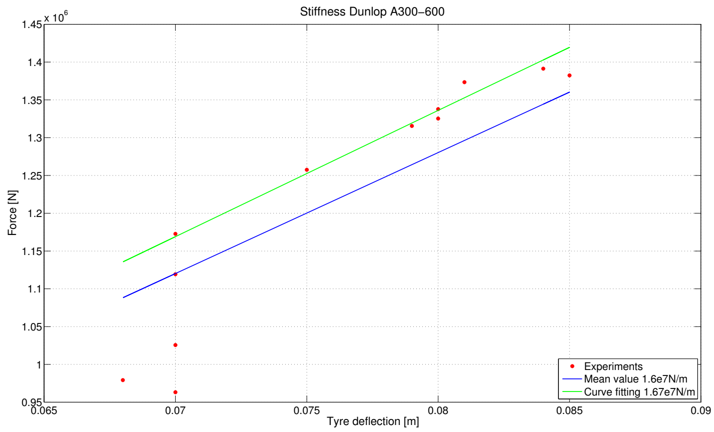

Figure 2.11: Tire stiffness coefficient : Experimental determination on A300 tires

The variations between all measurements are coming from the above-mentioned assumptions. After data analysis, the average value (blue line) is $k_z = 1.6 \cdot 10^7 [N/m]$. Compared to the value mentioned in the tire model used by USAF, where $k_z = 1.75 \cdot 10^7 [N/m]$ for an inflation pressure of $220[psi] = 15.17[bar]$ [44], measurements seem to be of the right magnitude order.

2.3.2 Theoretical tire friction models

There were many theoretical tire friction models developed over the years.

Dahl model

The Dahl model is based on the stress-strain curve of the material compatible with the Coulomb equation noted:

$$F_c = \mu \cdot F_z \tag{2.2}$$

where F_n is the normal force and μ the dynamic friction coefficient. [45]

Dahl models the stress-strain curve by a differential equation with the two following input variables : the displacement x of the local tire element of the contact patch and the sign of the velocity v of that tire element in regards with the road [16]. The equation takes into account the hysteresis phenomena (Figure 2.12). The material under stress has a friction force gradually increasing until rupture occurs, i.e when F_c is reached, where $\frac{dF_x}{dt} = 0$.

$$\frac{dF_x}{dt} = \frac{dF_x}{dx}\frac{dx}{dt} = \sigma(1 - \frac{F_x}{F_c} sign(v))^{\alpha} v \tag{2.3}$$

where F_x is the Dahl longitudinal friction force, x is the displacement, σ is a stiffness coefficient and α determines the shape of the stress-strain curve ($\alpha = 1$ is commonly used).

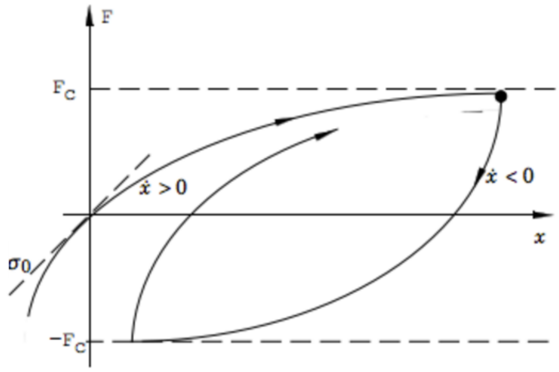

Figure 2.12: Friction force in Dahl's model [16]

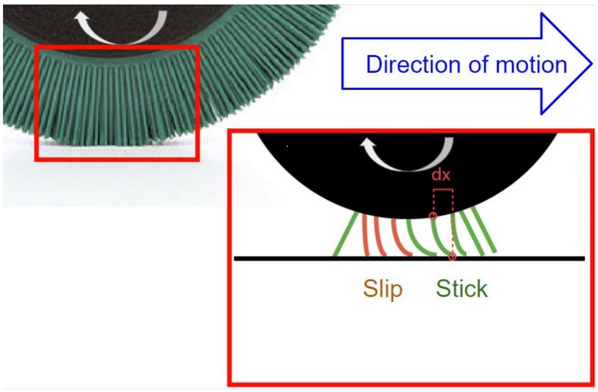

Figure 2.13: Bristles illustration

Bristle model

Following the Bristle technique, the behavior of all microscopical contact points between two irregular surfaces such as the tire and the ground are modeled by bristles. The tire surface can then be represented by a multitude of radial flexible bristles (Figure 2.13). As the tire moves, the green sticking bristles act like a spring and their strains increase, developing a friction force [16]:

$$F_x = \sum_{i=1}^{n} \sigma_0 \cdot \delta_x \tag{2.4}$$

with the number of bristles N, their stiffness σ_0, the relative deformation of the bristle δ_x. This model incorporates the random nature of friction through the N parameter. But this model is too complex and time-consuming for simulations and may end up in oscillatory results due to the absence of a damping effect on the bristles.

LuGre model

The LuGre model was inspired by the bristle one (i.e. when a tangential force is applied, the bristles deflect like springs) [46]. The LuGre evolution is that when the deflection reaches a certain value, the bristles start to slip (orange ones in figure 2.13). This permits to include the Stribeck effect, i.e. the stick and slip behavior. The average bristle deflection z is determined by the velocity during a steady-state motion.

$$\frac{dz}{dt} = v_r - \frac{\sigma_0 |v_r|}{g(v_r, v_s)} z \tag{2.5}$$

$$F_x = \sigma_0 z + \sigma_1 \frac{dz}{dt} + f(v) \tag{2.6}$$

where $g(v)$ is the Stribeck effect function, $f(v)$ is the viscous friction function usually linearized as $f(v_r) = \sigma_2 v_r$ and σ_2 is called the viscous friction coefficient [47]. Both functions are illustrated in figure 2.14. The relative velocity v_r is the relative speed between the point of contact (on the tire surface) and the velocity of the wheel centre $v_r = v - r_d \omega$. The Stribeck velocity v_s is a boundary value of v_r at which the tire (i.e. the bristles) starts to slip on the surface. A reasonable approximation of the Stribeck effect is function of the static and Coulomb friction coefficients respectively μ_S and μ_C. [17]

$$g(v_r, v_s) = \mu_C + (\mu_S - \mu_C) e^{-|\frac{v_r}{v_s}|^{0.5}} \tag{2.7}$$

The LuGre dynamic friction model is preferred to the dynamic Dahl one (Dahl, 1968) for aircraft tires because it takes into consideration this Stribeck effect.

The longitudinal slip between the geometrical point of contact and the surface is defined as :

$$\gamma = \frac{v_r}{v_{aircraft}} \tag{2.8}$$

An example of the LuGre friction coefficient ($\frac{F_x}{F_n}$) related to the slip ratio for the LuGre model is illustrated in figure 6.9. Around the origin, it clearly defines a linear behavior terminated by a peak value, which can be associated with the Stribeck velocity.

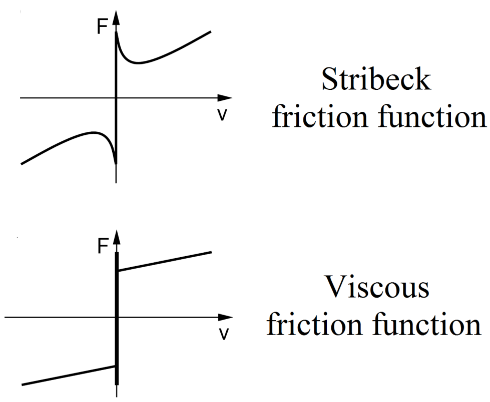

Figure 2.14: The Stribeck friction function and the Viscous friction function illustration [17]

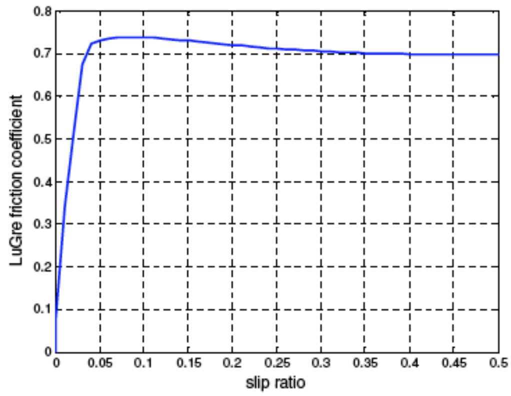

Figure 2.15: LuGre friction coefficient in regards with slip ratio [14]

2.3.3 Experimental tire friction model

The LuGre tire model is a reasonable choice for aircraft tire modeling under landing constraints (i.e. shocks) because it is applying the Stribeck effect without being too complex for simulation. Indeed, it only requires the input of 6 parameters (σ_0,σ_1,σ_2,μ_C,μ_S,v_s). However, this model only depicts the distribution of longitudinal and normal forces and will not suffice for our taxi operation simulations. In this case, we need to turn to another more complex model that integrates lateral forces and the (self-)aligning torque as well.

Pacejka-Bakker model

Up to now, all these models were based on physical laws and properties. The next step consists in developing models based on empirical methods. From experimental data, Bakker used the Pacejka magic formula to build its tire model by *curve-fitting* his results. Here is the famous so-called "magic formula" of Pacejka [48]:

$$F(\gamma) = D \cdot sin\,(C \cdot atan[B(1-E)\gamma + E \cdot atan(B\gamma)]) \tag{2.9}$$

where B (stiffness), C(shape), D(peak) and E(curvature) are fitting constants. F is the normalized force, e.g. lateral F_{lat} or longitudinal F_{long} divided by the normal force F_z, and is function of the slip (γ).

The Bakker coefficients used in this study are the ones corresponding to a car tire. Therefore, the model has to be adequately adapted.

First, we compared the mass supported by each wheel on a conventional car with the one on an Airbus A320. By approximating the mass of a car equipped of 4 wheels to 1[t] and the Airbus A320 one to roughly 70[t] mainly distributed among the 4 main landing gear wheels, we finally get a difference factor of 70. From there, at each time step, the algorithm is taking this corrective factor into account via 3 steps:

1. The normal force calculated on each wheel ($F_n = m \cdot g$) is virtually divided by 70.
2. With that reduced normal force and the calculated slip γ, the Bakker model computes the lateral and longitudinal forces acting on the wheel.
3. Those lateral and longitudinal forces (corresponding to a car wheel) are finally multiplied by 70 to be used in our aircraft model.

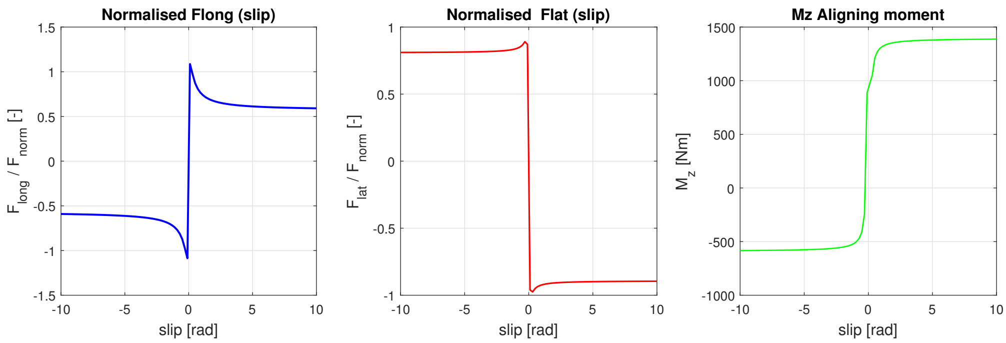

Figure 2.16: The Bakker's car coefficients applied to the aircraft weight.

The results of the normalized forces are visible in Figure 2.16. The Stribeck effect is still visible although it is an experimental approach. This means that the LuGre model approximates the reality quite well for longitudinal forces.

2.4 ICR steering geometry

In a constant radius turn R_n at constant speed $V = \omega \cdot R_n$, the objective of the vehicle is to stay on the curved track with each wheel rolling without slipping (Figure 2.17). This track is similar to a circle with a defined radius R_n around a reference point ICR (i.e. Instant center of rotation). As the main wheels are on the left and right sides of the longitudinal axis of the aircraft, they travel around the ICR on different circles of radius R_i (i=1,2,3,4). As the rotational speed ω around the ICR is the same, each wheel has to travel at a different speed $V_{wi} \neq V$ with (i=1,2,3,4) to avoid excessive longitudinal wheel slip.

$$\Omega_w = \frac{V_i}{R_i} \tag{2.10}$$

As seen in figure 2.17, each wheel has to be perpendicular to the vector joining ICR and the center axle of the wheel to avoid wheel side slip.

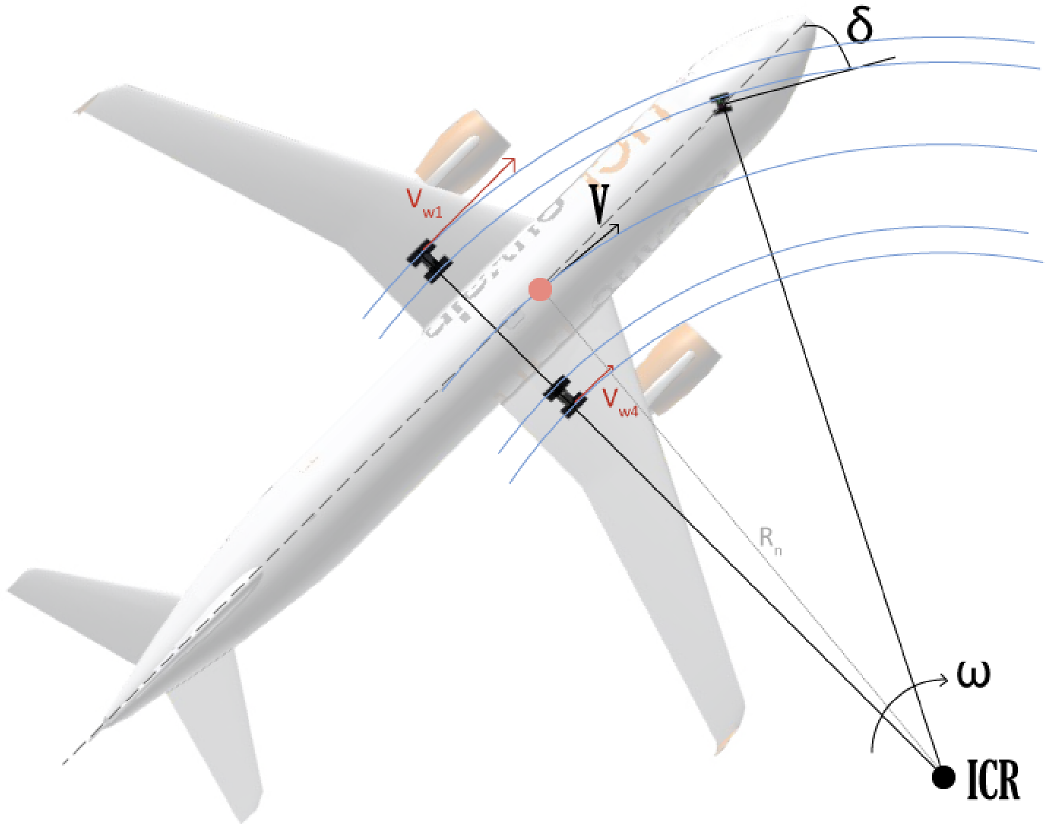

Figure 2.17: ICR

Chapter 3 : Modeling method of the Airbus A320

In this chapter, we explore how to model an aircraft using a specialized software such as Robotran.

3.1 Fundamentals of Robotran

Robotran [49] is a symbolic generator of multibody models. An aircraft, like any multibody system, can be - for the sake of modeling - seen as in a set of distinct bodies linked by degrees of freedom called *joints* in Robotran. Some of these degrees of freedom can be controlled in specific situations via actuators (e.g. the rotation of the nose wheel steering).

3.1.1 Inertial frame

Robotran uses a Cartesian inertial frame whose its orientation can be chosen by the user. In this case, it was decided to respect the conventional aviation frame defining x as the longitudinal axis of the aircraft positive in the forward direction and z as the vertical one positive in the upward direction. Consequently, y points to the left (Figure 2.3).

3.1.2 Bodies and inertia

Hypotheses All bodies are considered as rigid. In other words, this means that the characteristics of elasticity and plasticity of aircraft materials are not taken into account.

Each of those body has a mass, a center of mass (x,y,z location) and an inertia matrix (3x3). This last element defines the masses distribution around the center of gravity. It is essential data to model how the aircraft will behave under movement.

In this study, the inertia matrix is calculated based on simple geometric figures such as cylinders (C) and rectangular parallelepipeds (R). Indeed, a body can be composed of multiple *sub-bodies*, themselves represented by cylinders and parallelepiped (e.g. the aircraft main body is composed of the fuselage, the wings, the engines and the tail).

The inertia matrix of body assembly, like the main landing gear, is computed via the Steiner theorem [50].

$$I_{assembly} = \sum_{n=1}^{i} I_{subbody,i} + m_{subbody,i} \cdot D^2_{subbody,i} \tag{3.1}$$

where m is the mass of the *sub-body (i)* and D is the matrix referring to the distance between the center of gravity position vector of the *sub-body (i)* ($\overrightarrow{CG_i}$) and the one of the *body assembly* ($\overrightarrow{CG_a}$). The matrix D has the form :

$$D_{subbody,i} = \begin{bmatrix} 0 & -d_z & d_y \\ d_z & 0 & -d_x \\ -d_y & d_x & 0 \end{bmatrix} \qquad \begin{bmatrix} d_x \\ d_y \\ d_z \end{bmatrix} = \overrightarrow{CG_i} - \overrightarrow{CG_a}$$

3.1.3 Joints

A 6 degrees of freedom joint is obtained via the succession of 3 translational (x,y,z) and 3 rotational (x,y,z) degrees of freedom (dof). By constraining certain degrees of freedom, it is possible to obtain any kind of joint. In Robotran only the two following joints are available and need to be combined in a sequential manner to obtain the desired degrees of freedom of any real joint.

- revolute joint (1 dof in rotation)
- prismatic joint (1 dof in translation)

In Robotran, three roles can be given by the user to joints : joints can be *independent*, *dependent* or *driven*. For the two first categories, their existence is linked to the presence of constraints (e.g. loops described in 3.1.4). The *driven* joint permits to assign a certain value in position, speed and acceleration to it (e.g. the blocked position of an extend gear of an aircraft, or an imposed motion of a body).

3.1.4 Tree-like versus closed-loop structures

To describe the so-called *topology of the system* [18], i.e. the way bodies are connected, a tree-like structure is always used as represented in the green box in Figure 3.1. A tree-like structure means that the set of bodies and joints cannot create any closed-loop (red box in Figure 3.1). Unfortunately, many multibody mechanisms are forming some (e.g. the landing gear mechanism). To take those loops of bodies into account, we have to assure that each body only has one parent body but the number of child bodies is not restricted. This means that a particular procedure has to be used to virtually transform those close-loop structure into a tree-like one. In Robotran, three different ways to cut a loop exist to obtain the tree-like structure:

- Cut in a body;
- Cut in a ball joint;
- Cut in a connecting rod;

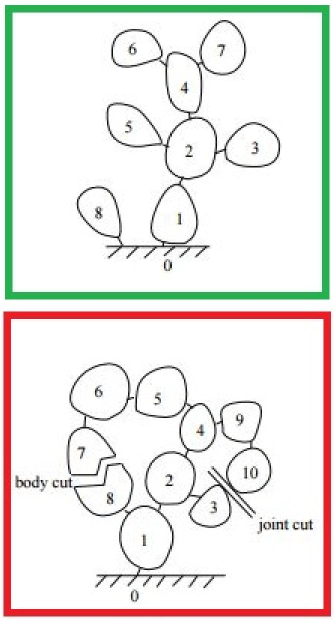

Figure 3.1: The multibody can have a tree-like (green) or a closed-loop structure to which cuts are applied (red) [18]

If closed-loop mechanism are described in Robotran, e.g. the landing gear visible at Figure 3.2, the *independent* and *dependent* joints take on their full meaning. Indeed, we can imagine to set the prismatic joint of the nose wheel suspension as *independent* and the revolute joint connecting the two rods as *dependent*. Once the suspension is travelling up or downwards, a *dependent* motion of the revolute joint will be induced.

Figure 3.2: The nose wheel suspension joints [19]

However in this study, to reduce the computation time, we simplified each landing gear mechanism to avoid any loops, as mentioned in the coming section 3.2.

3.1.5 Forces and torques

In Robotran, a distinction is done between external forces and torques (e.g. wind blowing on the aircraft, tire contact on the road) and internal ones (e.g. motor torque applied to the wheel).

Joint forces and torques

These forces and torques (noted Q^i for joint i) contribute to the motion equations and acts within the joint.

External forces and torques

In addition to the gravity and to the joint forces and torques, there exists external forces and torques, noted f_{ext},t_{ext}, acting on the bodies. In Robotran, in case of multiple external forces (or torques) applying on the same body, a single resultant force and pure torque is calculated, with respect to the center of mass of the body.

3.1.6 Dynamical solution

After representing the multibody system as a collection of joints and bodies submitted to possible constraints (loop, user,...), Robotran symbolically calculates the dynamical equation [49] :

$$M(q)\ddot{q} + c(q, \dot{q}, f_{ext}, t_{ext}, g) = Q(q, \dot{q}) + J(q)^T \lambda \tag{3.2}$$

These equations allow to calculate the joint accelerations $\ddot{q}$ for a given configuration (determined by joint position q and speed $\dot{q}$) while forces and torques (f_{ext}, t_{ext}, g, Q) are applied. This computation method is called *Direct Dynamics*.

In equation (3.2) :

- M is the mass matrix (symmetric, $[n * n]$).
- c is the non linear dynamical vector $[n * 1]$. All the gyroscopic, centrifugal and gravity terms, as well as the external forces (f_{ext}) and torques (t_{ext}).
- q is the vector of the generalized coordinates, referring to the *relative* motion in the joints of the system.
- Q is the vector of joint forces and torques.

- J is the constraint matrix $[m * n]$ i.e. $J = \frac{\partial h}{\partial q^t}$
- λ represents the Lagrange multipliers associated with the constraints (dimension : $[m * 1]$).

The physical and geometrical constraints can be induced by loops (h_l) in the multibody system or can be introduced by the user for a specific reason (h_{user}). All the constraints have to be satisfied at any time, i.e.

$$h(q) = \begin{bmatrix} h_l(q) \\ h_{user}(q) \end{bmatrix} = 0 \qquad [m * 1] \tag{3.3}$$

which amounts to solve the dependent variables in terms of the independent ones.

However in our aircraft model, there are no loops and thus no dependent joints. The constraints $h(q)$ are nonexistent and so are the Jacobian J and the Lagrange multipliers λ.

The system equation (3.2) simply reduces to :

$$M(q)\ddot{q} + c(q, \dot{q}, f_{ext}, t_{ext}, g) = Q(q, \dot{q}) \tag{3.4}$$

This differential system is solved using the initial values of the generalized coordinates $q(t = 0)$ and $\dot{q}(t = 0)$. Once accelerations are obtained, velocities and positions of the next time step are calculated by time integration that iterates until the first time is considered resolved.

In terms of numerical solver, when Simulink is used as interface to Robotran (see 3.1.8), an automatic choice is made between 8 options. However, for our aircraft model, the two automatically selected solvers were: ODE45, a Runghe Kutta of order 4 crosschecked with an order 5 expansion, and ODE15, which is more adequate for stiff problems (e.g. when the aircraft is turning at low speed, the problem becomes stiff) [51]. We also kept the *time step* setting to *variable* to allow for stiff problem resolution.

3.1.7 Driven variables

A driven joint i can be assigned in position, velocity and acceleration. The symbol used for those driven generalized coordinates are c^i instead of q^i

$$c^i = f(t); \dot{c^i} = \dot{f}(t); \ddot{c^i} = \ddot{f}(t) \tag{3.5}$$

When driven variables (joints) are used in addition to independent ones, a special attention needs to be paid when solving the motion equation. Indeed, driven variables cannot be time integrated. A split of the independent and driven variables are thus made prior to the system resolution. The generalized coordinates are separated in q_u and q_c, respectively independent and driven variables [18]:

$$q = \begin{bmatrix} q_u \\ q_c \end{bmatrix} \tag{3.6}$$

Equation (3.4) is partitioned accordingly using the Lagrange multiplier technique [52] by defying $F \triangleq c - Q$, it then becomes:

$$\begin{bmatrix} M_{uu} & M_{uc} \\ M_{cu} & M_{cc} \end{bmatrix} \begin{bmatrix} \ddot{q}_u \\ \ddot{q}_c \end{bmatrix} + \begin{bmatrix} F_u \\ F_c \end{bmatrix} = \begin{bmatrix} 0 \\ \lambda^c \end{bmatrix} \tag{3.7}$$

The λ^c contains the Lagrange multipliers associated with the driven motion constraints 3.5. This λ^c represent the torque or force joint, depending on the joint characteristic (revolute or prismatic) [18].

$$\lambda^c = M_{cu}\ddot{q}_u + M_{cc}\ddot{q}_c + F_c$$

The dynamical equation to be solved instead of equation 3.4 becomes :

$$M_{uu}\ddot{q}_u + (F_u + M_{uc}\ddot{q}_c) = 0 \tag{3.8}$$

3.1.8 The Simulink interface

The symbolic models generated by Robotran can be easily interfaced with the block diagram environment MATLAB/Simulink®. Simulink is a multi physics modeling system software (Mathworks) with a graphical interface using blocks to design and implement controllers and to simulate any kind of dynamical systems.

A Robotran/Simulink modeling process can be represented by a three consecutive step.

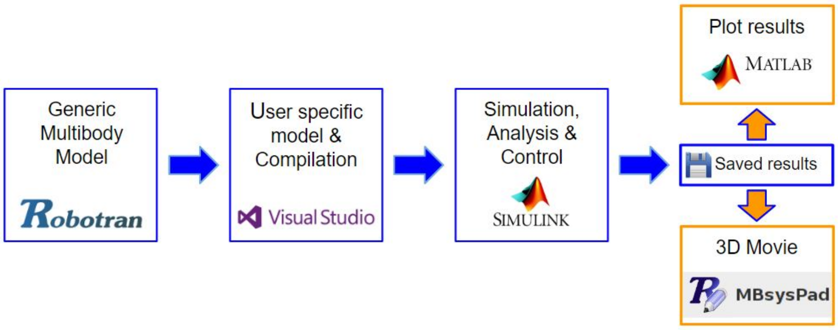

Figure 3.3: A Robotran/Simulink process

Once the multibody model is designed in the graphical editor MBsysPad (Figure 3.4), Robotran generates symbolically all the kinematic and dynamic equations under the form of C-functions with all the data and equations needed to solve the dynamics.

Secondly, certain C-functions can be filled in by the user to implement specific features such as the external and joint forces and torques (e.g. for the aircraft, the suspensions, the electrical motor torque), the driven joint time function. Then All the C-functions of the project are compiled providing a *ready to use* executable (Visual Studio).

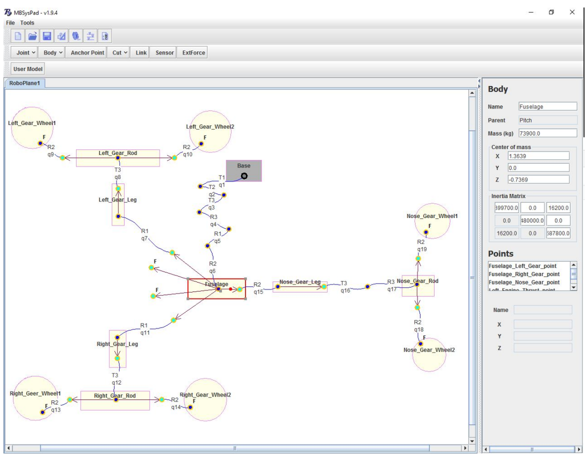

Figure 3.4: Model Building in MbsysPad

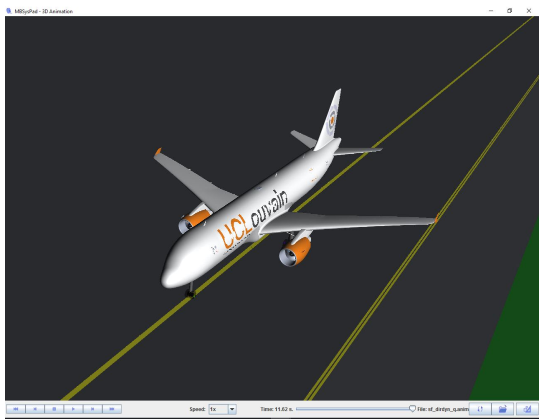

Figure 3.5: The results viewed via the animation module

Finally, the control of the system (e.g. the control of the wheel torque to adjust the speed of the aircraft), the extraction of the results and the launch of the simulation is done with Simulink, in which the model is represented as a block with inputs and outputs allowing a controlled design.

During the simulation, an animation file is created and updated to visualize the results under the form of a 3D movie (Figure 3.5).

3.2 Modeling the Airbus A320

The modeling of the Airbus A320 was carried out on the basis of the A320 Neo technical information found in the technical [53] and pilot manuals [54]. However, some information was missing or confidential and thus inaccessible. In order to cope with those missing data, some comparisons were realized with other aircraft or vehicles (e.g. the Airbus A300-600).

General hypotheses

1. The modeling is based on an aircraft at maximum take-off weight (MTOW) with all the fuel tanks full (i.e. completely filled in). Its total mass is 73 900 [kg].
2. The aircraft is divided into four major multibody sub-systems.
   - The fuselage with the wings, the engines and the tail
   - the nose landing gear (simplified design, no loops)
   - the left landing gear (simplified design, no loops)
   - the right landing gear (simplified design, no loops)

   Those design simplifications allow for a better computational efficiency by keeping a tree-like multibody structure (referring to section 3.1.6), while preserving the goals of the current work. Each landing gear is modeled by a single shaft (i.e. the leg) equipped with a suspension and connected to a rim rod. The wheels are then simply linked to this rod through a revolute joint.
3. The geometry of all parts and sub-parts is approximated by cylinders (C) or rectangular parallelepiped (R) shapes in order to calculate their inertial matrix (section 3.1.2). The simplified model is illustrated in Figure 3.7.

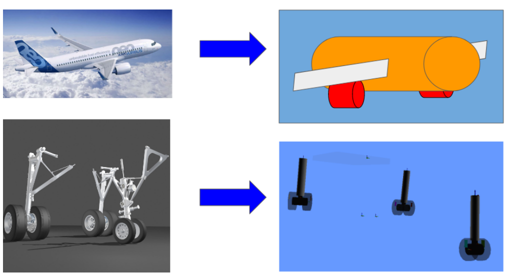

Figure 3.6: The A320 subdivided for inertial matrix calculation

Figure 3.7: The model in Robotran with a single fuselage body

4. The mass distribution was approximated through the following waterfall sequence, as all the needed information could not be found precisely [54, 5, 55]. A summary of all the resulting values can be found in Table (3.1).
   (a) The known Maximum Take-Off Weight[1] (MTOW) of the A320 Neo equals 73 900 [kg]

[1] In aviation, the term weight is used but refers to the mass in kg.

(b) The Dry Operating Weight (DOW) given as reference is 44100 [kg][2]

(c) The total fuel capacity of all the tanks is 18 728 [kg] : 12 252 [kg] stored in the wings and 6476 [kg] in the center tank placed in the fuselage at the wing root level

(d) The maximum load (i.e. passengers and cargo) is obtain by subtracting the DOW and the fuel from the MTOW : 11 072 [kg]. This mass has to be added and distributed along the fuselage

(e) The total mass of the landing gear (LDG) is around 4% of the MTOW : 2900 [kg]

(f) Each LEAP engine has a mass of 3000 [kg]

(g) So the remaining mass for the wings, fuselage and tail is :

$$DOW - LDG - 2 \cdot Engines : 35200[kg]$$

(h) Due to confidential data, an approximation has to be made for the mass distribution between wings and fuselage. A mass ratio of 1/4 for wings and of 3/4 for the fuselage was roughly estimated giving wings mass of 8800 [kg]. The fuselage and the tail have together a mass of 26400 [kg]. The load is also added to the fuselage, giving a final value of 37472 [kg].

5. The mass estimated for the landing gear (2900 [kg]) is further subdivided into three main sub-parts (Figure 3.8). The only available data was the mass of each tire [56].

(a) Because the main landing gear is designed to absorb the landing shock, we can reasonably assume that it has a heavier mass than the nose gear. Thus, we decided to estimate the nose landing gear at 772 [kg] and each main gear at 1064 [kg].

(b) Each nose wheel tire weights 23.5 [kg]. The remaining mass was split as follows : 500 [kg] for the shaft of the leg with the suspension and 225 [kg] for the rim (no brakes installed on the nose wheel).

(c) Each main wheel tire has a mass of 82 [kg]. The leg shaft was estimated at 600 [kg] and the rim (equipped with brakes) at 300 [kg].

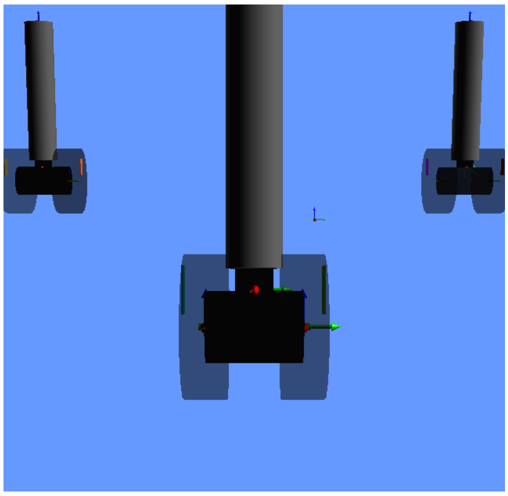

Figure 3.8: The simplified landing gears of the A320

[2]Each A320 has a different DOW and is generally regularly weighted to update its actual value. This is an important value for take off performance calculations, e.g. to determine the runway length needed for a specific loaded aircraft.

Parts	Unit	Weight [kg]	Simplified shape	Dimensions [m]
Fuselage + tail + load	1	37 472	Cylinder[3]	h= 37.57 r= 4.14
Wings with fuel	1	27 528	Parallelepiped	x=4.2 y=35.8 z=0.3
Engine	2	3 000	Cylinder	h= 3.328 r= 1.2
Main gear main shaft	2	600	Cylinder	h= 2.4 r= 0.25
Main gear rim block	2	300	Cylinder	h= 0.9271 r= 0.25
Main gear wheel	4	82	Cylinder	h= 0.4318 r= 0.5842
Nose gear main shaft	1	500	Cylinder	h= 2.4 r= 0.25
Nose gear rim block	1	225	Cylinder	h= 0.5 r= 0.25
Nose gear wheel	2	23.5	Cylinder	h= 0.2235 r= 0.381

Table 3.1: Mass distribution of the 73.9 tons

3.2.1 Bodies

The fuselage with the wings and the engines

The fuselage including the tail, the wings and both engines[4] are merged into a single body in Robotran. According to section 3.1.2, its inertia matrix $I_{aircraft}$ is obtained via the Steiner theorem, i.e. the assembling of each element inertial matrix around a common center of gravity (CG) (equation 3.1). Due to the shape simplification of each element, some hypotheses regarding the position of the center of gravity of each element were necessary (Table 3.2). Those hypotheses were made in order to obtain a final CG value within the limit of the aircraft [54]. Moreover, it was decided to target a value in the x axis corresponding to 26.5 % of MAC (Mean aerodynamic chord), i.e. a position distant from the leading edge of the wing equalling to 26.5% of the mean wing width. Due to this choice, the CG position is at a distance of 1.4[m] from the middle of the aircraft (the reference used in our model instead of the nose datum[5] for Robotran design simplification).

Simplified element	CG (x) [m]	CG (y) [m]	CG (z) [m]
Fuselage	1.7368	0	0
Wings	4.2	35.8	0.3
Engine 1	5.981	5.75	-2.13
Engine 2	5.981	-5.75	-2.13

Table 3.2: Center of gravity of each aircraft element in our simplified design

The landing gears

As mentioned in section 3.2, each landing gear mechanism is simplified to an assembly of four sub-bodies.

1. the leg shaft equipped with a suspension
2. the rim rod
3. the left wheel.
4. the right wheel

Each of those sub-bodies has its own inertial matrix, its own related CG and its own mass.

[3]Ideally, the fuselage should be seen as an hollow cylinder filled in with few complex shapes (e.g. seats) and vacuum. However, as the aircraft is supposed to be full loaded, we can reasonably approximate a filled in fuselage with full passengers, seats, luggage and cargo containers to a filled cylinder.

[4]The numbering of the engines are always done from the left hand side wing tip up to the right hand side wing, i.e. from captain to copilot side.

[5]On commercial aircraft, all positions are based on a aircraft reference point called the datum.

3.2.2 Joints

Hypothesis All the joints are considered as perfect joints without any internal parasitic forces or torques. They are two types of joints used, translational (T) and rotational (R) ones.

The fuselage with the wings and the engines

The aircraft has 6 degrees of freedom (dof) represented by 3 translational joints and 3 rotational joints. They are connecting the inertial cartesian frame (fixed to the ground) and the aircraft body (fuselage) through the following sequence (Figure 3.9).

1. Forward (T1 in the x-axis)
2. Side-way (T2 in the y-axis)
3. Upwards (T3 in the z-axis)
4. Yaw (R3 around the z-axis)
5. Roll (R1 around the x-axis)
6. Pitch (R2 around the y-axis)

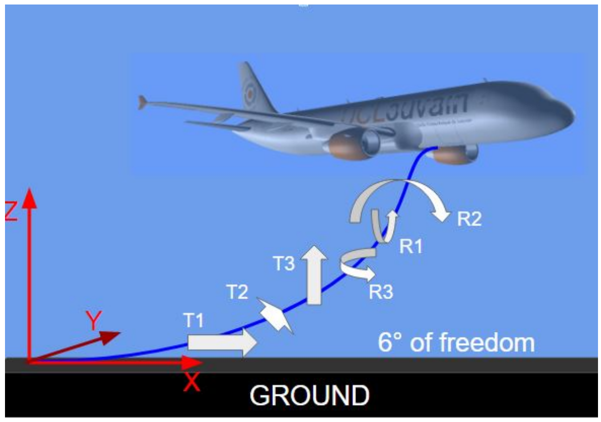

Figure 3.9: 6 dof illustration

The landing gear

The design of the main gears and the nose gear are similar, only the values of the elements are adapted. However the connection to the aircraft body (fuselage) respects the orientation of the landing gear retraction (and extension). Indeed between the fuselage and the main gear legs, a gear retraction joint is installed around the x-axis (R1) because the main landing gear retracts into the fuselage for the flight phase. In opposition, the nose gear retraction is longitudinal, inducing a rotation around the y-axis (R2) to be stored in the nose of the fuselage with the wheels in front of the gear leg.

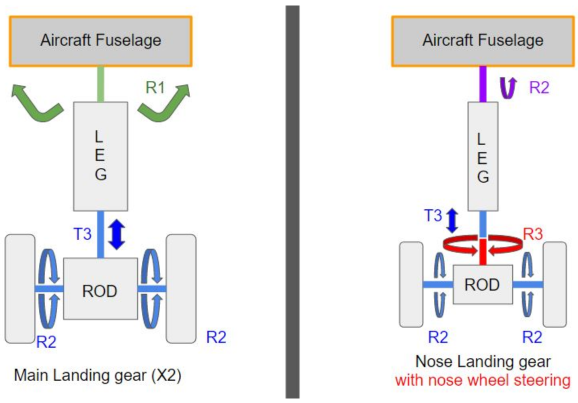

Figure 3.10: MBSysPad landing gear design

The suspensions connecting the legs with the rim blocks are modeled via a translational joint in the z-axis (T3) for all landing gears (Figure 3.10). Each wheel is connected to its rim block through a rotational joint in the y direction (R2).

Regarding the control wheel steering, a rotational joint was added between the suspension and the rim block of the nose wheel in order to allow the wheel to be turned around the z-axis (R3).

3.2.3 Forces and torques

Joint forces and torques

Suspension : The suspension forces have to be implemented for each landing gear. They are inserted as joint forces and torques in the symbolic C-functions generated by Robotran. The suspension force equation is based on a spring and a damper element as described by :

$$F_{suspension} = K_{spring} \cdot (q - l_0) + D_{damper} \cdot \dot{q} \tag{3.9}$$

with K_{spring} the stiffness of the spring, l_0 the initial length of the spring, q the actual length of the joint, D_{damper} the damping coefficient and $\dot{q}$ the actual velocity of the joint. The K_{spring} and D_{damper} coefficients, being confidential data, had to be respectively estimated through equilibrium (i.e. static analysis) and constant speed turn scenario (i.e. quasi-static analysis) simulations. The objective was to obtain realistic values of the suspension margin length at its maximal compression, i.e. the visible part of the piston which is about 10 [cm] (Measured on the A300-600). The final values obtained are the ones visible in Table 3.3.

Landing gear	K_{spring} [kN/m]	l_0 [m]	D_{damper} [kN s/m]
Main	800	0.469	90
Nose	500	0.43	80

Table 3.3: Suspension coefficients for each landing gear based on model simulations

Electrical motor output : In the case of an electrical motor on the main wheels, the torques extracted from the gear reducer is added as a joint torque via the Simulink interface.

External forces and torques

Engine thrust : While the aircraft has its engines running, even being in idle, a certain amount of thrust is delivered. It has been inserted as external forces via the Simulink interface. The application point of these forces were defined via a sensor point in MBsysPad that allows to precisely locate a resultant force.

Chapter 4 : Specifications

Following the modeling of the current Airbus A320 design, we will define the specifications of an autonomous taxi and pushback system to enhance the A320. In respect with those specifications, we will then define viable aircraft configurations.

4.1 Specifications

The objective is to identify the most appropriate technology assembly for an autonomous taxi system for the Airbus A320, i.e. the best mix of mechanical, automation and electrical designs, to allow the automated aircraft to respect current ground operations constraints and aviation standards. Those essential functions and constraints are identified in the specifications brief here under. They are separated into two categories[1]: the main functions (Table 4.1) and constraint functions (Table 4.2).

Index	**Main functions**
MF1	Move autonomously on the ground.
MF2	Follow a specific trajectory in an autonomous way.
MF3	Regulate the taxi speed.
MF4	Estimate travel time
Sub index	**Criteria and levels of main functions**
1.1	Based on the Airbus A320 characteristics and design.
1.2	User can monitor the system at any moment in time.
2.1	Trajectory is defined by geographical coordinates (e.g. N50 54.2 E 004 29.0).
2.2	Trajectory is most of the time marked on the ground by yellow painted lines (width 0.30[m]) with black painted edges.
2.3	Trajectory is sometimes indicated by taxiway lights spaced by 15 [m].
2.4	Maximal deviation from track : 1 [m] on straight line, 2 [m] on curved line.
2.5	In low visibility conditions with 3 [m] visual range.
2.6	On snow covered taxiways : up to 0.1 [m] snow.
3.1	Accuracy of 5% required.
4.1	Estimate precisely time of travel to a specific point along a track.
4.2	Communicate automatically travel time to ATC.

Table 4.1: Functional specifications of the autonomous system : main functions

[1]Those two categories are usually assembled in one document. For document layout it was decided to separate them into two tables.

Index	**Constraint functions**
CF 1	User can activate and deactivate the system.
CF 2	System working on every airport.
CF 3	Keep A320 current fuselage structure.
CF 4	Integrate system into the aircraft.
CF 5	Able to stop whenever it is required.
CF 6	Respect current used taxi speeds.
CF 7	Adapt speed to reach target time at a specific target position.
CF 8	Assure comfort of passenger.
CF 9	Minimize fuel consumption.
CF 10	Minimize additional maintenance cost.
CF 11	Track design is a continuous function.
Sub index	**Criteria and levels of constraint functions**
1.1	Reaction time : 1[s].
1.2	Deactivation by a push button.
1.3	Deactivation by manual brake application.
2.2	Airport respecting ICAO airport rules [57].
4.1	Use aircraft power only.
4.2	No external device connected to the aircraft.
5.1	When the last point of trajectory is reached.
5.2	When a red stop bar is detected (see Figure 1.4).
5.3	When obstacle in front of the aircraft, engines or wings : stop before obstacle.
5.4	When obstacle is behind the tail (backward motion) : stop before obstacle.
6.1	Max speed on straight track : 30[kts].
6.2	Max speed on curved track : 15[kts].
6.3	Min speed capability : 20[kts].
7.1	Target position and time introduced by the user.
8.1	Respect general transport comfort criteria.
11.1	The 1^{st} and the 2^{nd} derivative of the track function is continuous.

Table 4.2: Functional specifications of the autonomous system : constraint functions

4.2 Potential aircraft configurations

In respect with those specifications, we identify three possible configurations :

1. An A320 with a directional nose wheel and with 4 electrical motors powering each main gear wheel.
2. An A320 also with a directional nose wheel but with the thrust being provided by the turbojet engines of the aircraft.
3. An A320 equipped with a free nose wheel and with 4 electrical motors powering each main gear wheel. This configuration is the so-called *differential drive* configuration.

In the following chapters, we will carefully analyze the mechanical aspects linked to those configurations, implement automation and define the controlled powering electrical equipment required. Finally, by combining all those elements, we will be able to compare them, identify potential improvements and determine the operational impact on actual aviation ground operations.

Chapter 5 : Mechanical aspects

Since three potential aircraft configurations were highlighted, let us analyze the mechanical aspects and the required modifications for each of them.

5.1 The A320 with the directional nose wheel and with 4 electrical motors powering each main gear wheel

In this configuration, the current A320 nose wheel steering design is reused (section 1.3). There are no mechanical modifications, the only work be to done is to insert a trajectory controller upstream of this electronic box, i.e. to replace the inputs coming from the pilots.

The 4 main wheels have to be adapted to allow the placement of an electrical motor. The type of motor used will be discussed in chapter 7. Nevertheless, an adaptation of the rim rod mass has to be done on our A320 model. The mass of the electrical motor used in a previous similar project was about 150[kg] per wheel [58].

Indeed, this power supply configuration was already tested by EGTS (Electric Green Taxi System), a joint venture between Safran and Honeywell created in 2011 [59]. The goal of this project was to reduce the fuel consumption during taxi and pushback operations. However, the system was not autonomous, pilots having a joystick to control the nose wheel position and speed. Unfortunately, due to the drop in oil prices over the last years, the project did not encounter the expected success and was aborted before the commercialization phase (initially planned to be in 2018 [60]).

Figure 5.1: EGTS : Main wheel electrical motors [20]

5.2 The Airbus A320 with the directional nose wheel and with the thrust being provided by the turbojet engines of the aircraft

This configuration is the replica of what is manually done by pilots nowadays. No mechanical adjustments are needed. However, an important challenge involves the braking control. Indeed, the turbojet engines while running at idle power, i.e. the lowest regime possible, are still providing a certain thrust. Nowadays, pilots are braking to reduce their taxi speed even with engines in the idle position. Consequently, on the autonomous aircraft taxi system, the speed has to be controlled by both the thrust and the brakes.

5.3 The Airbus A320 equipped with a free nose wheel and with 4 electrical motors powering each main gear wheel.

The so-called differential drive configuration is the common one used in robotics, e.g. cleaner robot, grass-cutter robot, due to its sharp turn ability and simple control implementation. However most of those robots are equipped with a castor wheel at the rear (Figure 5.2). To respect the specifications of chapter 4, a move of the nose wheel to the rear of the aircraft without affecting the fuselage design cannot be done. We will thus have to study the feasibility of a front free nose wheel.

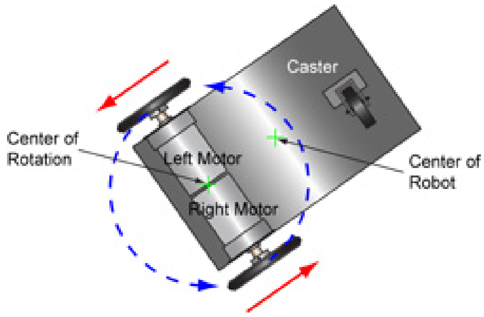

Figure 5.2: Differential drive illustration [21]

In the standard A320 geometry, the nose wheel has a positive caster angle of $0.157rad$, that we can assimilate by intuition to a positive self-aligning effect. However, this advantage theoretically induces a greater force for turns involving more torque to be delivered by the electrical motors installed on the main gear wheels. A confirmation of this theoretical intuition by some simulations is necessary. In the meantime, a comparison between different landing gear designs can be performed.

5.3.1 Mechanical analysis of the free nose wheel

In respect to the specifications of chapter 4, we decided to compare the two following landing gear designs.

1. The current A320 landing gear design with its positive nose landing gear caster angle.
2. A modified nose landing gear with a neutral or *close to zero* caster angle, i.e. a perpendicular nose wheel leg.

Because most robots are using castor wheels, it may be interesting to see the impact of this kind of wheel on the two landing gear designs mentioned above. For this study, the determined *wheel-ground* contact point is situated behind the nose gear leg at a distance equivalent to half the nose wheel radius (i.e. 38.1 [cm]) (Figure 5.3).

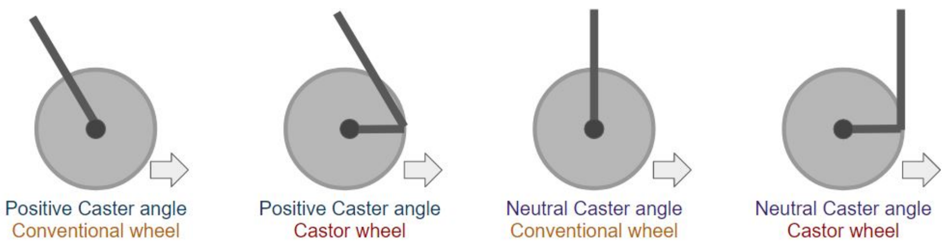

Figure 5.3: The different designs [21]

In all those mechanical designs, the orientation of the aircraft is controlled by the driving wheels based on the turn radius the aircraft plans to follow. This technique is using the ICR 2.4 to adjust the speed of each driving wheel.

First analysis : Stability of the nose wheel steering in straight line

The first comparison criteria is the stability of each configuration while applying a torque perturbation of 1.5 [kN] on both right main wheels between 2 and 2.4 [s]. No aerodynamic drag, wind or any external factor are implemented. The speed of the aircraft is set at 6[m/s].

Positive caster angle : As we see in Figure 5.4, the A320 with its positive caster angle and conventional wheel is stable, as expected, due to both the self-aligning moment of the caster angle and the one of the tire included in our Bakker model. To confirm the influence of the caster angle with the same landing gear design, we compare the conventional wheel with the castor one. The result shows a greater initial amplitude however the damping of the oscillation is quicker (5.4). To really understand the influence of the caster angle, let us continue by analyzing the neutral one with the conventional and the castor wheel.

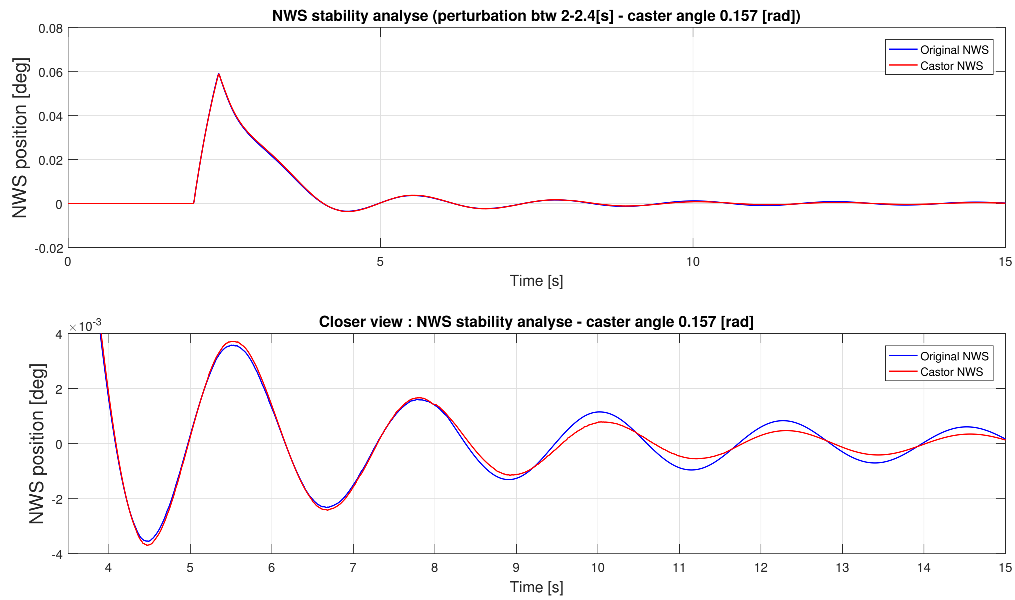

Figure 5.4: Stability analysis for the positive caster angle

Neutral caster angle : Once the caster angle is reduced to zero, the conventional wheel design becomes unstable (Figure 5.5). Moreover, the wheel initially starts to turn in the wrong direction before spinning in the right one. This behavior looks similar to the one observed on shopping caddies front wheels when the normal force acting on them is too small. Similarly, on the Airbus A320, the center of gravity is close to the middle of the aircraft, inducing that the normal force on the nose wheels is significantly lower than the one on the main wheels.

To confirm the influence of the normal force, a progressive forward center of gravity shift was realized[1]. With a 1m and 2m shift, the nose wheel is still turning in the wrong direction but it stabilizes itself to an non neutral position. With a further forward load shift, the wheel finally turns in the right direction, nevertheless it quickly becomes unstable.

When a neutral caster angle is kept but the nose wheels are replaced by castor ones, the same outcome is observable.

[1] The nose wheel suspension was consequently adapted

From those results, a too small normal force on the nose wheels can explain the unstable attitude. However, it seems that another unknown element of the Airbus design or a model simplification induces instability too.

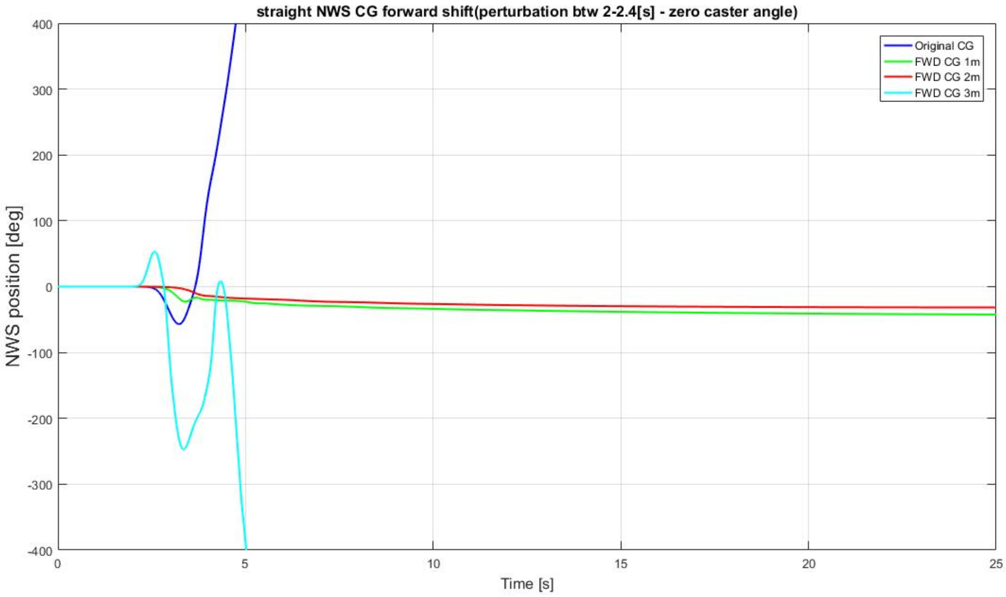

Figure 5.5: Stability analysis : neutral caster angle

Close to zero caster angle : To further understand the roles of the center of gravity position and the caster angle, a positive angle of 0.01 [rad] with different center of gravity (CG) shifts were applied. The results (visible in Figure 5.6) show that this caster angle associated with the initial CG position results in instability. As soon as the CG is shifted forward, the system gains in stability. To keep a stable system, if the CG envelope is moved rearward, the caster angle has to be increased. Nonetheless, when reaching a certain level of CG shift, the gain in stability becomes less significant (e.g. between 2m and 3m shift).

However, it is important to keep in mind that the CG envelope is determined by the aerodynamic properties of the aircraft in flight. The only way we could increase the normal force on the nose gear without affecting flying performances is to move the complete nose gear to the back and this is not allowed by the specifications (chapter 4).

The castor wheel does not bring any advantage at a small caster angle (Figure 5.7) compared to the difference seen with the normal positive caster angle of 0.157 [rad] in Figure 5.4.

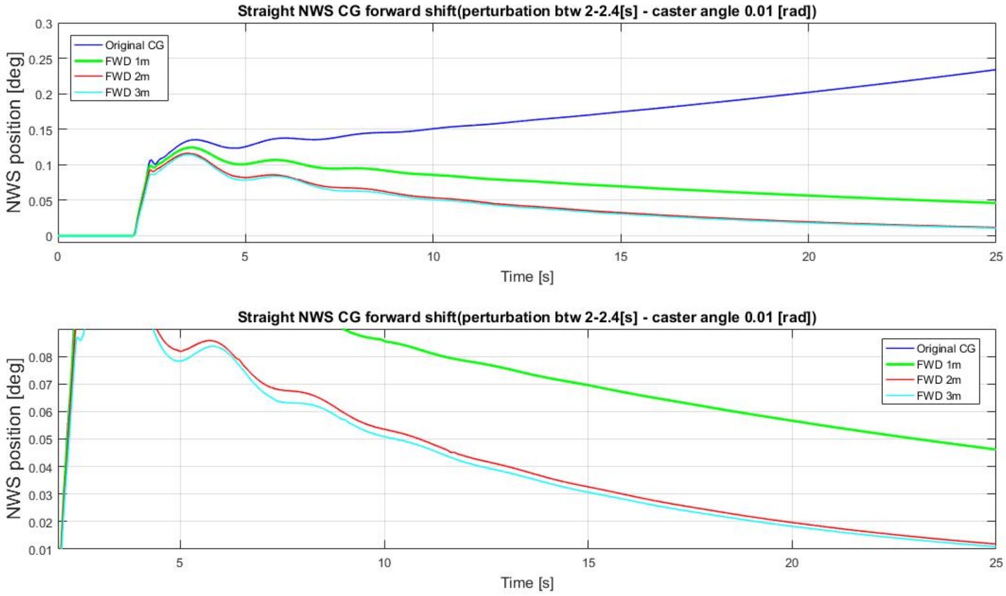

Figure 5.6: Stability analysis : *close to zero* caster angle (0.01 [rad]

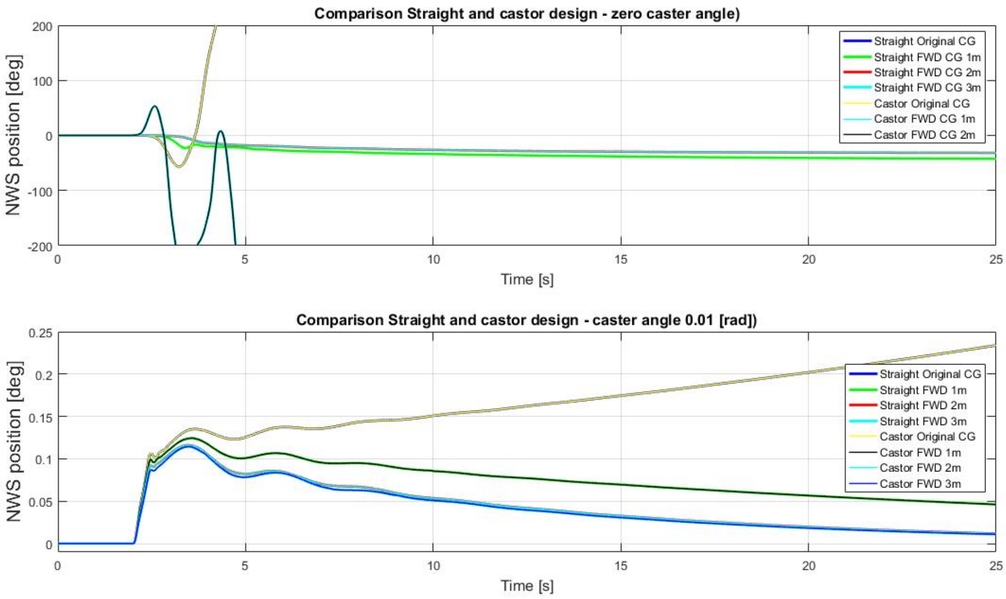

Figure 5.7: Same results observed between *Straight* and *Castor* wheel design with a caster angle of 0.01 [rad]

Observations : Those results highlight the importance of the positive caster angle on the A320 nose landing gear, which is not to be found on larger aircraft such as the A330 or the A380 having a neutral or even a negative one. This could be explained by the design and the center of gravity envelope position on the A320. However, it could also be influenced by the many assumptions done for the implementation of this model.

Second analysis : Ability to follow a specific turn radius

The second comparison consists in testing the ability of obtaining the right orientation of the nose wheel when differential torques are applied on the main wheels. The speed of the aircraft is set at 6[m/s]. The torque application is commanded in a way to respect the ICR criteria on a radius turn of 8[m] (R_N in Figure 2.17). It is important to realize that this radius turn is the one followed by the aircraft CG. The nose wheels are travelling along a 15[m] curve. The nose wheel steering should then reach a 60° (1[rad]) position.

However, the results obtained are under expectations. None of the different designs could achieve the target position (Figure 5.8). The positive caster angle landing gear is the worst responding one. The castor wheel has a lower achieved position than the conventional one. This could be expected due to the higher stability of the designs observed previously (Figure 5.4) and explained by the influence of the self-aligning torque of the positive caster angle.

Although the *close to zero* caster angle landing gear design was unstable with the normal CG position, it seems strangely stable enough in this scenario. The instability observed previously is probably not strong enough to have the time to establish itself and be visible here. Nevertheless, the achieved nose wheel steering position is the best one. Indeed, with a small forward CG shift (1m), the reached position is slightly lower, as expected due to the increased stability effect.

All the maximum values of the main wheel torques and the NWS joint rotation are indicated in Table 5.1.

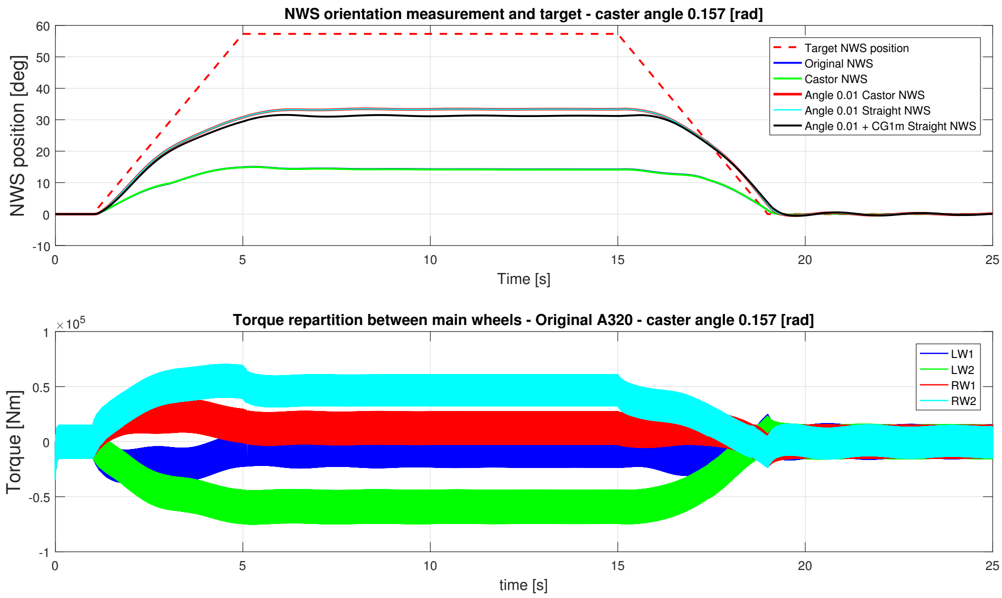

Figure 5.8: The nose wheel steering orientation on a turn track of 15[m] radius for the various NWS design (top). The torque applied on the main wheels of the original aircraft design, to respect the CIR criteria (below).

Design	Max torque on wheels [Nm]	Max NWS rotation [deg]
Original design	7e4	15.05
Castor (caster angle 0.157)	5.87e4	14.98
Straight (caster angle 0.01)	4.53e4	33.48
Castor (caster angle 0.01)	4.53e4	33.48
Straight CG shift 1m (caster 0.01)	3.98e4	31.54
Straight CG shift 3m (caster 0.01)	5.02e4	30.00
Target value	-	57.3

Table 5.1: Maximum torque and nose wheel orientation during on a targeted turn of 15m radius at a speed of 6m/s.

Conclusion

Based on these two upward analyses, we can conclude that the differential drive configuration is not a viable solution for the Airbus A320. The CG position and the caster angle are significant parameters in the nose wheel steering position stability, however they also prevent an easy orientation control. Besides those elements, the wheelbase[2] could be a factor in this unsuccessful design.

In the following chapters concerning the automation and the electrical powering equipment, the free nose wheel design will thus not be considered anymore.

[2] Distance between the main wheels and the nose wheels (Figure 2.4)

Chapter 6 : Automation with speed and trajectory control

After the mechanical comparison and analysis, the implementation of the automation will be described in this chapter. As from now, the two remaining viable aircraft configurations are:

- The A320 with a directional nose wheel and 4 electrical motors powering each main gear wheel.
- The A320 also with a directional nose wheel but with the thrust being provided by the aircraft turbojet engines.

To follow the prescribed track, the steered nose wheel has to be controlled. Further, at power level, each system has its own characteristics that have to be implemented. The electrical motor equipped design can accelerate and brake using the motors. On the contrary, the jet engine equipped design has to use a mix of automatic braking and jet engine thrust reduction to control its speed.

The common trajectory control system working at a given speed will be discussed first, followed by the speed control systems. The comparison between the different aircraft behavior will be analyzed in chapter 8 in order to take into account the electrical aspects of chapter 7.

6.1 The common trajectory control system

The trajectory controller has to adjust not only the orientation of the nose wheel steering but also the orientation of the aircraft around the yaw axis (i.e. vertical z-axis).

To mathematically design this controller (i.e. to find the appropriate control equations and factors), it is necessary to temporary work on a further simplified aircraft model compared to the one conceived in Robotran. For that purpose, bicycle inspired steering dynamics are used. Indeed, like for a bicycle, the nose wheel steering is actuated to cause a change in the aircraft orientation and is comparable to the front wheel of a bike.[61]

In this simplified model it is important to note that the position of the aircraft (x_a, y_a) is expressed as the position of the center of gravity (CG) of the Airbus in the inertial frame. It can be compared to geographic coordinates (x_a, y_a similar to latitude and longitude) relative to a geographic airport reference point, e.g. the central position of the airport defining the origin of our inertial frame, O=(X=0, Y=0). The illustration of the frame is visible in Figure 6.1 with the red bullet indicating the center of gravity positioned in the XY inertial frame.

The following assumptions are made to keep the model mathematically simple in order to design the controller.

1. The rolling without slipping condition applies for each wheel.

2. The main landing gear wheels (i.e. rear wheels) are approximated by a single wheel at the center of the aircraft.
3. The nose landing gear wheels are approximated by a single wheel placed on the longitudinal axis of the aircraft.
4. The simplified main landing gear wheel velocity is v_0 and v stands for the specific forward speed of the CG.

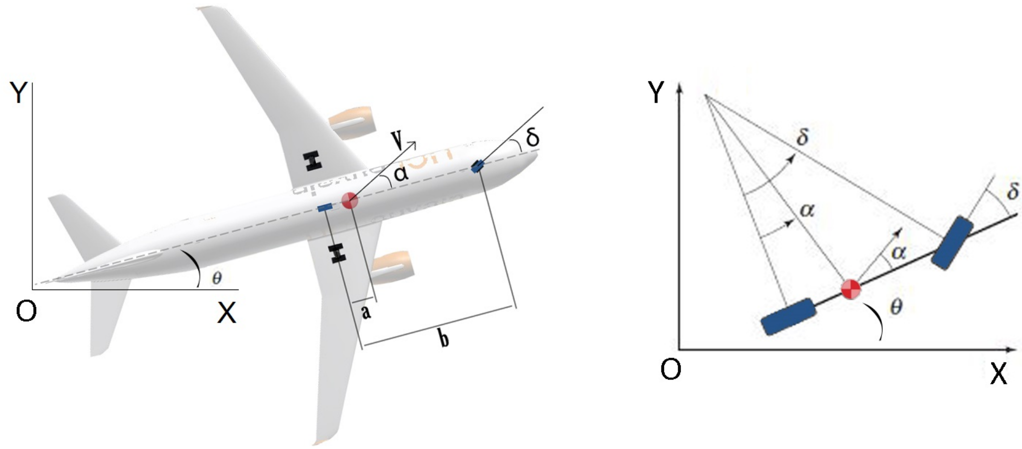

Figure 6.1: Aircraft steering dynamics simplified to a bicycle model

in regards with those assumptions, the model uses the following variables: δ the steering angle, a the distance between rear wheels and CG, b the wheel base[1], θ the yaw angle[2], α the angle between the velocity vector and the longitudinal axis of the aircraft and R_{turn} the radius of the turn.

With all those assumptions and notations, we can now define the state equations. The objective is to obtain a linear automatic system which is mathematically easier to work with in order to design the controller.

6.1.1 State equations

Initially, by trigonometry (Figure 6.1), the following relationship between α and δ can be found by knowing that $b = R_{turn} \cdot tan(\delta)$ and $a = R_{turn} \cdot tan(\alpha)$ leading to $tan(\alpha) = \frac{a}{b} tan(\delta)$.

$$\alpha = tan^{-1}\left(\frac{a \cdot tan(\delta)}{b}\right) \tag{6.1}$$

Dynamics equations

The aircraft speed at the CG is $v = \frac{v_0}{cos\alpha}$ so that the velocities $\dot{x}_a$, $\dot{y}_a$ and $\dot{\theta}$ are given by :

$$\frac{dx_a}{dt} = vcos(\alpha + \theta) = v_0 \frac{cos(\alpha + \theta)}{cos\alpha} \tag{6.2}$$

$$\frac{dy_a}{dt} = vsin(\alpha + \theta) = v_0 \frac{sin(\alpha + \theta)}{cos\alpha} \tag{6.3}$$

$$\frac{d\theta}{dt} = \frac{v_0}{R_turn} = \frac{v_0}{b} tan\delta \tag{6.4}$$

[1]longitudinal distance between front and rear wheels
[2]Orientation of the aircraft in the track frame

Linearization around the equilibrium point

To linearize those equations, a specific *target* condition is chosen so that the differential equations equal to zero, i.e. a condition where no variation exists anymore: the *equilibrium point*.

$$\frac{dx_a}{dt} = \frac{dy_a}{dt} = \frac{d\theta}{dt} = 0 \tag{6.5}$$

Here, the equilibrium point is defined so that the aircraft is travelling along a straight line track aligned with the X axis and has a certain velocity so that $v_0 \neq 0$. At the equilibrium point, we have $\dot{\theta} = 0$ and $\delta = 0$ which means that $\alpha = 0$ as well.

However if we look at the two first dynamics equations ($\dot{x}_a$, $\dot{y}_a$) we can never reach equilibrium because at the equilibrium point we end up with $\dot{x}_a + \dot{y}_a = v_0 \neq 0$. Therefore we have to consider to work only with the lateral deviation from the track. The goal becomes to cancel the lateral deviation and obtain $\theta_{equil} = 0$ aligned with the track.[61]

Nevertheless, the track can be oriented at any angle θ_{ref} in frame X, Y. This means that a frame change has to be made in order to reset $\theta_t = 0$ when the yaw of the aircraft is aligned with the track (Figure 6.2). To simplify the notation in the following explanations, the lateral deviation will be expressed as y, referring to the distance between the CG of the aircraft and the track X_t axis.

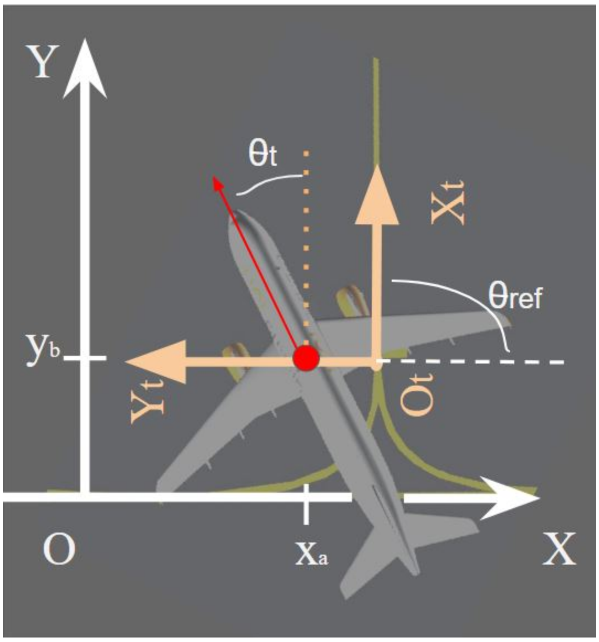

Figure 6.2: Frame alignement with the track. The objective becomes to cancel the lateral deviation

The system is then limited to the variations of the lateral position y and of the yaw angle θ_t. The state variables are $X = (y, \theta_t)$. The single input variable U is the nose wheel steering angle δ, $U = \delta$. Here, we assume that those state variables data are provided by the dynamics computation of the elaborated model implemented in Robotran. The state functions can be written as :

$$f(X,U) = \begin{pmatrix} v \cdot sin(\alpha(U) + X_2) \\ \frac{v_0}{b} tan(U) \end{pmatrix} \qquad h(X,U) = X_1 \tag{6.6}$$

with $\alpha(U) = tan^{-1}\left(\frac{\alpha \cdot tan(U)}{b}\right)$

The linearized system is described by the state equation $\dot{X} = AX + BU$ and the output equation $Y = CX + DU$. The matrices A,B,C,D are found by deriving $f(X,U)$ and $h(X,U)$ around the equilibrium point ($X = (0,0)$,$U = 0$).

$$A = \frac{\partial f}{\partial X}\Big|_{equil} = \begin{pmatrix} 0 & v_0 \\ 0 & 0 \end{pmatrix} \qquad B = \frac{\partial f}{\partial U}\Big|_{equil} = \begin{pmatrix} \frac{a}{b}v_0 \\ v_0\frac{1}{b} \end{pmatrix}$$

$$C = \frac{\partial h}{\partial X}\Big|_{equil} = \begin{pmatrix} 1 & 0 \end{pmatrix} \qquad D = \frac{\partial h}{\partial U}\Big|_{equil} = 0$$

Normalized linear model

To obtain a linear system with only one parameter, we can further simplify the model: the wheel base b becomes the length unit and the time to travel b becomes the time unit $\tau = t\frac{v_0}{b}$. [61] The normalized state z becomes $z = (\frac{X_1}{b}, X_2)$ and the input notation $u = \delta$. The state equations with $\gamma = \frac{a}{b}$ is then written [3]:

$$\dot{z} = \begin{pmatrix} z_2 + \gamma u \\ u \end{pmatrix} \tag{6.7}$$

The linearized system is now described by the state equation $\dot{z} = Az + Bu$ and the output equation $y = Cz + Du$. The matrices A,B,C,D are the following:

$$A = \begin{pmatrix} 0 & 1 \\ 0 & 0 \end{pmatrix} \qquad B = \begin{pmatrix} \gamma \\ 1 \end{pmatrix}$$

$$C = \begin{pmatrix} 1 & 0 \end{pmatrix} \qquad D = 0$$

6.1.2 Reachability or controllability

Before implementing a controller, we have to ensure that the system is controllable or reachable by checking that the matrix W_r of the system is of full rank, i.e. that its determinant is not zero:

$$\det(W_r) = \begin{vmatrix} B & AB \end{vmatrix} = \begin{vmatrix} \gamma & 1 \\ 1 & 0 \end{vmatrix} = -1 \neq 0$$

In the present case, the system is controllable.

6.1.3 State feedback Controller

From the system just described and linearized[4], we will now implement a controller that would be able to follow a prescribed trajectory. The first step will be to follow any straight track but we will see afterwards that the track can become more elaborated to finally represent a real taxiway with its curves. The controller will be a state feedback controller because we can reasonably assume that the aircraft sensors[5] can provide data on the two specified state variables.

The objective of the controller is to reach and keep a zero lateral deviation $\Delta y = 0$ and the correct yaw angle θ_{ref} corresponding to the track orientation in the reference frame. The control law of the linear feedback is function of the state variables (z) and the reference value (r). The negative sign of K indicates the negative feedback.

$$u = -K \cdot z + k_r \cdot r \tag{6.8}$$

[3] a and b defined in Figure 6.1

[4] Under the assumption that the aircraft was travelling at constant speed with an equilibrium point corresponding to a straight line

[5] The aircraft is equipped with inertial platforms providing magnetic heading and geographic position to the aircraft.

The closed loop system with the feedback becomes:

$$\dot{z} = (A - B \cdot K)z + B \cdot k_r \cdot r \tag{6.9}$$

To define the value of the feedback gain K, the determinant of (sI-A+BK) has to be calculated ($\gamma = \frac{a}{b}$ see Figure 6.1).

$$det(sI - A + B \cdot K) = \begin{vmatrix} s + \gamma k_1 & 1 - \gamma k_2 \\ -k_1 & -k_2 \end{vmatrix} = s^2 + (\gamma k_1 + k_2)s + k_1 \tag{6.10}$$

By comparing this polynomial with the general characteristic polynomial $p(s) = s^2 + 2\zeta\omega_n s + \omega_n^2$, the factor K can be estimated.

$$k_1 = \omega_n^2 \quad , \quad k_2 = 2\zeta\omega_n - \gamma\omega_n^2 \tag{6.11}$$

where k_r is not affecting the stability of the system (i.e. this is the reason why it was not included in the polynomial found above) but does affect the steady-state output. It can be found by the following formula and in this case $k_r = k_1 = \omega_n^2$ [61]:

$$k_r = \frac{-1}{C(A - BK)^{-1}B} \tag{6.12}$$

Thus the controller has the following final shape :

$$u = k_1(\Delta y) - k_2(\Delta yaw) \tag{6.13}$$

The values of the general characteristic polynomial factors (ζ and ω_n) can be found in tables (Figure 6.3) and determine the overshoot percentage (D) and the time response for a step input that we desire for our system [22]. The time response is defined as the time from the start of the step input until the response remains within 2% of its final value and this happen when [62]:

$$e^{-\zeta\omega_n T_r} < 0.02 \implies \zeta\omega_n T_r \approx 4 \tag{6.14}$$

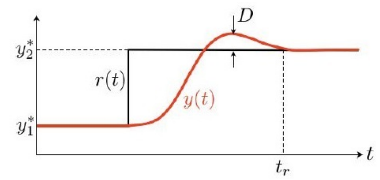

	$0 < \zeta \leq 1$	$1 < \zeta$
t_r	$\frac{4}{\zeta\omega_n}$	$\frac{4}{\omega_n(\zeta - \sqrt{\zeta^2 - 1})}$
D	$100 \exp\left(\frac{-\zeta\pi}{\sqrt{1-\zeta^2}}\right)$	0

ζ	D
0.25	40%
0.4	25%
0.5	18%
0.6	10%
0.7	4.5%
0.8	1.5%
1.0	0%

Figure 6.3: Polynomial characteristic factors determination tables [22]

First, the overshoot percentage is chosen providing the value of ζ. ω_n is then deduced by the targeted time response, $t_r = \frac{4}{\zeta\omega_n}$ when $0 < \zeta \leq 1$.

A320 trajectory controller factors and results: During real taxi operations, the aircraft speed can reach a maximum of 15[m/s] in a straight line and usually a reduced speed of 7.5[m/s] in a curve to avoid nose wheel skidding and slipping. To wisely choose the appropriate value for ζ and t_r, a first analysis is performed in straight line starting with a lateral deviation of 1[m].

Nowadays, pilots tend to smoothly align the aircraft with the taxiway center line. This behavior can be associated with a 0% overshoot corresponding to a $\zeta = 1$. The time response choice is then made based on the analysis of Figure 6.4 (top). The most appropriate time response seems to be $t_r = 8$.

However, we can imagine that some pilots are more *dynamic* than others and have a tendency to slightly overshoot the line before coming back to a perfect alignment of the aircraft on the taxiway. For that purpose, a second analysis was realized with $\zeta = 0.7$. We see in Figure 6.4 that the main difference with the case when $\zeta = 1$ is the overshoot and the shorter rising time (i.e. the time needed to go from 10% to 90% of the step value [62]). Below a certain value of time response, the overshoot percentage is increasing (e.g. $t_r = 5$ has an overshoot of nearly 20%). Moreover, with a smaller time response, the tendency is to perform a damped oscillation of larger amplitude (e.g.$t_r = 5$ curve) than the others (e.g.$t_r = 10$ curve). For those reasons, the time response of $t_r = 10$ looks to be more appropriate to simulate the so-called *dynamic pilot attitude*.

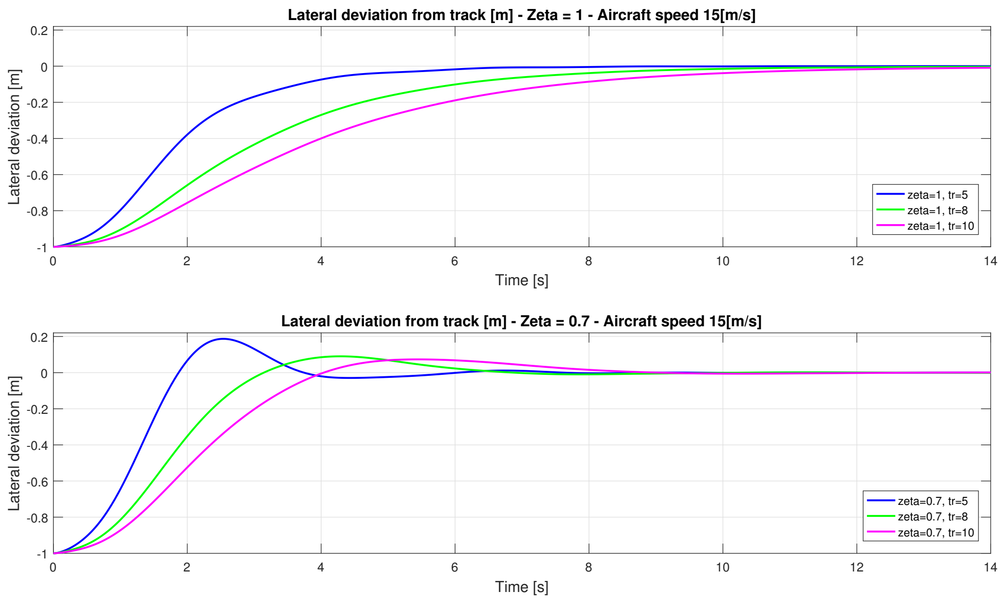

Figure 6.4: Step input of 1m lateral deviation with $\zeta = 1$ (top) and $\zeta = 0.7$ (bottom).

The main goal of the state feedback is to position the eigenvalues of the closed loop, via the controller factors k_1 and k_2, on the left part of the imaginary axis in order to get a stable system (Figure 6.5). The eigenvalues are the roots of the polynomial stated at equation (6.10). As expected, all the tested factors have negative real values (i.e. stable system).

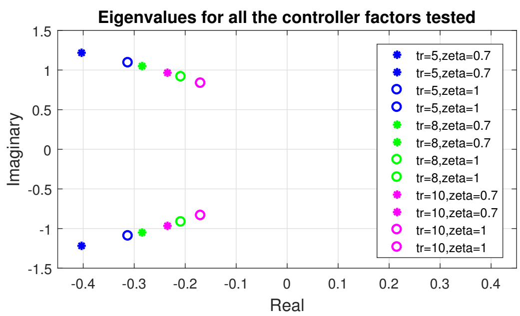

Figure 6.5: System eigenvalues

For passengers' comfort, the nose wheel is usually rotated from 0° to 45° in about 3 seconds meaning a rotational speed of about 0.26 [rad/s]. This data is an approximation of what pilots manually do. Up to now, our current system model was not limited to a specific rotational speed. Logically, the implemented feedback loop controller in association with a continuous track (straight lines and realistic curves) is not leading to excessive nose wheel steering position variations. Nevertheless, a rotational speed limiter was implemented to ensure the system never exceeds a rotational speed of 0.26[rad/s], e.g. in case the aircraft receives an inadequate 90° abrupt track change. This limiter is acting on the slope (i.e. the derivative) of the output nose wheel controller signal. Every time the derivative of the position exceeds this 0.26 value, the limiter restrict it to that value. The NWS position output signal of the limiter becomes $NWS_{position,t-1} \pm 0.26 \cdot dt$, with dt the time step and $NWS_{position,t-1}$ the previous nose wheel position. In addition, the nose wheel steering speed limiter also ensures, from an electronic point of view, that the position command signal sent to the aircraft system never exceeds the mechanical stop position of the nose wheel steering (i.e. 75° [5])

In the case of the 1[m] lateral deviation input, the results obtained when the limiter is active (continuous lines) are compared with the ones without the limiter (dash lines) (see Figure 6.6). As expected, the addition of a limiter behind the controller induces a small delay. The delay is influence by the rising time observed, thus by the response time and a low ζ. However, the stability is not affected in this specific case.

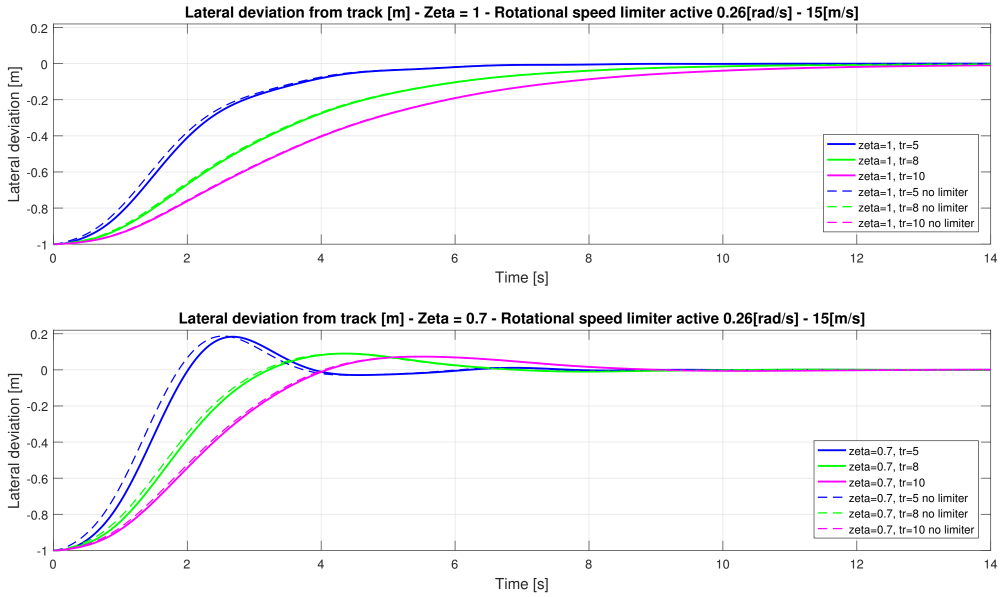

Figure 6.6: Activation of the rotational speed limiter for a step input of 1m lateral deviation with $\zeta = 1$ (top) and $\zeta = 0.7$ (bottom). Comparison with the unlimited version in dash lines

6.1.4 Identification of the needs to handle the trajectory controller

After this controller definition and the nose wheel steering speed limiter analysis, the two inputs required to this control system are

- the lateral deviation Δy
- the angle between the track and the longitudinal axis of the aircraft Δyaw

However, as we have discussed before, we need to handle the case where the track direction is not aligned with the inertial reference X axis. This block would receive the track information based on a reference point x_{ref}, y_{ref} and an orientation yaw_{ref}. With the current position of the aircraft, it would be able to provide Δy and Δyaw to the controller.

In accordance with the specifications, we know that each taxiway (i.e. the tracks) is based on 4 coordinate points. An additional block is thus required to draw the track based on those points and identify which reference point to choose to provide x_{ref}, y_{ref} and yaw_{ref} to the next block.

Finally, a selection has to be made in the database to create a sequence of several taxiways and to properly send the 4 right coordinate points to the block mentionned just before.

6.1.5 Controller sequence and process

Based on the identification done in subsection 6.1.4, the controller implemented in Simulink is composed of 4 different subsystems visible in Figure 6.7.

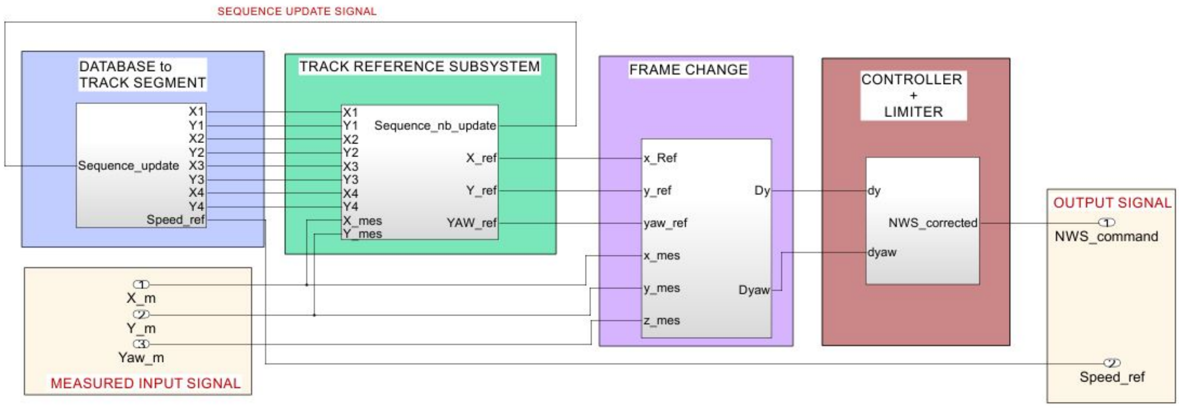

Figure 6.7: All the blocks constituting the full trajectory control process

From database to track segment subsystem

In this subsystem, a sequence of taxiways, each composed of 4 different geographic coordinates and a speed reference, is extracted from the database. Only one taxiway segment (i.e. the 4 points) is provided at a time to the next block. The appropriate taxiway is selected in regards with the *sequence update signal* received from the track reference subsystem (subsection 6.1.5). A sequencing number is generated by a counter reacting to the *signal* (i.e. every time the aircraft is approaching the end of the actual taxiway segment, the sequencing number increases) (Figure 6.8).

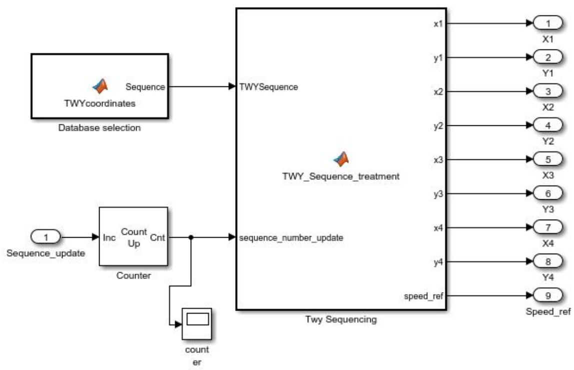

Figure 6.8: Simulink diagram of TWY sequencing subsystem

In this study, the assumption is made that the first segment of the taxiway sequence corresponds to the segment on which the aircraft is. When the last segment in the sequence is reached and the counter is incremented one more time, the last segment information is still sent but the reference speed is forced to zero.

Indeed, for each segment, a maximum speed is defined. This information is directly forwarded to the speed controller system (section 6.2).

Track reference subsystem

This subsystem receives the track segment defined by 4 points (x_i,y_i with i =1,2,3,4). To simplify the building of the entire track, the first point (x_1,y_1) and the last one (x_4,y_4) are the edges of the track segment. From those, an appropriate reference point and angle (x_{ref}, y_{ref}, yaw_{ref}) are defined by transforming the track points into a mathematical polynomial.

It is a 4 steps process:

1. Development of the track polynomial $y = a_1x^3 + a_2x^2 + a_3x + a_4$. It is important to check the orientation of the track. If track is going north or southbound, a rotation of the axes by $\pi/2$ is necessary (i.e. change of x_i into y_i and y_i into x_i) as illustrated in Figure 6.2.
2. Search for the cubic polynomial coefficients values (a_1,a_2,a_3,a_4) passing through the four points defined track.
3. Identification of the closest point of this track polynomial in regards with the actual aircraft position, i.e. tracking the smallest distance separating the aircraft and the track :
   (a) The equation of the distance is determined by :
   $$fun = \sqrt{(x_a - x_{track})^2 + (y_a - (a_1x_{track}^3 + a_2x_{track}^2 + a_3x_{track} + a_4))^2}$$
   (b) The extraction of x_{ref} [6] from the distance equation is done by using *fminbnd* function in Matlab.[63]
   (c) y_{ref} is calculated by replacing x_{track} by x_{ref} in the equation :
   $$y_{ref} = a_1x_{track}^3 + a_2x_{track}^2 + a_3x_{track} + a_4$$
   In case the track was detected as north-southbound (as mentioned in first step), the values need to be replaced in the inertial frame, i.e. rotate the axes back by $-\pi/2$.
4. The last step is to calculate the yaw_{ref} through the derivative of the polynomial at the point of reference, i.e. the slope of the track in the inertial reference. To obtain the angle,
   (a) Calculate the arctan of the slope
   (b) Analyze if the aircraft wants to travel the track east, west, south or north.
   (c) Apply appropriate correction to proceed in the right direction, e.g. adding or subtracting π or $\pi/2$.

Once the system detects that the aircraft is approaching the end of the taxiway segment, the *sequence update signal* is sent to request the next taxiway segment.

Frame change subsystem

As the objective of the controller is to follow any track and not only straight lines, it means that the yaw_{ref} (i.e. the direction of the track or θ_{ref} in Figure 6.2) could be different from 0 depending on the reference point chosen along that track. On top of that, the lateral deviation Δy is also dependent on yaw_{ref}. By definition the lateral deviation is always perpendicular to the direction of the track.

This complexity was solved by creating a new reference frame (X_t,Y_t) with its origin (O_t) placed on the reference point along the track(x_{ref},y_{ref}), visible in Figure 6.2.

[6]the value of x_{track} that minimises the value of fun)

This subsystem is calculating the lateral deviation Δy between the position of the aircraft (x,y) and the reference point along the track (x_{ref},y_{ref}) as well as the angle difference Δyaw between the actual yaw and the reference yaw_{ref}. Those values are feeding the Nose Wheel Steering Controller subsystem.

Nose Wheel Steering Controller with the rotational speed limiter subsystem

The algorithm implemented in this subsystem is the one explained here above where the nose wheel steering position, $u = \delta = k_1 \cdot \Delta y - k_2 \cdot \Delta yaw$, is sent to the aircraft model via the nose wheel steering velocity limiter.

Due to the assumption that the inertia of the nose wheel steering is small compared to the one of the aircraft, the velocity and the acceleration are not provided to the model. Only the position is provided to the driven joint by the controller. As a consequence, to avoid unrealistic and abrupt changes, the position command of the controller is limited in speed.

In the rotational speed limiter block, the instant slope is analyzed by calculating the derivative of the position command function. This value is reduced to a maximum of 0.26 [rad/s]. This corresponds to a normal manual pilot input nowadays (i.e. a 45° variation in 3 seconds).

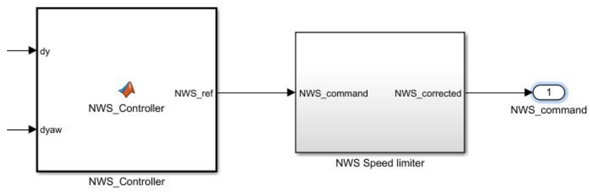

Figure 6.9: Controller and rotational speed limiter

6.1.6 A320 pushback

During the pushback procedure, the system has to deal with negative aircraft speeds. The controller remains basically the same. Only minor changes were required so that the system could understand that the aircraft was traveling backwards, e.g. inverse the deceleration and acceleration limitation values.

The major challenge was to keep the $\theta_r ef$ in the forward direction and not in the travel direction. Some modification were required in the frame change subsystem to turn the $\theta_r ef$ by π when the system detects a negative aircraft speed.

As visible in Figure 6.10, based on the results obtained by the simulations done before, the decision was made to choose the value of $t_r = 10$ and $\zeta = 1$ for smoother interception.

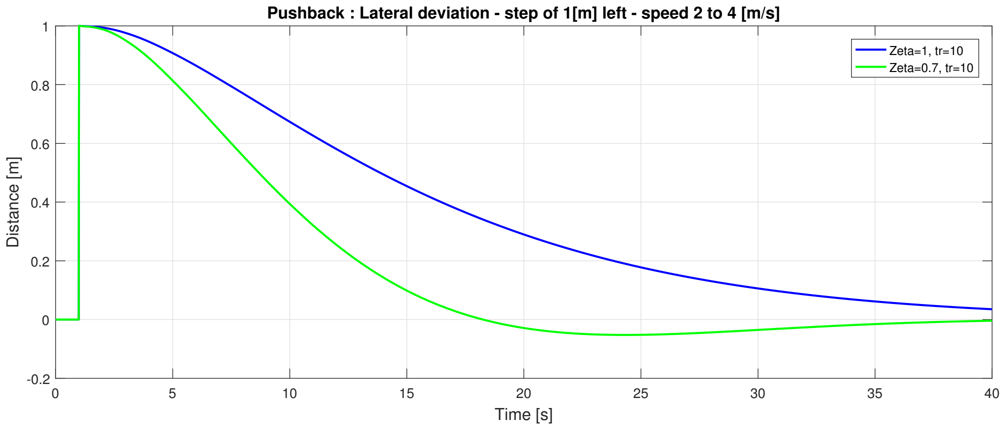

Figure 6.10: Lateral deviation step during pushback. ζ comparison

This procedure is only available with the electrical motor equipped aircraft because the jet engine cannot be used for backward motion.

6.1.7 Evaluation of the system under extreme scenario

In order to better evaluate the influence of the delay on the speed stability imposed by the nose wheel steering speed limiter, the aircraft is tested in an *extreme* case where some assumptions made previously are not fully respected anymore. Indeed, the system was initially linearized around an equilibrium point with the assumption that the state variables variations were small. A generalization of the system usage was then established in order to follow curved lines (e.g. continuous taxiways). The objective of this analysis, where the imposed variations are important, is to add a safety factor to our system. Moreover, if the system is proven to be stable in this scenario, it would be stable in any conventional ones.

In this extreme case, the aircraft speed is set to 9[m/s] slightly above the usual turn speed of 7[m/s] (i.e. a safety factor of 1.2). The track is made up of two straight lines perpendicular to each other as illustrated in Figure 6.11. The aircraft is travelling on the first track and receives the information about the next track 19[m][7]before the intersection of the two track lines (9 sec after the start of the simulation). This means that the nose wheel is 7m in front of the intersection point. It also means that the cockpit just passed (1 second earlier[8]) the start of the normal curve painted on the ground (Figure 6.11). This is thus the most realistic scenario where pilots lately realized that they had to turn. However, in that case, pilots will strongly brake to reduce the aircraft speed before turning but in our simulation the speed is kept high and constant.

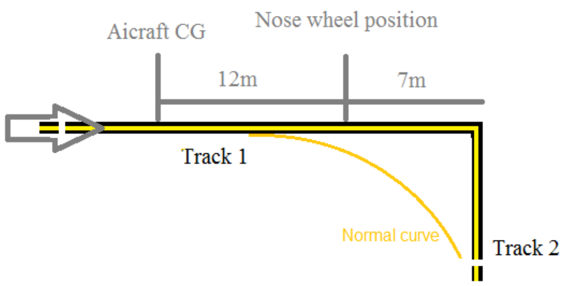

Figure 6.11: Illustration of the track used to test the influence of the induced delay onto the trajectory stability.

[8]This distance was chosen because most of the taxiway curve have a radius of 15[m].
[8]The 1 second decision time is a standard in aviation (e.g. reaction time after an engine failure during take-off roll).

The results of the lateral deviation are shown in Figure 6.12. When $\zeta = 1$ (top), the most appropriate response is done with $t_r = 8$ and $t_r = 10$. The first one, shown in green, is correcting quicker than the second one, shown in magenta, but has a tendency to overshoot the second track before stabilizing. With a time response of $t_r = 5$ shown in blue, the system is over correcting and becomes unstable. This is due to the greater delay already spotted in Figure 6.12. In the same way, when $\zeta = 0.7$, the time response $t_r = 10$ (magenta) becomes the only stable case in this extreme scenario. As previously observed, this scenario also shows the smallest delay compared to the two others.

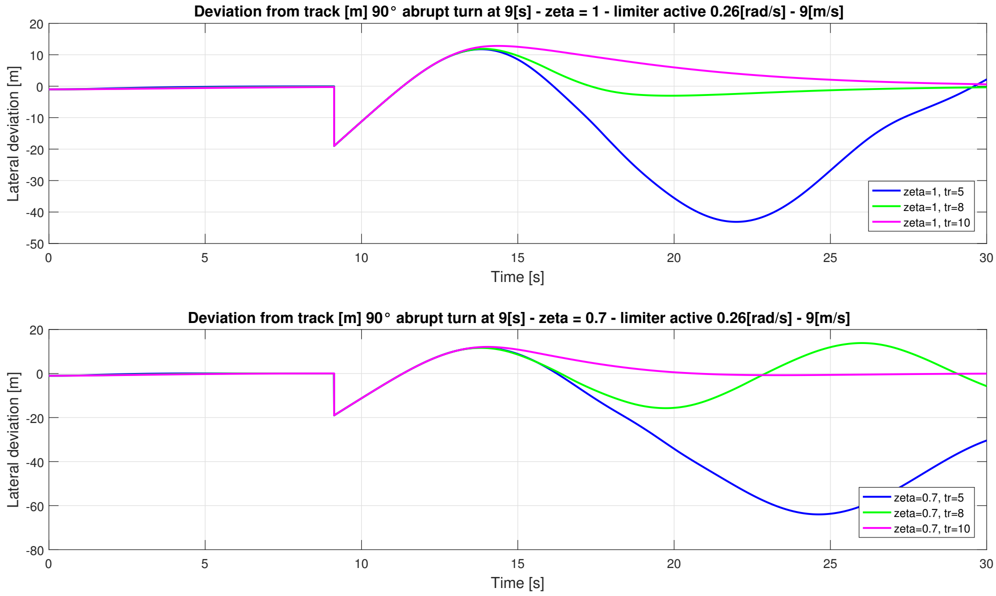

Figure 6.12: Active speed limiter for a step input of 1m lateral deviation followed by a 90° sharp turn, with $\zeta = 1$ (top) and $\zeta = 0.7$ (bottom).

In Figure 6.14, a closer view of the stable results extracted from Figure 6.12 is shown. The overshoot of $\zeta = 0.7$ with $t_r = 10$ (magenta) is less important than the one of $\zeta = 1$ with $t_r = 8$ (green) and, in addition, reached quicker a stabilized position. The $\zeta = 1$ with $t_r = 10$ (blue) is slower to react but never overshoot the track again. Depending on the desired behavior, the two remaining candidates are $\zeta = 1$ with $t_r = 10$ for smooth but slower trajectory tracking and $\zeta = 0.7$ with $t_r = 10$ for a more dynamic attitude (Figure 6.13).

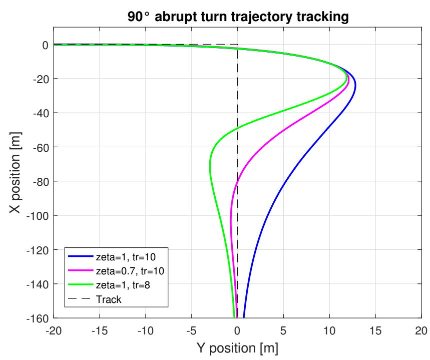

Figure 6.13: The aircraft following the track (black dash lines) for each stable configuration.

To finally choose between those two behaviors, an analysis of the nose wheel steering command signal during the scenario is carried out. In Figure 6.15, a comparison is made between the signal provided by the controller to the NWS speed limiter (dash lines) and the output of the NWS speed limiter sent to the aircraft system (continuous lines). The speed limitation is clearly visible through the slope of the continuous line. To be stable, i.e. not influenced by the induced delay, the two signals (dash and continuous lines) have to merge before passing through zero.

From another point of view, compared to $\zeta = 0.7$, it is interesting to see that the NWS command signal from the controller of $\zeta = 1$ has a larger initial amplitude (Blue dash line in Figure 6.15). This is explained by the difference in k_2 which is function of ζ (equation (6.11)). Because Δyaw is significantly larger than Δy, k_2 has a larger influence on the output result (see equation 6.13).

Because the difference in final NWS position amplitude (continuous lines) is not significant and the time to be stabilized on the track is shorter with $\zeta = 0.7$ (as seen in Figure 6.14), our decision is to choose for $\zeta = 0.7$ with $t_r = 10$ coefficient for our controller.

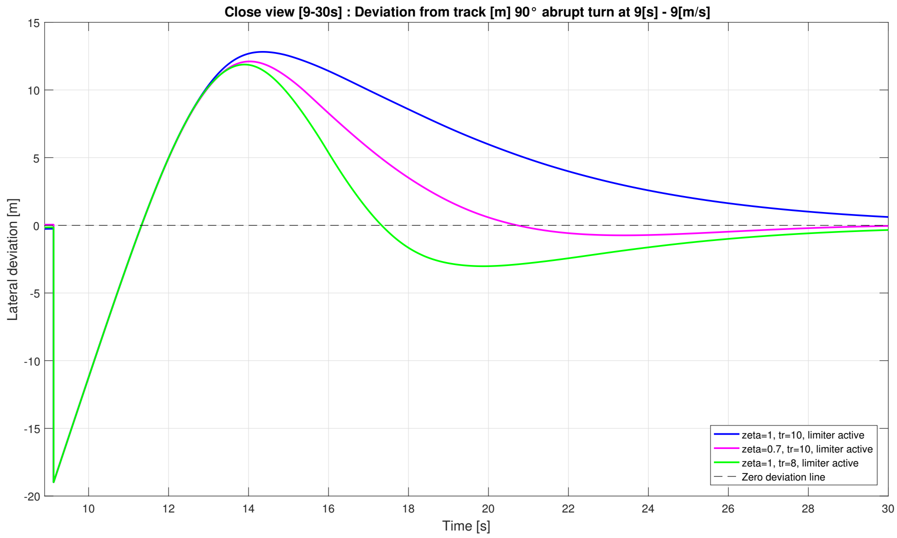

Figure 6.14: Closer view [9 to 30 seconds] of the stable results shown in figure 6.12

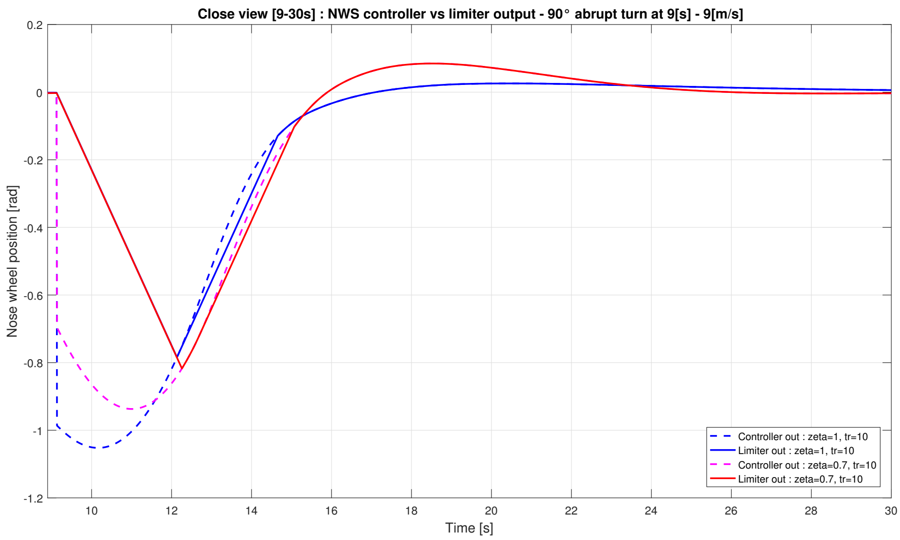

Figure 6.15: Difference between NWS controller output and rotational speed limiter output during the 90° sharp turn scenario

6.2 Speed control

Before exploring the differences between the electrical motor equipped aircraft and the jet engine powered aircraft on the ground, a common introduction of speed control is developed.

The speed control of the aircraft on the ground can be associated with a car cruise control. However, the speed range is different and is defined by the actual speed limit daily used while taxiing with an airliner[9] : -10 to 30 kts (-5,14 to 15,43 m/s).

6.2.1 Introduction : The physical equations behind the speed control

The equation of motion of the aircraft on the ground is

$$m\frac{dv}{dt} = F - F_d \tag{6.15}$$

The force F is the one generated by the aircraft through the torque of the electrical motors installed on the main wheels (or the thrust of the jet engines). The force F_d is the disturbance force composed of the gravity force F_g taking into account the slope of the taxiway, the rolling friction force F_r and the aerodynamic drag F_a.

For electrical equipped aircraft, the force equation can be written as:

$$F = 4\frac{n}{R}T_m(\omega)$$

with n the gear reducer factor, R the main wheel radius and T the torque per electrical motor. For the jet engines taxi, F equals the thrust provided by the aircraft.

In both case, the disturbance force is developed as follows [61]:

$$F_d = f_g + F_r + F_a = mg \cdot sin(\phi) + \mu_r \cdot mg \cdot sgn(v) + 1/2\rho C_d A v^2$$

with μ_r the rolling friction coefficient (0.01 for a heavy truck on concrete [12]), C_d the aerodynamic drag coefficient and A the frontal area of the aircraft. The rolling friction force is included in the Bakker model. The aerodynamic drag is not included in this study because of the unknown and complex frontal area of the aircraft. The aerodynamic shape of the nose of the aircraft could be analyzed through fluid mechanics but this is outside of the scope of this global approach. Once A is determined, the implementation of this aerodynamic drag in the system is done by creating an external force into the *MBSysPad of Robotran.* The position of this external force can be set either at the nose position of the aircraft, either at the center of gravity. The force equation is then implemented through *Visual Studio* in C language and linked with the forward speed of the aircraft.

State equation

To design our controller, we simplify the model by working on a zero slope taxiway, without any aerodynamic drag and with an aircraft travelling forward. The state equation becomes :

$$\dot{v} = \frac{F}{m} - \frac{Fd}{m} = \frac{F}{m} - g\mu_r \tag{6.16}$$

The state variable and the output variable are both the speed v and the input is the force F

[9] Large passenger aircraft

Controller general shape

The controller is a proportional-integral feedback controller. The general shape of the controller looks like :

$$u(t) = k_p(v_{ref} - v(t)) + k_i \int_0^t (v_{ref} - v(\tau))d\tau \tag{6.17}$$

6.2.2 The speed controller for an electrical motor equipped aircraft

The speed control system can be divided into three different levels (shown in different colors in Figure 6.16).

1. High level control (green box)
2. Low level control (magenta box)
3. Electrical motor control (blue box = the subject of next chapter)

In summary, the aircraft speed reference is sent to the *high level control* which analyzes and adjusts the signal to respect to the different criteria (e.g. comfort, ICR). Once corrected, the signal is subdivided for each main wheel and sent to the *low level control* which transforms the speed command into controlled torque reference signals. Those resulting signals are transferred to the electrical motor to deliver the requested torques and to obtain the requested aircraft speed.

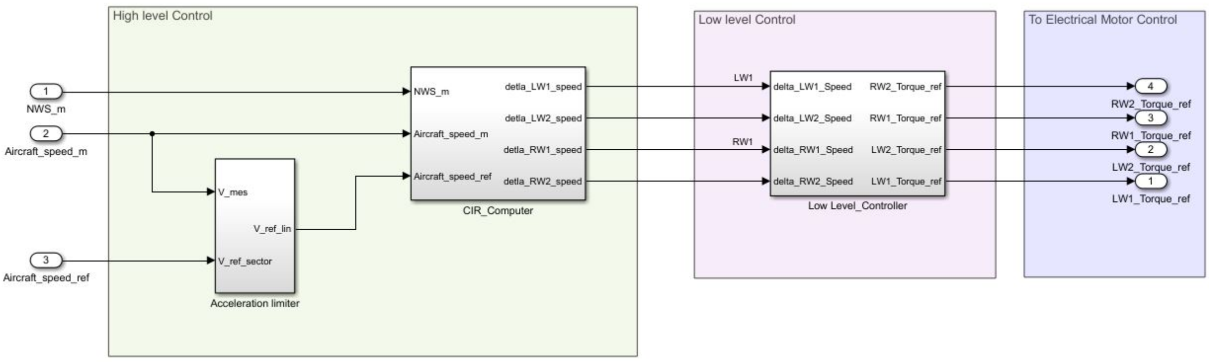

Figure 6.16: The different levels of speed controller for the electrical motor equipped aircraft

Low level control

Each main landing gear wheel is equipped with an electrical motor providing torque to the wheel and consequently inducing its rotation. Thanks to the design of the trajectory control and the respect of the ICR criteria, the speed of each wheel can be different. The speed control has accordingly to be duplicated for each wheel and has to work separately. The speeds of equation 6.17 (v_{ref} and $v(t)$) naturally refer to the selected wheel reference speed and measured speed (Figure 6.17). The output of the controller is the reference torque to be sent to the electrical motor controller developed in the next chapter.

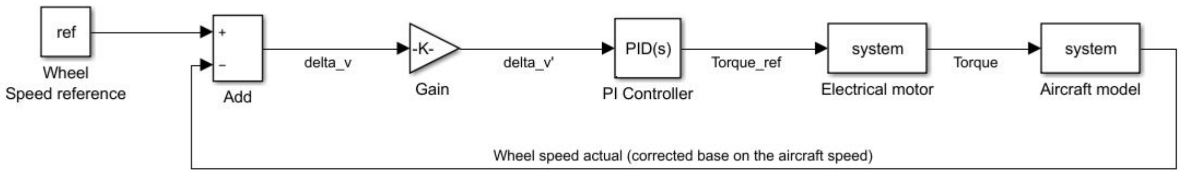

Figure 6.17: Structure of the wheel speed controller on an electrical equipped aircraft (low level control with the electrical motor and the aircraft model illustration)

The coefficients kp and ki are equivalent for each wheel speed controller and were found via a trial and error approach to get a maximum overshoot of 5% and a time response of about 5 second for a step on the speed (1m/s). To easily fine-tune the controller coefficient, it was decided to already apply a gain of 4.5e3 at the controller input. With a kp = 4, a ki of 0.9 was finally chosen for the good compromise between overshoot and steady state error correction as seen in Figure 6.18.

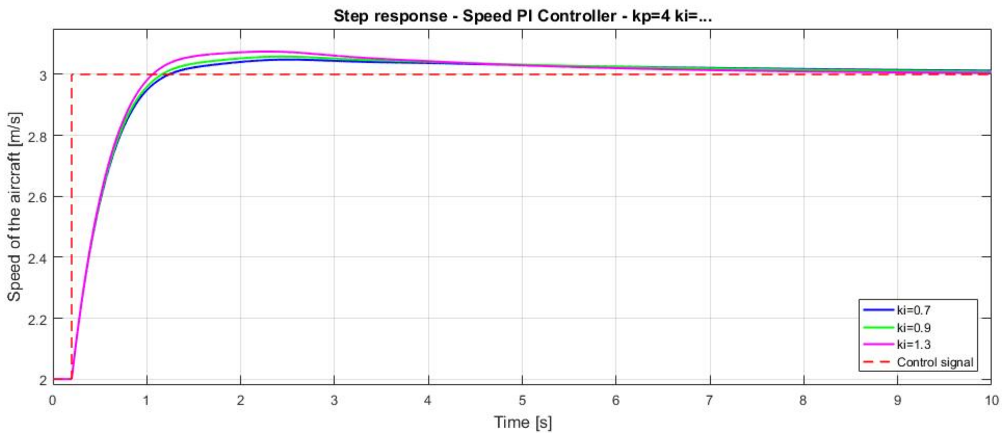

Figure 6.18: Overshoot choice to keep it below the 5%

High level control

Acceleration limiter : To handle larger steps up to a maximum speed keeping the same overshoot criteria, an acceleration limiter was installed upstream of the low level control. A research was made to establish a realistic value of acceleration and deceleration that could be handled by seated passenger and walking cabin crew. The choice was made to look at the train and tram industries because the passengers can either be seated or can be walking during the journey. The values found are 1.3 m/s^2 for a normal acceleration, $-1.5m/s^2$ for normal braking and $-3.3m/s^2$ for emergency braking [64].

To apply those criteria, a reference slope has to be implemented in regards with the amplitude of the speed (reference) step. By knowing this amplitude and the acceleration criterion, a corresponding time can be deduced.

$$\Delta t = \frac{\Delta v_{ref}}{a_{criterion}}$$

By using memory boxes, the end of the time t can be monitored to level off the reference slope. In the current design, the acceleration limiter does not reconsider any reference speed change before the end of the time t. As the assumption is made that the system is only following the maximum appropriate speed and not pilots' inputs (referenced in 6.1.5), we consider that the aircraft has the time to stabilize its speed before dealing with a new speed change.

The acceleration limiter for a step from 2 to 15m/s is shown in Figure 6.19. The magenta line slope is the acceleration criteria of $1.3m/s^2$. The actual aircraft speed slope in blue never exceeds the speed limiter one and is also visible in term of acceleration in the lower part of the figure. The actual vertical accelerations are also visible in green in this figure and do not exceed $0.05m/s^2$. However it is inherent to the suspension stiffness and damping factors implemented in the model.

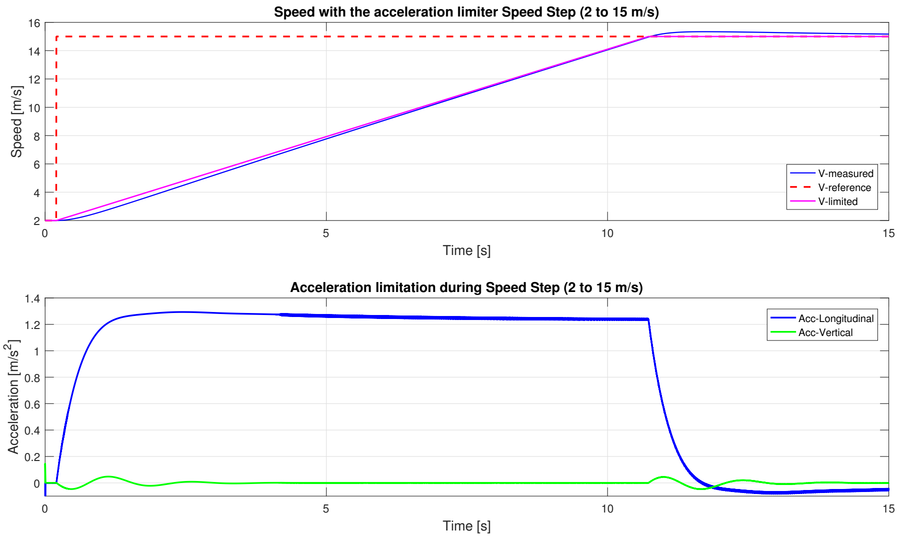

Figure 6.19: Acceleration limited to $1.3m/s^2$ in a positive acceleration.

The emergency braking is applied when the aircraft reference speed sent to the acceleration limiter module does a negative step of more than $8m/s$. The deceleration rate becomes $3.3m/s^2$ and as seen in Figure 6.20, the greater vertical acceleration (up to $+/-0.12m/s^2$) is induced by the higher compression rate of the nose landing gear suspension. Indeed, as the deceleration increases, the forward mass transfer becomes more important.

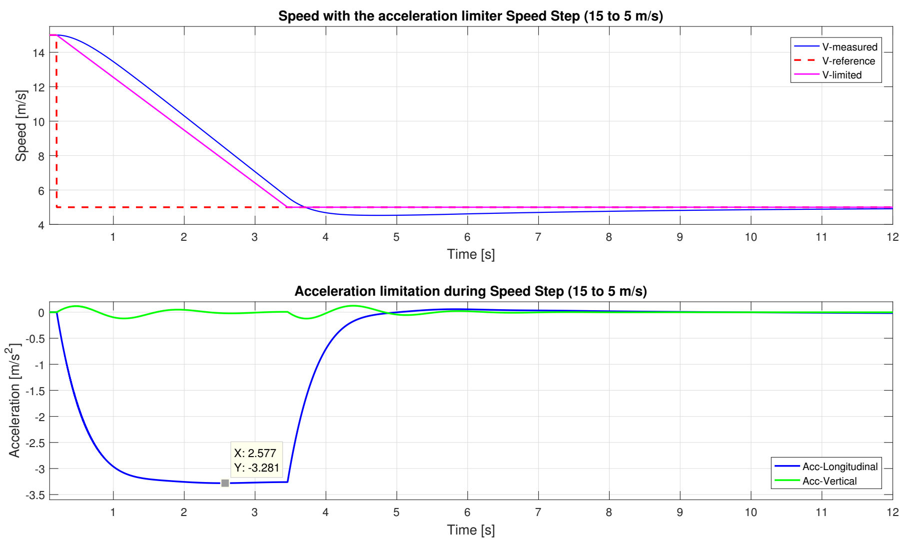

Figure 6.20: Emergency deceleration limited to $3.3m/s^2$

For smaller reference speed step (less than $8m/s$), the deceleration does not exceed $1.5m/s^2$ as visible in Figure 6.21.

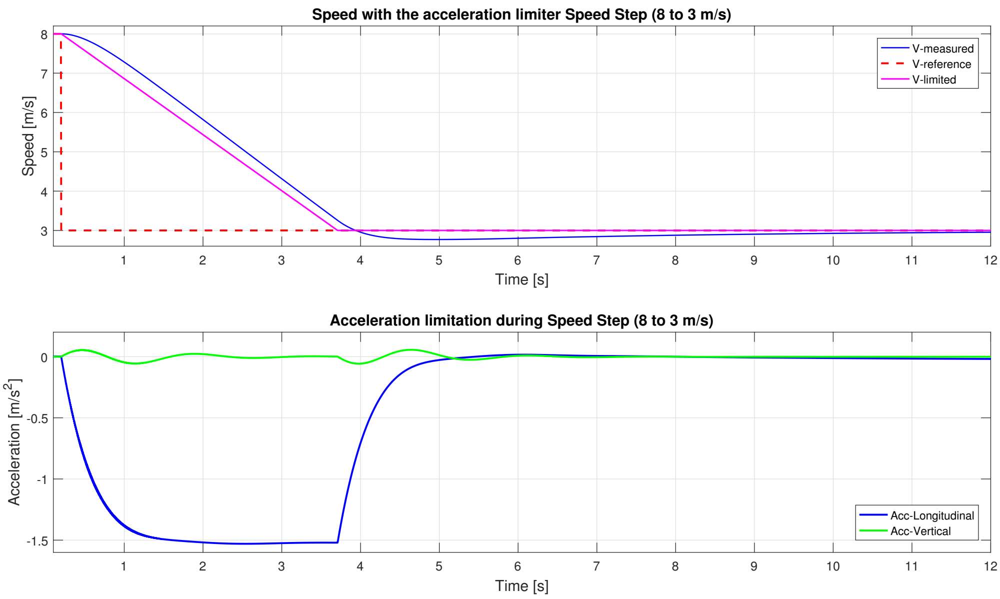

Figure 6.21: Normal deceleration for a smaller speed step limited to $1.5m/s^2$

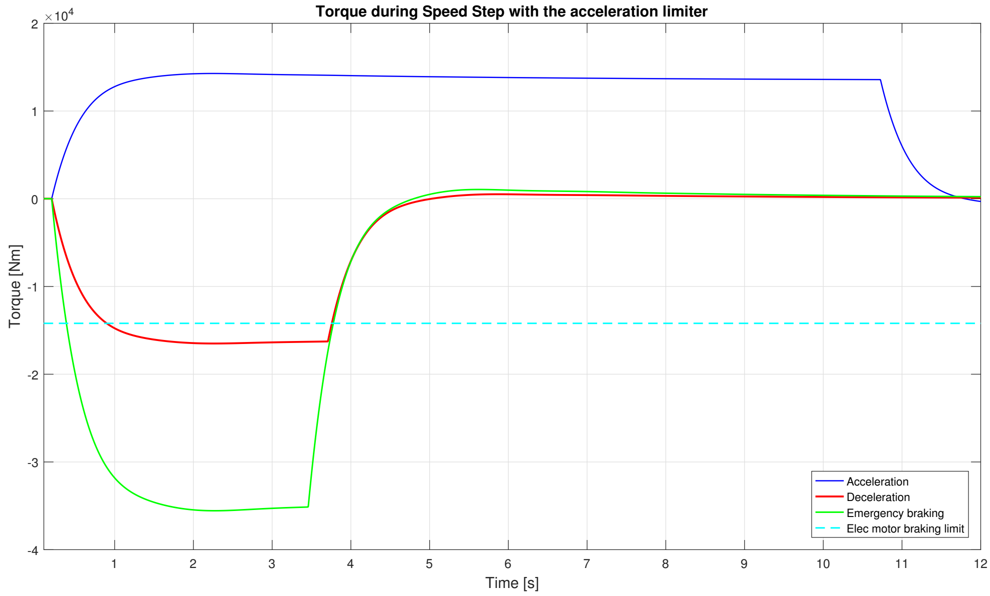

Figure 6.22: The torque applying to each wheel in all 3 acceleration/deceleration scenario's. The brakes are applied below the electrical motor negative torque limit (cyan).

With the acceleration limiter, we can observe that the maximum torque necessary to accelerate the aircraft up to its taxi speed is **14.3[kNm] per wheel** (Figure 6.22).

ICR Computer subsystem : The objective of this subsystem is to adjust the speed of each wheel in regards with the angle of the nose wheel steering, i.e. with the instant turn radius that the aircraft is following (Figure 6.23).

In addition to the nose wheel steering angle data, the subsystem receives the aircraft speed (v) and the reference speed vector (v_{ref}). Both values are used to define the actual and reference rotational speed of each wheel ($\omega_{w,actual}$ $\omega_{w,ref}$ respectively). The difference between those two speeds is sent to the low level control of each wheel.

If, a comparison was made between the reference calculated wheel speed $\omega_{w,ref}$ and the real measured rotational speed of the wheels $\omega_{w,measured}$, a static error would be observed. This error comes from the necessary longitudinal wheel slip used by our ground-tire model.

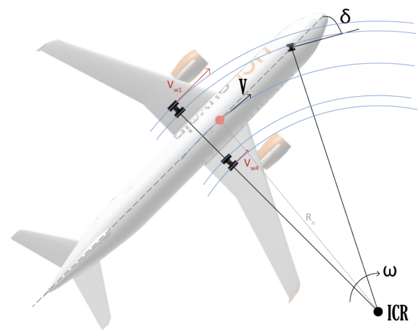

Figure 6.23: ICR criterion inducing difference in wheel speeds

Dispatcher

For the negative torque induced by deceleration as observed in Figure 6.22, the electrical motors cannot absorb all the energy. A coordination between electrical motors and brakes is required.

As seen in Figure 6.24, a dispatcher could be implemented between the low level control and the electrical motor control to allocate maximum torque to the motor and the remaining torque to the brakes.

However, in our model, this dispatcher is not implemented for computation performance reasons and because both outputs would be added before being sent to the *Joint Torque* aircraft model input (as illustrated in Figure 6.24). The only advantage to use a dispatcher in our model would be the possibility to have different controllers behaviors for brakes and electrical motors.

The energy produced by the electrical motors could be used to recharge the on-board batteries or should be dissipated through resistances. However, this is out of the scope of our study.

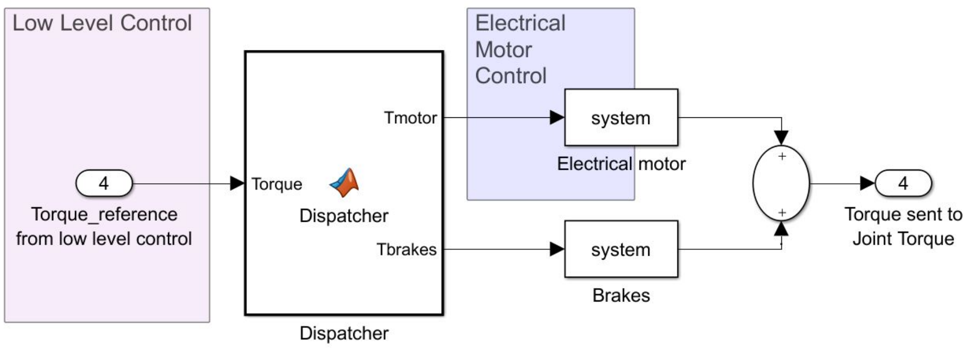

Figure 6.24: Deceleration Torque dispatch between brakes and electrical motor (for each of the 4 wheels)

6.2.3 The speed controller for the jet engine thrust taxi

The speed control of the jet engine aircraft is only divided into 2 different levels of control (shown in different colors in Figure 6.25).

1. High level control (green box)
2. Low level control (magenta box)

As for the electrical motor equipped aircraft, the aircraft speed reference is sent to the *high level control* which analyzes the signal to respect comfort criteria and compare it to the measured signal to dispatch it between brakes and the jet engine. Once dispatched, the signal of the brakes is subdivided for each main of the 4 wheels and together with the jet engine signal, they are sent to the *low level control*. Up to now the signal is just a speed (i.e. deviation between reference and measured aircraft speed). The *low level control* transforms them respectively into brake torques and jet engine thrust controlled signals. Those resulting signals are sent to the aircraft model to be respectively applied as joint torques and external forces.

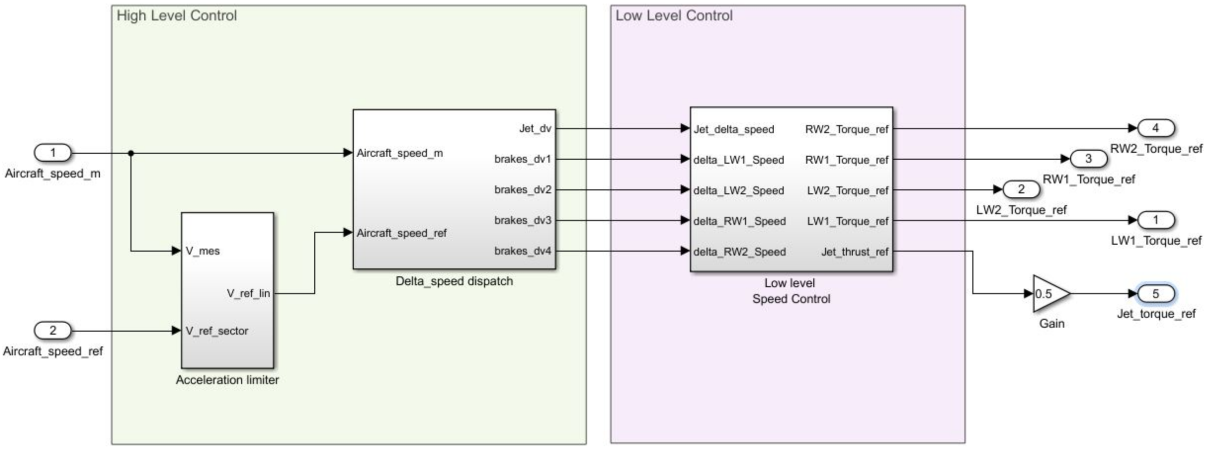

Figure 6.25: The different levels of the speed controller for an electrical motor equipped aircraft

High level control

Acceleration limiter : The acceleration limiter used in the high control of the electrical motor equipped aircraft was duplicated in this high level control level because the same acceleration criteria linked to passengers' comfort still apply.

Speed signal dispatcher : The objective of this subsystem is to dispatch the differential speed signal between jet engines and brakes to only use jet engine thrust when aircraft acceleration is needed and brakes when deceleration is needed. This avoids any thrust application simultaneously with activated brakes, i.e. transforming jet engine energy into brakes heat. However, it is important to remember that jet engine thrust cannot reach a zero value. At idle, i.e. the lowest regime possible, a small amount of thrust is created. In this model, we assume that the idle thrust is about 3450[N] per engine (Figure 6.26). Those 3450[N] representing 2.5% of the maximum engine thrust, is an arbitrary value due to the absence of this kind of information in the datasheet of the engine [55]. This constant minimum engine thrust induces constant brake use which may lead to rapid brake disk wear.

In this configuration, both jet engines are synchronized, i.e. differential thrust is deactivated, because during airline operations differential thrust is rarely used. In addition, to avoid disruptions in the trajectory control, all the brakes are applying the same negative torque.

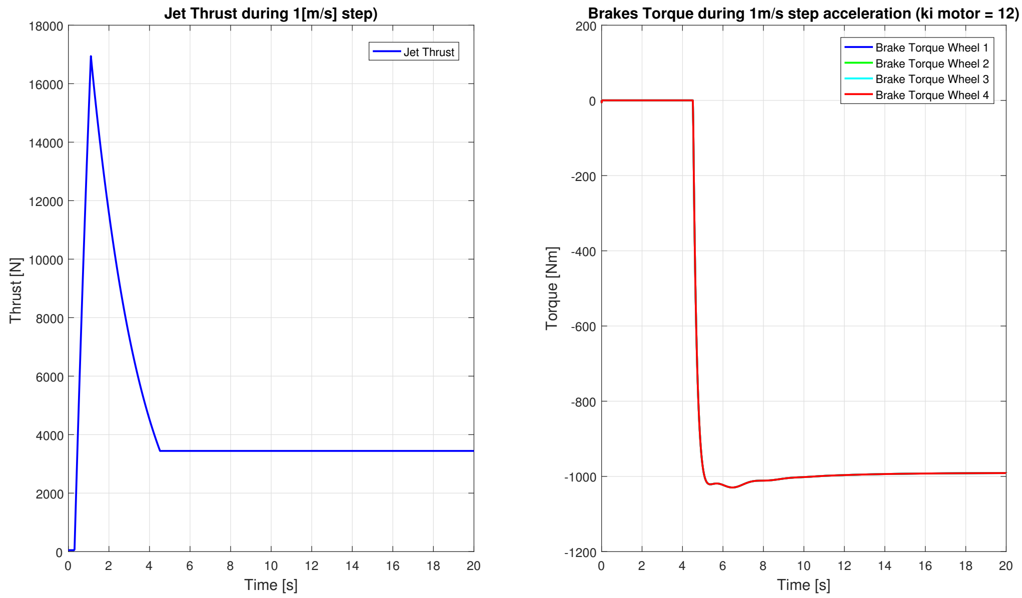

Figure 6.26: The thrust per engine and the torque per brake during a 1[m/s] acceleration step[10]

Low level control

The low level control is separated into 2 components: on one side the control of the engine thrust used during accelerations (green) and on the other the control of each wheel brake used during deceleration (red in Figure 6.27). The signal stating which one has to be used is sent by the high level control (Speed signal dispatcher).

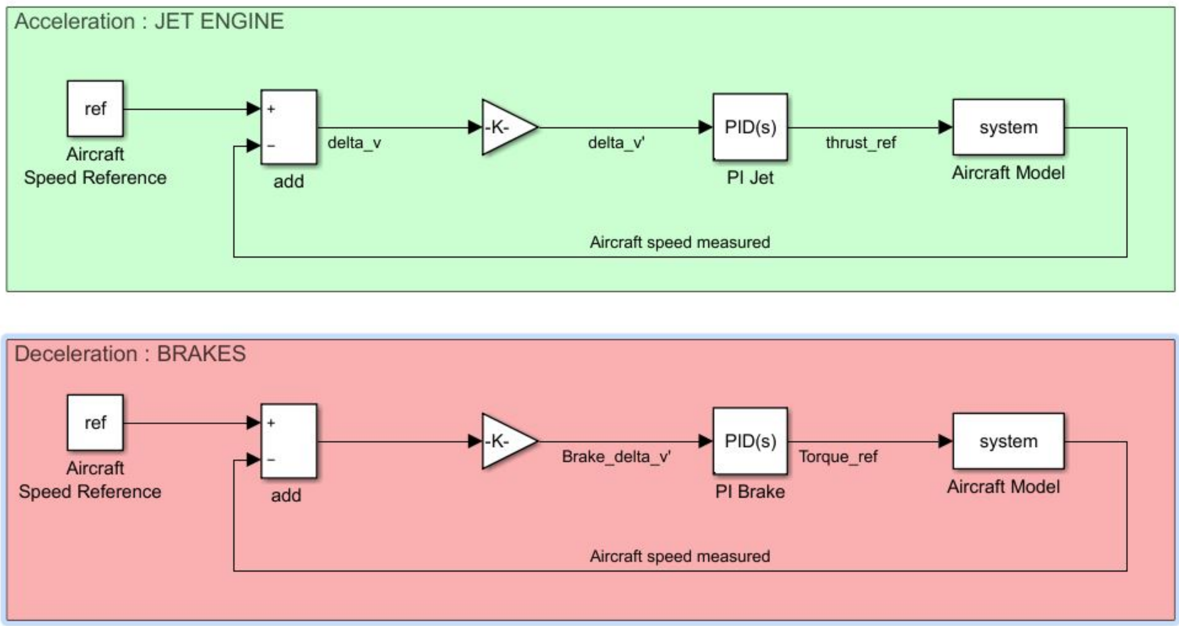

Figure 6.27: Structure of the aircraft speed controller with the separation between engine thrust and the 4 brakes torques

In case of a step acceleration, both system are working sequentially as seen on 6.26. The fact that the two series of PI controller are independent and working sequentially, in the case of a 1[m/s] aircraft speed step, the overshoot can be drastically reduced as seen in Figure 6.28. For that purpose, the PI controller coefficients of the jet engine are $k_p = 4$, $k_i = 0.5$ while the ones for the brakes are $k_p = 40$ and $ki = 12$. The integral coefficient of the brakes PI was chosen to get back to the target speed as soon as possible even if the torque applied on the brakes would be larger. It seems better for brake heat to brake harder but during a short period of time, than softer during a longer period. So, after a comparative analysis of different simulations, it was decided to choose $k_i = 12$ (Figure 6.28).

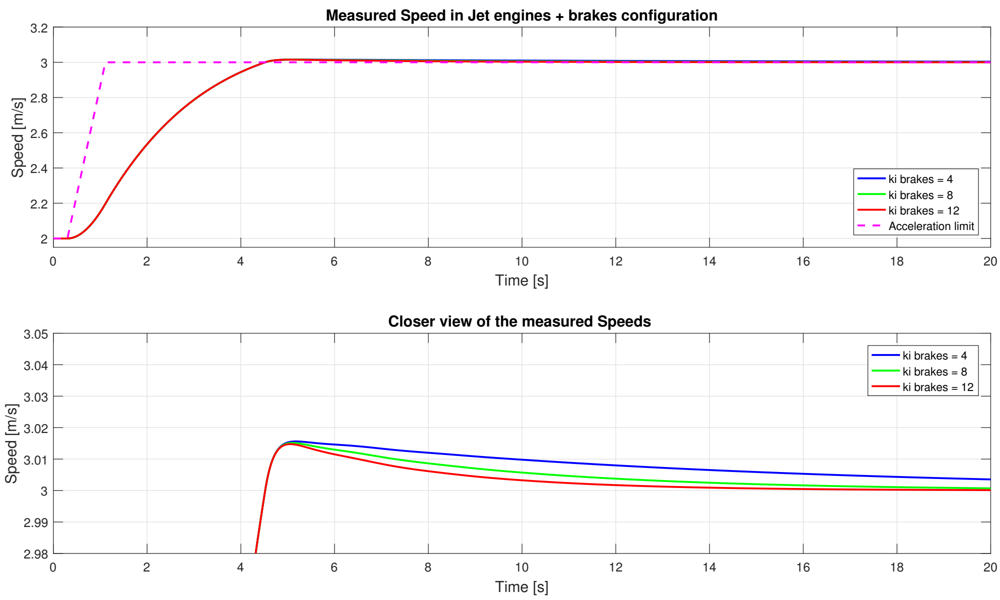

Figure 6.28: Structure of the aircraft speed controller with the separation between engine thrust and the 4 brake torques

As we can see in Figure 6.28, the maximum acceleration limit shown in magenta dashes is not closely followed by the measured aircraft speed. This behavior depends on the controller coefficient of the jet engine PI. It was decided to set low factors to keep the jet thrust below 15% of its maximum take-off thrust i.e. less than $20kN$. During taxi operations, the thrust has to be minimized as well to reduce the risk of jet blast hazards. Figure 6.29 illustrates the result of a jet blast as experimented by the BBC Top Gear team (full video sequence visible at the following link [23])

Figure 6.29: A 2CV car passing behind a Boeing 747 jet engine (BBC Top Gear experience)[23]

Chapter 7 : Electrical motors and control

In this chapter, another set of objectives will be taken up, namely the study of the electrical motor equipment. To define the appropriate motor and its control, we will first briefly navigate through the existing technologies before choosing the most relevant one for this project. A suitable controller will further be implemented in order to provide the required torque obtained in the mechanical analysis.

In this model, the aircraft can move thanks to two different force means: the thrust provided by the jet engines or the torque provided by four electrical motors. Each of those motors are connected individually to a main gear[1] wheel. Those electromechanical converters need to provide a nominal torque of 14.3[kNm] at a speed of 15m/s (25.6rad/s). The power required is thus $P = T_{em} \cdot \omega = 366kW$. But which kind of electrical motor has to be chosen ?

7.1 The different electrical motor types

In this section, the objective is to define which type of electromechanical converter best fits the A320 autonomous taxi application. Nowadays, 3 different types of electromechanical converters exist :

1. DC motors
2. Induction machine (i.e. asynchronous)
3. Synchronous machine

Let us describe these three types of converters, with a focus on their advantages and drawbacks, leading to a choice for this project.

[1] In aviation, the gear refers to landing gear, i.e. the undercarriage of an aircraft

7.1.1 DC motor

In the DC motor, the stator magnetic field is obtained tanks to magnets or electromagnets and is illustrated by the green arrow B in Figure 7.1. This magnetic field is static relative to the stator.

The rotor, composed of wires in which DC current flows, interacts with this magnetic field. Indeed, by Lorentz force equation[2], due to the current i in the winding placed inside the magnetic field B, a force F perpendicular to them is generated (equation 7.1.1 [65]. The two forces F on each side of the rotor winding generates the motor torque, e.g. this torque will be transmitted to the wheel of our aircraft through a reducer.

$$F = il \times B$$

To conduct current into the rotor windings from a static source, the DC motor is equipped with brushes and commutators. The brushes, mostly in carbon, are static and the commutators are placed on the rotor. Unfortunately, those elements are expensive and subject to wear [66]. Moreover, the current flowing at the intersection can create some spark leading to electrical losses.

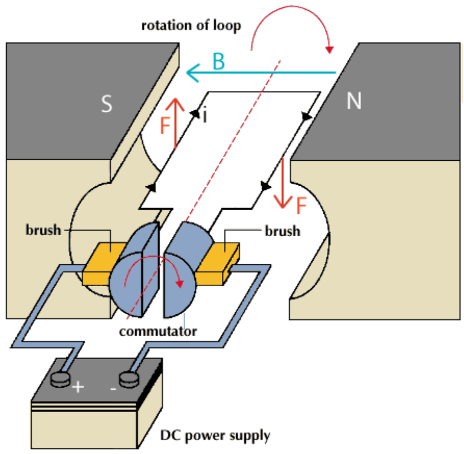

Figure 7.1: DC motor schematic with the stator magnetic field B, the current i in the rotor inductance and the reactive force F [24]

Brushless DC motors (BLDC) also exist. These motors require few maintenance and have less shaft friction, leading to a better torque-weight ratio. At equivalent performances, a smaller size can be reached with a BLDC motor. However, it needs more complex electronic control to get a precise speed regulation. Its operating mechanism is closer to a synchronous machine than a DC motor. The heat generated by a brushed DC motor is coming from the joule losses created by the current flowing into the rotor windings. It is thus more difficult to cool the whole motor down.

DC motors are often used for electrical windows, seats, and other in-cabin designs in automotive vehicles, due to their low production costs and their simple design. They are less suitable for high torque and high speed applications [24]. For these reasons, it is important to look for another kind of electromechanical converter for the aircraft motion.

7.1.2 Induction machine

In the induction machine, a rotating magnetic field is generated in the airgap, the so-called *stator magnetic field*, and is induced by triphase alternative current flowing in triphase stator windings.

The rotor is composed of short circuited windings or equivalently. Indeed most of those rotors are composed of a simpler mechanical design called *the squirrel cage*, i.e. a barrel metallic structure with longitudinal bars connected together at their extremities as seen in Figure 7.2. When there is a speed difference between the stator magnetic field and the rotor physical motion,

[2] In reality is not all the time the Lorentz force which applies on the rotor, however this explanation is one of the method used to describe the DC motor operation.

each longitudinal bar on this structure feels a variation of the stator magnetic field. Those variations induce currents in the bars that will consequently generate forces F, as illustrated by magenta arrows in Figure 7.3.

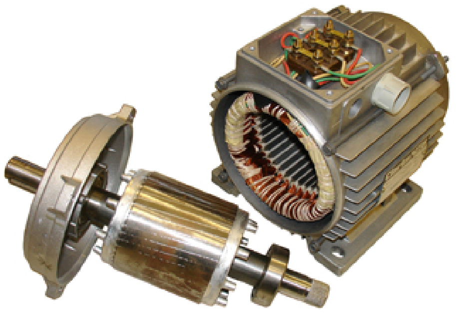

Figure 7.2: Induction machine with the squirrel cage rotor and the 3-phase stator windings [25]

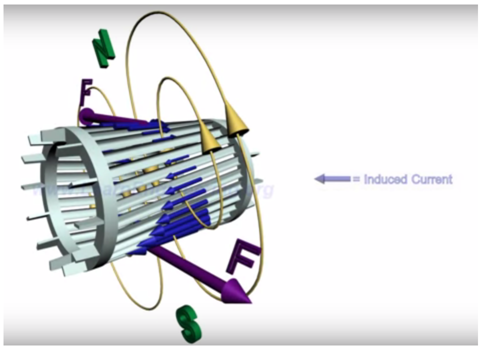

Figure 7.3: Squirrel cage with the turning stator magnetic field (yellow), induced currents i_r (blue) which induce forces F (magenta). [26]

In terms of advantages, the induction machine is cheap to produce because it does not have any permanent magnets. It is robust, it does not require much maintenance and is a self-starting machine [67]. With the assistance of power electronics, many disadvantages of the induction machine have disappeared, e.g. the variation of speed function of the load torque. However, the main drawbacks that remain are the higher weight and the larger size of those machines in comparison with the synchronous ones [68]. Unfortunately, those points are essential in our aircraft application.

7.1.3 Synchronous machine

The synchronous machine is an AC motor and has the same stator configuration as the induction machine. However the rotor is different : the rotor can be wounded to create an electromagnet with a DC current source flowing through the windings or it can be equipped with permanent magnets (PM).

The consequence of the synchronous machine is the need to obtain a rotational rotor speed (ω_m) synchronised with the rotational speed of the stator magnetic field, i.e. with the frequency of the stator current ($\omega_s = 2\pi f_s$).

$$\omega_m = \omega_{synch} = \frac{\omega_s}{p} \tag{7.1}$$

At synchronous speed, without any load applied on the motor output shaft, the poles of the rotor are aligned with the turning poles of the stator (i.e. p pairs of poles), i.e. magnetic lock position where the magnetic attraction between those poles is maximal (Figure 7.4). When load is applied, a small deviation between those poles exists but the main advantage is that the rotor speed remains constant regardless of the load.

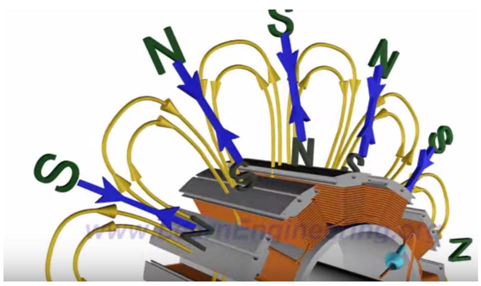

Figure 7.4: PM poles on the rotor attracted by the turning stator magnetic field (yellow) at synchronous speed [27]

However at start up, the turning magnetic field is too fast and the locking position cannot be reached. There are two solutions to cope with this problem at the start. Either power electronics are used to adjust the frequency of the stator current ω_s to values different from the grid frequency $\omega_\infty = \omega_s$. Or a squirrel cage (or damper winding) is added onto the rotor to act as an induction motor during the start until attaining the synchronous speed. The last solution being to use control electronics, which is the case for our application. This is thus not an issue.

Nevertheless, the synchronous machine can stall out of synchronous speed due to motor overload or low voltage supply or low excitation voltage (in case of wounded rotor).

The surface mounted permanent magnet synchronous machine is simpler than the wounded one and does not require much maintenance. Other PM synchronous machine configurations exist, such as interior magnets or radially inserted magnets, but as it is not the subject of this paper, we will not develop these.

The main advantages of a synchronous machine are its high efficiency, its size and its lower weight compared to the induction machine. Moreover, the *not self starting* characteristic can be handled by control electronics.

7.1.4 Motor selection for the A320 application

For all those reasons, the decision was made to implement **a synchronous machine** on each driving wheel of the Airbus A-320.

7.2 Control of the synchronous machine

The objective of this section is to detail how to implement a controller to reach any operational speed and torque for the synchronous machine.

7.2.1 General structure

The synchronous machine is powered by a 3-phase voltage source. The torque and speed are delivered to the aircraft wheel by connecting the rotor to the wheel shaft directly or through a gear reducer (Figure 7.5).

Voltage source: On the Airbus A320, this voltage source could be the 28V DC batteries of the aircraft providing AC voltage through an inverter (i.e. transformer from continuous current DC to Alternative current). However, the power capacity of those batteries is limited to 1 KVA [69]. The other electrical sources of the aircraft are the external power (i.e. a gasoline power generator connected to the aircraft while parked), the generators of each jet engine and the one of the APU[3]. Though, the external power cannot be used while moving. As the objective of electrical motors is to reduce fuel consumption, the jet engines should be considered as extinguished. The remaining potential source of energy is the APU providing triphase 115V 400Hz voltage and can provide up to 90 kVA [69], which seems powerful enough to power synchronous motors.

Physical input: Due to the fact that the APU is providing triphase voltage at a frequency of 400Hz and that the synchronous motor needs an adapted frequency f_s linked to the desired rotor rotational speed ω_m (equation 7.1), a frequency converter (power electronics) has to be inserted between the source and the machine. Without this converter the synchronous machine

[3]Auxiliary power unit: a small jet engine that can be started on battery power and which is stowed in the tail of the aircraft.

cannot be controlled. The objective of this control electronics is to perform vector control. By adjusting the amplitude and the phase of the voltage we will control the amplitude and the phase of the currents flowing into the stator windings. Those current changes induce an adjustment of the amplitude and the phase of the stator magnetic field and consequently a modification of the output torque.

Physical output: The torque obtained at the output is thus indirectly linked to the controlled voltage amplitude and phase at the output of the control electronics. The output speed depends on the torque delivered and on the load applied to the machine.

Torque Controller: The controller analyses the measured physical values (i.e. the currents, the rotor position) to deliver a reference voltage in amplitude and phase to the power electronics as illustrated in Figure 7.5.

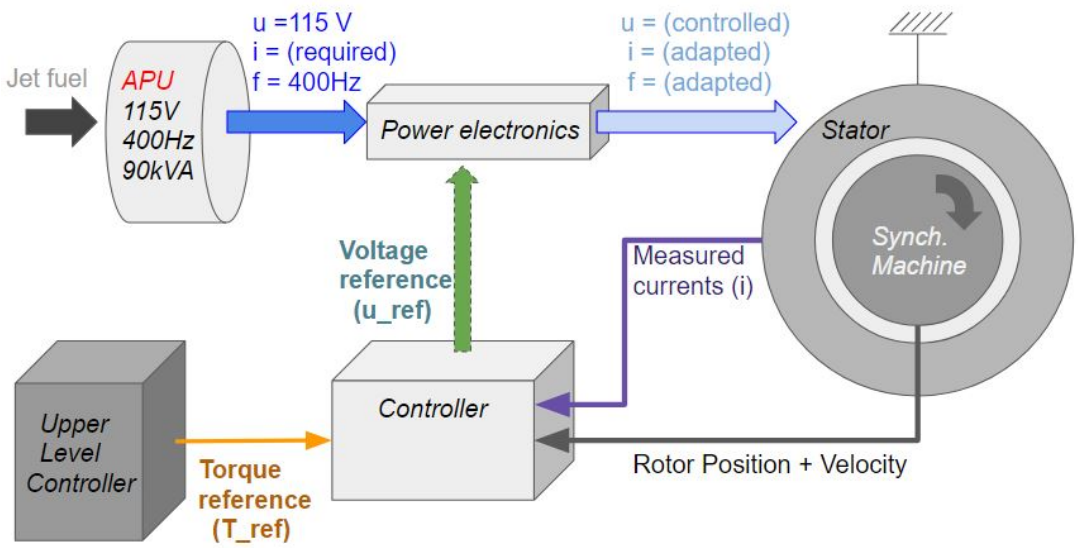

Figure 7.5: The physical connections of the synchronous machine

7.2.2 Controller implementation objectives

The next step is the implementation of a controller to obtain the precise torque reference value requested by the upper level controller, i.e. the speed controller (section 6.2). As described further down, the control of the torque based on the equations written with the physical current (i_a,i_b,i_c) is complex (equation 7.2). A mathematical simplification is necessary but is completely virtual. It does not affect the controller physical values input. The way it is done is the following :

1. Measure the physical values (i_a,i_b,i_c)
2. Convert them mathematically into virtual values more adequate to control (i_d,i_q)
   (a) Compare virtual measured currents with virtual reference currents needed to reach the reference torque
   (b) Calculate the virtual reference voltage that will induce those currents adjustments
3. Mathematically convert the virtual reference voltage into a physical reference voltage
4. Send it to the power electronics

However, due to the global approach of this master thesis and the high demanding processor resources needed to simulate the mechanical and electrical model together, we only work in the virtual reference frame without performing all the mathematical transformations. The reason behind this is the fact that the only data useful for the mechanical model is the torque extracted from the electrical model. A full "physical to virtual" conversion for voltage and current would indeed drastically slow down our simulations without providing significant additional information for our global goal. Nevertheless, we still extract the values of the measured physical currents and voltages to observe any machine over-current or over-voltage.

In the coming subsections, we will go through all the mathematical simplification steps to finally obtain the machine controller equations, to implement in Simulink, but expressed in the virtual frame.

7.2.3 Torque equation and the virtual reference frame change

In the 3-phase reference frame a,b,c (left in Figure 7.6), the torque equation of the synchronous machine is written:

$$T_{em} = -p\left(M_f sin\theta_e i_a i_f + M_f sin(\theta_e - \frac{2\pi}{3})i_b i_f + M_f sin(\theta_e - \frac{4\pi}{3} i_c i_f\right) r \tag{7.2}$$

M_f, i_f are the mutual inductance and the current of the rotor windings, θ_{em} is the position angle of the rotor.

However it will be easier to work in a 2-phase reference frame instead of the a,b,c 3-phase one. Through Concordia transformation (T), the reference frame becomes the virtual α, β frame (with the hypothesis that the homopolar component is null). The physical values (i_a,i_b,i_c) are not changed as mentioned previously. The torque equation becomes :

$$T_{em} = pM_{0f} i_f \left(-sin\theta_e i_\alpha + cos\theta_e i_\beta\right) \tag{7.3}$$

A further simplification is done by virtually aligning the stator windings with the rotor ones in order to reduce the number of mutual inductances (i.e. to see the magnetic field of the stator align or perpendicular with the rotor one). A virtual rotation of angle ξ is applied. To fix the frame dq to the rotor one and to align the d-axis with the rotor magnetic axis, we impose ξ_r to be zero, i.e. $\xi_s = \theta_{em}$ (Figure 7.6). The rotational adjustment is called the Park transformation.
The resulting torque equation is :

$$T_{em} = p\left(M_{0f} i_f i_q + (L_d - L_q) i_d i_q\right) \tag{7.4}$$

L_q and L_d are respectively the virtual inductance aligned with the q-axis and the d-axis. It can be rewritten with K_t the torque constant, mostly mentioned in the data sheet of the machine.

$$T_{em} = p\left(K_t i_q + (L_d - L_q) i_d i_q\right) \tag{7.5}$$

As a surface mounted permanent magnet synchronous machine is chosen for further simplification, $L_d \approx L_q$ and the equation simplifies to $T_{em} = p(K_t i_q)$.

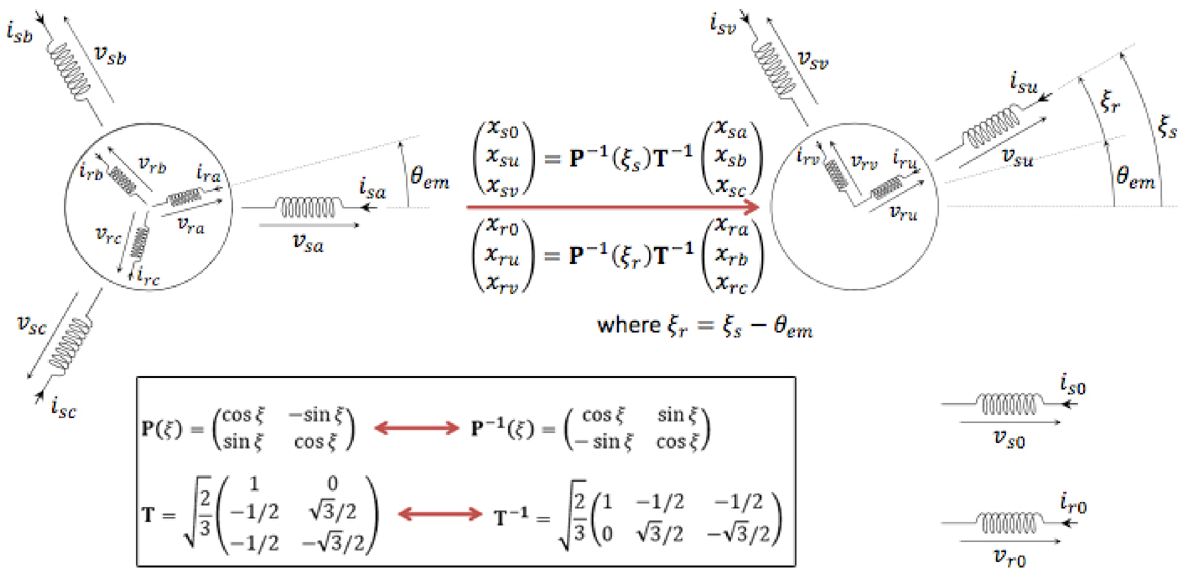

Figure 7.6: Illustration of the Concordia (T) and Park (P) transformation from abc to uv (qd) [28]

7.2.4 Control in dq reference frame

The reason behind the use of the dq frame is that the quantities to be controlled will not vary with the angular speed of the rotor movement. In addition, the dynamics of the mechanical system are assumed to be slow compared to the dynamics of the current controller. The main controller operates by considering the electrical machine as a torque source. So a torque reference T_{ref} is provided to the controller by the upper level controller (Figure 7.5). The controller transforms this reference into an current reference $i_{d,ref}$ and $i_{q,ref}$ to produce a reference voltage u_{ref} for each u_a, u_b, u_c component, as mentioned in subsection 7.2.2. The u_{ref} is then sent to the power electronics.

General equations of the system in the dq reference frame

A star-connection is imposed to the machine so that the current of the homopolar axis is physically constrained to be at zero. The voltage equations in the qd reference frame are :

$$u_d = R_s i_d + L_{os}\frac{di_d}{dt} - \omega_{em} L_{os} i_q \tag{7.6}$$

$$u_q = R_s i_q + L_{os}\frac{di_q}{dt} + \omega_e L_{os} i_d + \omega_{em} K_t \tag{7.7}$$

where $L_{os} = L_s - M_s$ is the stator winding inductance, R_s is the equivalent resistance of the stator windings. Those 2 values are important to know for the selected machine because they will be used afterwards in the controller.

It is important to set the current i_d to zero in the torque equation 7.5. This is not so easy to impose physically because the current i_d is not a physical value but a mathematical transformation resulting from three different physical current values. There is thus a need to control it virtually to zero to impose a correct set of physical currents.

Controller block diagram

Current loops: From the equations 7.6 and 7.7 in the dq reference frame, the block diagram of the machine and its controller can be constituted (Figure 7.7). The main complexity comes from the coupling between d and q circuits. The angular position of the rotor θ_{em} is obtained by position sensors.

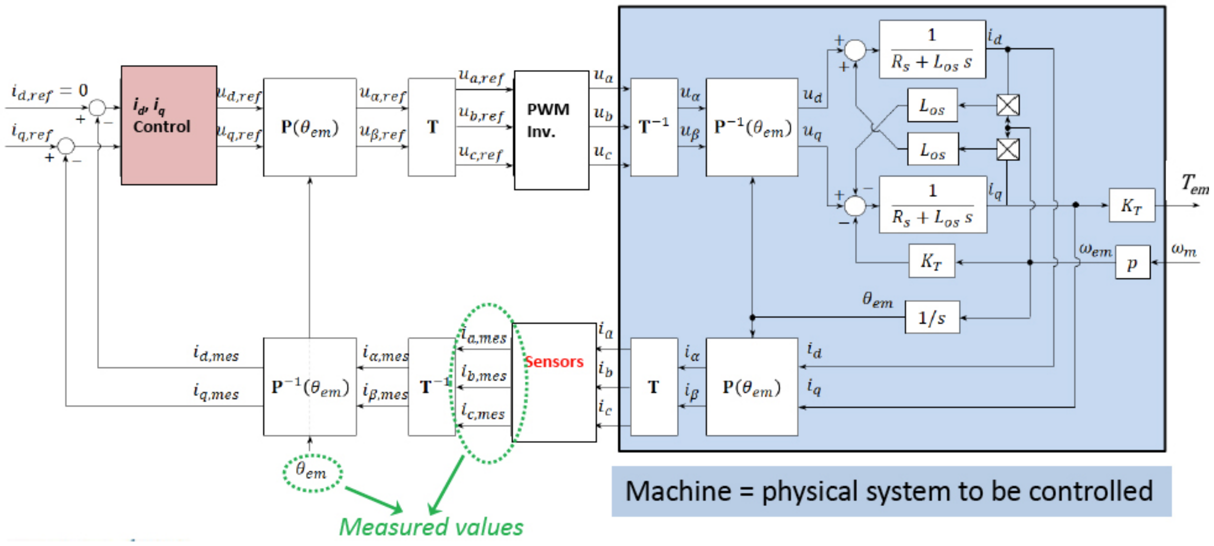

Figure 7.7: Block-diagram of the machine and its currents control loops in the dq reference frame. [29]

In order to simplify this block diagram and to decouple the q and d axis, we need to make some assumptions [29]:

1. The power electronics converter is assumed to be an amplifier gain G_u
2. The current measurement is ideal and equivalent to a pure gain G_i
3. The Park transformation and its inverse are considered as perfect and perform in a continuous way.
4. The inductance L_{os} is perfectly estimated.
5. The measurement of the rotational speed of the rotor is considered as ideal.

Once the q and d axis are decoupled, the block diagram can be separated into 2 independent control loops, one for each axis. The result is visible in Figure 7.8.

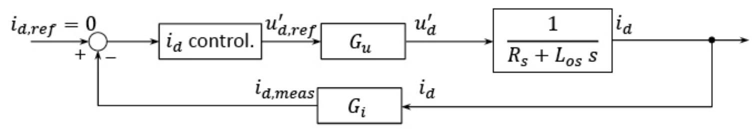

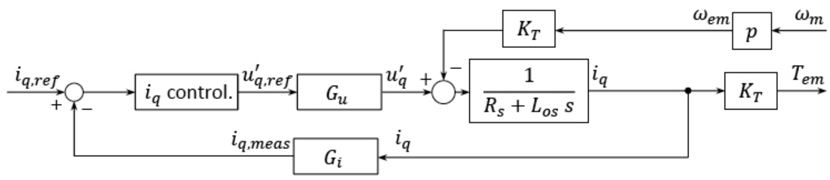

Figure 7.8: d and q axis decoupled control loops. [29]

By a compensation of the q-axis back EMF $\omega_{em}K_t$ and under the assumption that the torque constant k_t is perfectly estimated, the q axis block diagram can be further simplified (Figure 7.9).

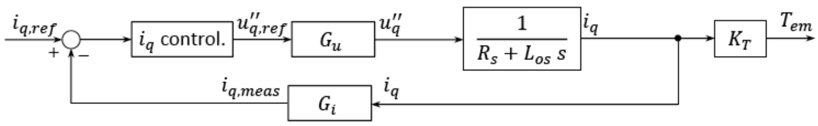

Figure 7.9: Simplified q-axis control loop by Kt perfectly estimated assumption. [29]

As mentioned earlier, the virtual reference voltage values extracted from our simplified control loops first have to be mathematically transformed back to physical voltage values before sending them to the PWM. This transformation has to be done in 2 steps:

1. From $[u''_{q,ref},\, u'_{d,ref}]$ to $[u_{q,ref},\, u_{d,ref}]$
2. From $[u_{q,ref},\, u_{d,ref}]$ to $[u_{a,ref},\, u_{b,ref},\, u_{c,ref}]$

The first step is done by applying some compensation terms corresponding to the inverse of the simplifications done to obtain the decoupled current loops :

$$u_{d,ref} = u'_{d,ref} - \frac{\omega_{em} L_{os} i_{q,mes}}{G_u G_i} \tag{7.8}$$

$$u_{q,ref} = u''_{q,ref} + \frac{\omega_{em} L_{os} i_{d,mes}}{G_u G_i} + \frac{\omega_{em} K_t}{G_u} \tag{7.9}$$

The second step is the application of Concordia and Park to come back in the physical reference frame (a,b,c).

$$\begin{pmatrix} u_{a,ref} \\ u_{b,ref} \\ u_{c,ref} \end{pmatrix} = \mathbf{TP}(\theta_{em}) = \begin{pmatrix} u_{d,ref} \\ u_{q,ref} \end{pmatrix} \tag{7.10}$$

Current controller: The controller box inserted in the current loops is a PI one (Figure 7.10). The structure is similar for the d and q current controller although the proportional kp and integral ki factors are different.

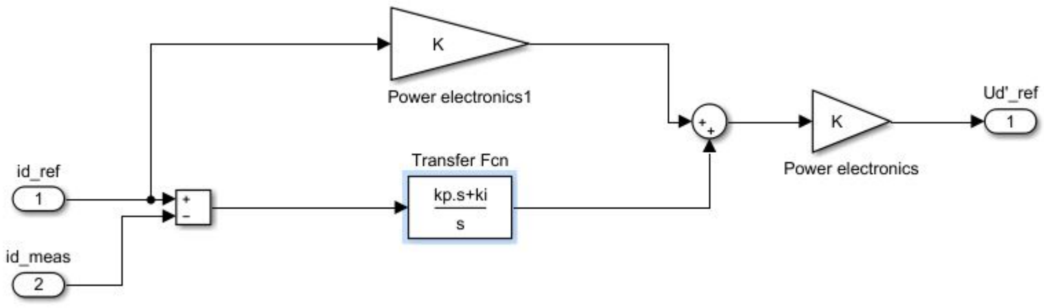

Figure 7.10: PI Controller box for the current loop

7.2.5 Synchronous machines and controller on the Airbus A320

As the objective of this master thesis is a global approach to the autonomous concept of an Airbus A320 on the ground, the choice of a specific synchronous machine is outside of the scope of this work. However a research of plausible machine was realized, performance wise only, to implement a model with realistic behaviors.

As expressed at the beginning of this chapter, the mechanical multibody simulation revealed that each electromechanical converter installed on each main wheel needs to provide a nominal torque of 14.3[kNm] at a speed of 15[m/s] ($\omega_{wheel} = v/R_{wheel} = 15/0.5842 = 25.676[rad/s]$). The power required is $P = T_{em} \cdot \omega = 377[kW]$. We have also seen that the power source for those four motors should be the APU providing 90kVA. Unfortunately it is impossible to find an synchronous machine of minimum 377kW that could respect the electrical power delivered by the APU.

A comparison with the green electrical taxi implemented on a A320 by EGTS, a partnership between Safran and Honeywell, shows a large difference in the specifications. The EGTS system is powered by 50kW electrical motors and is limited to a taxi speed of 20[kts] (10.29 [m/s] or 17.55 rad/s) translating into a torque of 2.85[kNm] per wheel [58]. This 7 times less than the torque required by the developed system. Moreover, most of electrical car synchronous motors have a rated output power at around 60 [kW]. It means that compact synchronous motors of those range of output power can be easily found on the market. [70]

After those research results, it was decided to modify our initial specifications based on the acceleration comfort criteria and to reduce the acceleration limit of $1.3[m/s^2]$ by a factor 7 to a value of $0.1857[m/s^2]$ to respect the APU power source capabilities. In addition, by reducing the speed to 20[kts] as the EGTS model, we see in Figure 7.11 that the torque needed does not exceeds 2[kNm]. The needed output power becomes 35.1[kW] which is even lower than the EGTS 50[kW] motors. Nevertheless, it takes more time to reach the reference speed in acceleration, hopefully in the deceleration phase the brakes are taking over.

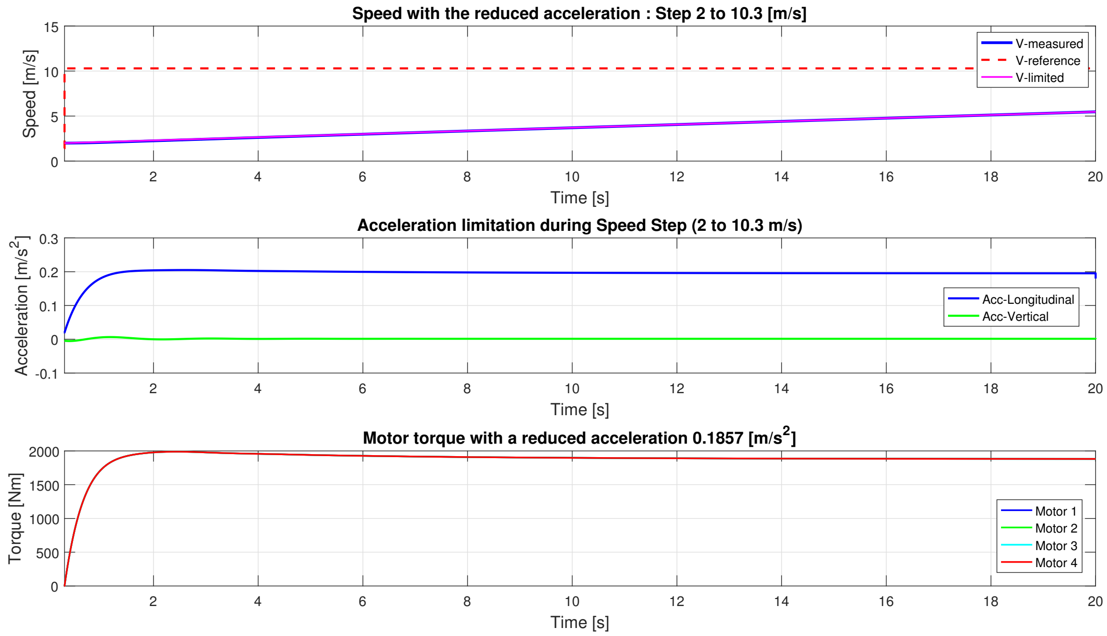

Figure 7.11: Speed and Torque curves of a reduced acceleration limit of $0.1857[m/s^2]$

Machine data

The chosen reference machine for the simulation is the SS13-236-4 with a nominal power of 37kW turning at 1500 [RPM] (157.08 [rad/s]) as seen in Figure 7.12. To adapt those motors onto the aircraft, it would be important to consider the following additional items :

1. A reducer 1:9 will be necessary to obtain a nominal speed of 17.45 [rad/s] (corresponding to 20[kts]) from the machine output shaft speed. The torque of the motor is multiplied by the reduction factor 9 to achieve the nominal wheel torque of 2.12 [kN]. The reducer induces mechanical power losses and its efficiency has to be considered.

2. A power electronic transformer is required by the machine to adjust the 115 V from the APU to the 350V.

3. Some saturation blocks are needed to avoid any overcurrent.

4. An improved APU generator power output is expected. The 4 electrical motors at their nominal power use 87.5 kVA of the 90kVA of the APU which does not leave much power for the remaining electrical components of the aircraft (e.g. the pilot instruments, the oven and the fridge in the cabin,...).

The data of the motor are represented in Figure 7.12 and are implemented in the model. Those data are used to implement the circuits illustrated in Figure 7.9 and 7.8. Even if we can consider the terminal motor resistance of $215m\Omega$ as R_s, the inductance data $L_{os} = L_s - M_s$ is missing. Because the value of terminal motor inductance is close to the generic L_{os} [28], we decided to take it as the L_{os} value, 4.675[mH]. In addition, the electrical time constant $\tau_e = \dfrac{L_{os}}{R_s} = 0.0217$ [s] remains low compared to the mechanical time constant of order 10^1 [s] as shown in Figure 6.22 of previous chapter.

Technical Data	Code Name	Unit	SS13-236-4	SS13-177-4	SS13-215-4
normal speed	N_n	rpm	1500	2000	2000
	P_n	kW	37	37	45
normal torque	M_n	Nm	235.57	176.68	214
normal voltage	V_n	V	350	350	350
normal current	I_n	Amp	62.5	62.8	76.4
max. speed	N_{max}	rpm	1750	2250	2250
zero speed torque	M_0	Nm	252.65	190.67	240.12
voltage constant	K_E	V/Krpm	170	226.66	170
torque constant	K_T	Nm/Amp	3.76	2.81	2.81
terminal motor resistance	R_{2ph}	ohm	0.215	0.171	0.14
terminal motor inductance	L_{2ph}	mH	4.675	3.674	3.191
Technical Data	Code Name	Unit	SS13-236-4	SS13-177-4	SS13-215-4
feedback device	-	-	Resolver	Resolver	Resolver
ambient temperature	-	˚C	0~40	0~40	0~40
insulative class	-	-	H	H	H
humidity	-	%	< 90	< 90	< 90
Dimension	Code Name	Measurement	SS13-236-4	SS13-177-4	SS13-215-4
motor length	K	mm	555	280	731
rotor size	D	mm	42	55	55
shaft keys width	M	mm	12	16	16

Figure 7.12: Datasheet synchrone machine SS13-236-4 [30]

Considering the power electronics converter and the current measurement as ideal, the amplifier gain G_u and the pure gain G_i are set to 1. This is also true for the power electronics K values in Figure 7.10.

7.2.6 Simulation Results

Machine controller adjustment

The controller used is a PI controller following the shape $C(s) = kp + \frac{ki}{s}$. The coefficients kp and ki are respectively 14 and 24 for the d-axis and q-axis current controllers. Those values were chosen to avoid any zero speed torque overshoot by the electromagnetic torque C_{em}. The time response is of order 10^{-3} seconds (in Figure 7.13). The integral coefficient ki helps to correct any steady-state error, the overshoot is corrected very quickly as seen in the virtual current i_q in Figure 7.13).

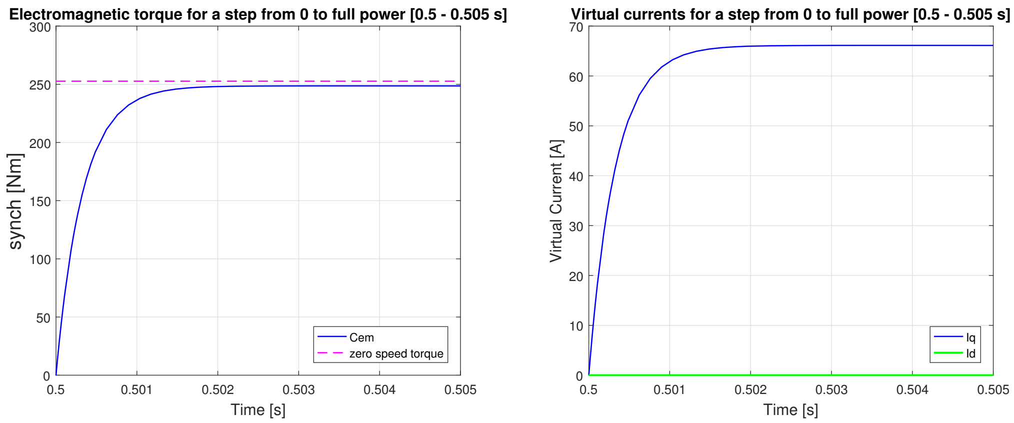

Figure 7.13: Zoom on the machine output torque (top) and the complete view of the virtual currents during an acceleration from no speed to full power, no torque situation

The virtual currents i_q and i_d are mathematically converted to physical values (i_a,i_b and i_c). The voltages are also converted, as explained earlier, and take the rotational speed of the rotor into account. The voltage amplitude is thus following this increasing speed behavior (Figure 7.14). In addition, the frequency of the currents and the voltages (amplitude and frequency too) is increasing all along the machine acceleration.

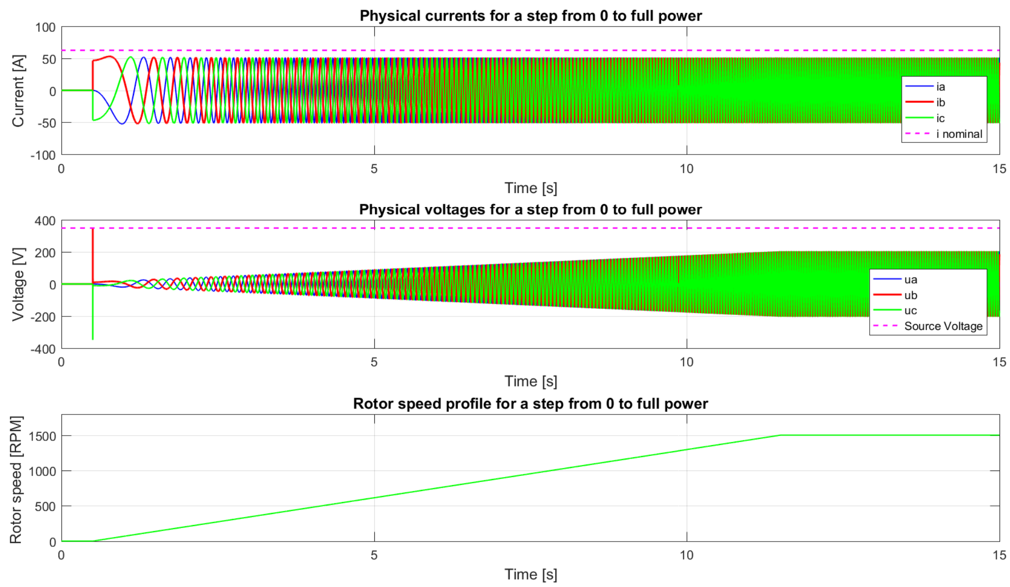

Figure 7.14: Physical currents and voltages in an acceleration from 0 to full power with the following speed step

Machine integrated in the aircraft model

The implementation of electrical motors in the Simulink model with the complete model is affecting the computation performances.

Nevertheless, the results obtained for a speed step from 6 to 7[m/s] on a straight track follows the correct speed slope as visible in Figure 7.15.

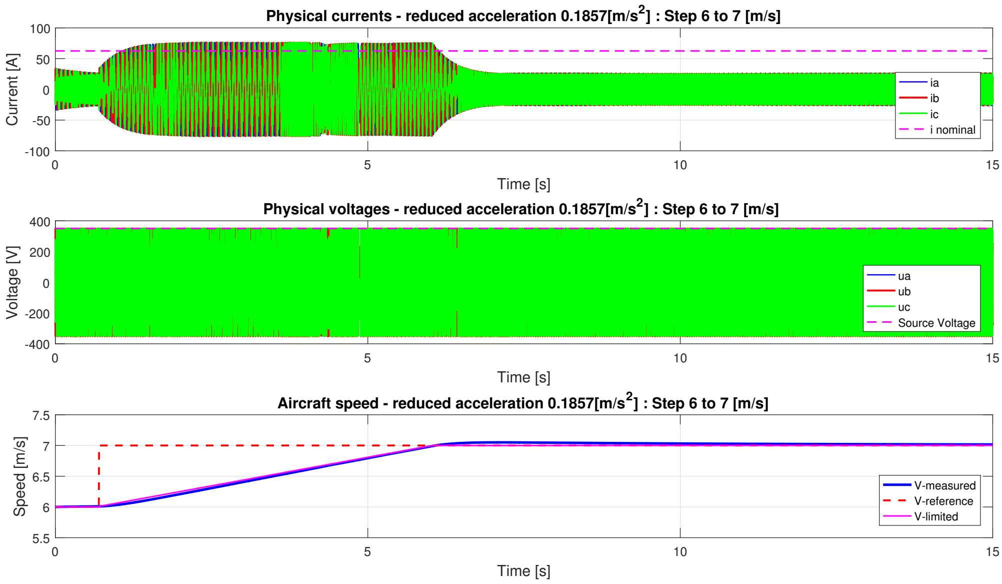

Figure 7.15: Physical currents and voltages during aircraft acceleration from 6 to 7[m/s]. Aircraft speed following

The torque (Figure 7.16) has an average value below the maximum one. Due to the quality of the results, this can be confirm by analyzing the torque reference in Figure 7.17 which is indeed below the maximum value. This can be done with the reasonable assumption that the controller acts in the same way as it was tested in subsection 7.2.6 (i.e. the torque reference is well followed by the controller).

Unfortunately, the physical currents are slightly exceeding their nominal values. To identify the cause, we can look at the reference torque after reducer and the rotor speed (both in blue in Figure 7.17). They never exceeds their limits which prove that the motor system receives the correct input. On the other hand, if we observe the shape of i_q in Figure 7.16, the quality of the results are not impressive. Because the physical currents are calculated from this virtual current, this could be the reason of the nominal current excess. This could also explain the higher than expected voltage values in comparison with the results obtained at maximum power in section 7.2.6.

Several attempt were made to improve the quality of the current i_q and the torque C_{em} without success. Among other things, the maximum time step of the simulation was reduced up to 1e-5[s], different solvers were used (e.g. ODE45,ODE15s).

Anyway, the implementation of the electrical motors control system on a Robotran/Simulink is working and do not affect the Vehicle Dynamic output.

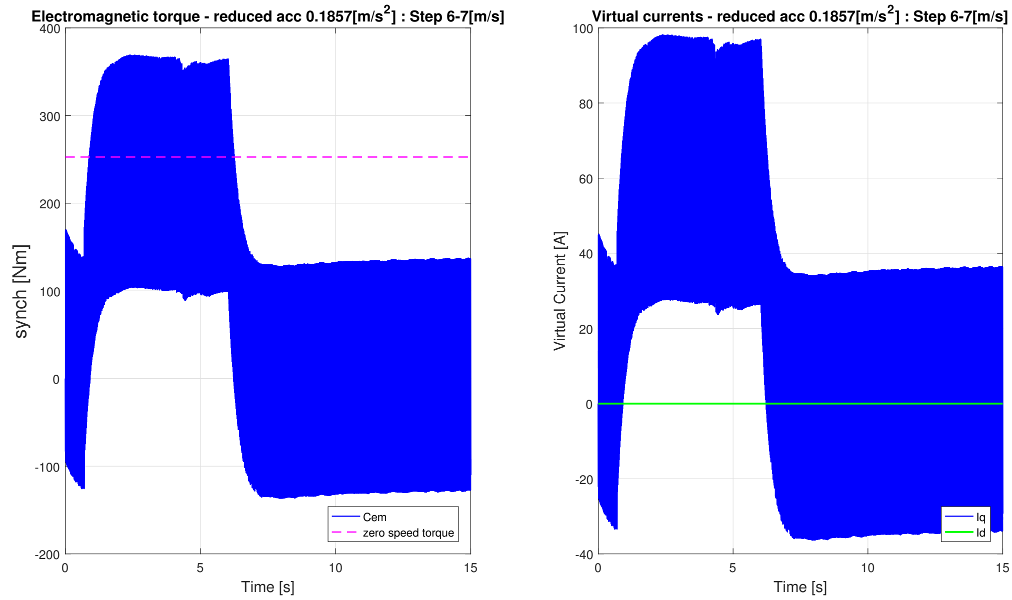

Figure 7.16: Physical currents and voltages in an acceleration from 0 to full power with the following speed step

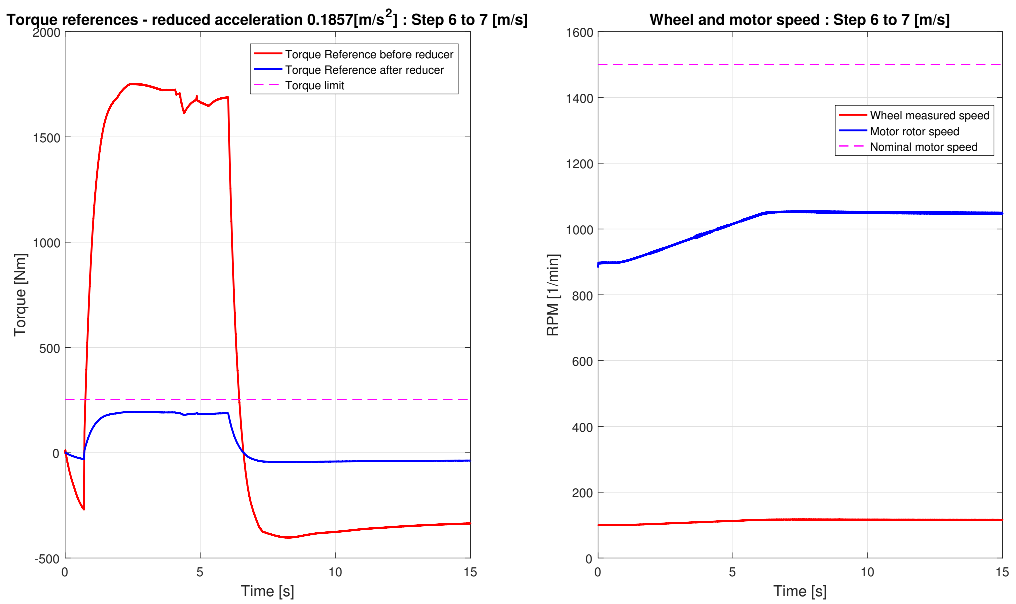

Figure 7.17: Reference torque (left) and rotational speed in RPM (right) before and after the reducer. The electrical motor limit values are indicated by the magenta dash line

Chapter 8 : Model analyses and operational consequences

In this chapter, a global summary of the results for the different models will be delivered, with their strengths and weaknesses and the impact these autonomous taxi and pushback systems have on current operations. A development is done on further potential improvements.

8.1 Model analyses

8.1.1 Model limitations

The biggest challenge to build this A320 model was the shortage in available non confidential data. This had an impact on the dynamic through the approximated mass distributions, bodies geometry and inertial matrices. Moreover, landing gears were simplified to dense cylindrical legs equipped with rim rods and wheels to improve computation performances.

In addition, the model does not include any parasite torque in the joints. In the physical world, any mechanical assembly has some. Neither is the aerodynamic drag implemented due to the complex shape of the aircraft. A full fluid mechanics analysis would be required.

Furthermore, the ground-wheel contact model of Bakker is not specific to aircraft tires. This car tire model was adapted to the aircraft mass.

Those model limitations have to be kept in mind while comparing mechanical, automation and electrical aspects of each aircraft design.

8.1.2 Comparison between designs

Trajectory capacities

In the current models : the directional nose wheel steering controlled system is a key factor for the Airbus A320 autonomous taxi and pushback. It should provide stability, robustness and controllabilty.

The trajectory controller mentioned in this study was designed for a directional nose wheel. Therefore, the implementation was the same on the electrical motor equipped aircraft and the jet engine one (i.e. first and second configurations).

However, a distinction can be done between the influence of the two propulsion technologies on the path tracking. On the one hand, the electrical motors are applying different torques on each main landing gear wheel in respect to the ICR. On the other hand, both jet engines are providing equal thrust at all time. Nevertheless, the influence is not significant as seen in Figure

8.1. Even with right engine shut down, the jet aircraft still follows the same track as the others. The trajectory system compensates for those perturbations.

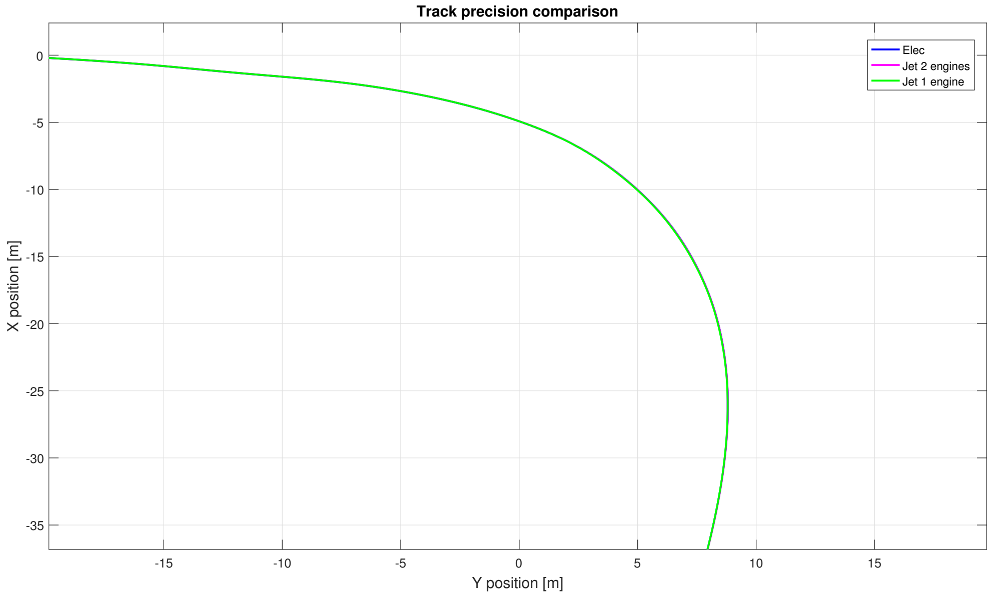

Figure 8.1: Speed and acceleration curves comparison for a 1[m/s] positive step

Concerning the free nose wheel equipped aircraft, unfortunately the mechanical analyses showed majors constraints for the implementation of a trajectory controller. Even with a castor wheel, the results were not significantly different. However, it was interesting to observe the caster angle influence on the stability. Another influencing factor is the center of gravity position which determines the normal force acting on the nose wheels.

For potential future developments :

1. The implemented track drawing based on a function of 4 points could be improved as it can be observed in Figure 8.2. A comparison is made between a polynomial of second order and another one of third order (as implemented in our system). We see that our system is better than the other one, however, we are still away for the perfect circle.

   Because taxiways are a set of straight lines and curves, a better and simpler method would be based on a database containing only 2 points (i.e. the start and the end of the track segment), an information about the curve radius and the center point of that curve. With those information and the equation of the circle, we could easily draw the black dashed line of Figure 8.2.

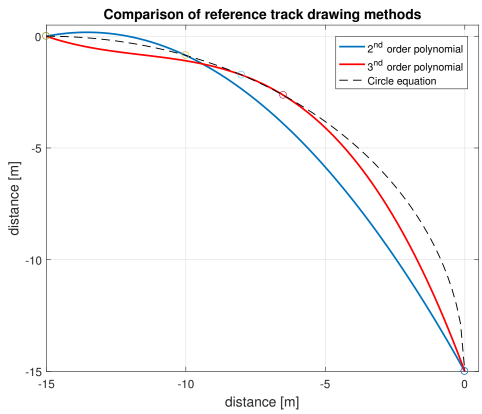

Figure 8.2: Comparison of draw track methods

2. In our model, the aircraft is comparing its current position with a reference position, the closest position on the track. This lateral deviation and the orientation error are used by the controller to come back on track. The system could be improved by implementing a feedforward system. The aircraft could determine which position he would reach at the next time step by assuming he is on the track. He could adjust the nose wheel orientation accordingly. The feedback loop, similar to the one implemented in our model, would inform the aircraft about its current error in position. The orientation of the nose wheel to reach the next point would use this information to correct the error [61]. This technique would normally improve stability due to its anticipation behavior and would potentially avoid rapid movement of the nose wheel.

3. To test the differential drive aircraft configuration (i.e. the free nose wheel design), another aircraft type should be used. It should be equipped with a classical landing gear type, i.e. with the main landing gear at the front and a free wheel under the tail (e.g. the DC3 in Figure 8.3). With this type of aircraft, the influence of the type of wheel, conventional or castor wheel, would be easier to study.

Figure 8.3: A classical landing gear more appropriate for differential drive design [2]

Speed controller

In the current model : even if the objective to keep a constant speed is identical, the controllers results of the first and the second configured aircraft are different. Indeed, due to the electrical power supply limitations of the APU, the acceleration of the electrical motor equipped aircraft is limited to 0.1857$[m/s^2]$ (in red in Figure 8.4). The jet engine powered aircraft acceleration is also affected due to the thrust restriction imposed to avoid potential jet blast hazards. The acceleration is increasing slowly but reaches a higher final value of about 1.4$[m/s^2]$ in regards with the initial 380[kW] high power electrical motor equipped aircraft curve (black) (i.e. the optimal electrical configuration that cannot be implemented due to APU power restriction). A value of 1.4$[m/s^2]$ is still reasonable for passenger comfort[64].

Consequently to the acceleration capability, the speed variation of the electrical aircraft is significantly slower than the jet engine one. If the objective is to have a comparable alternative to jet engine aircraft in regards with speed and acceleration, a research has to be done to provide high power electrical motors.

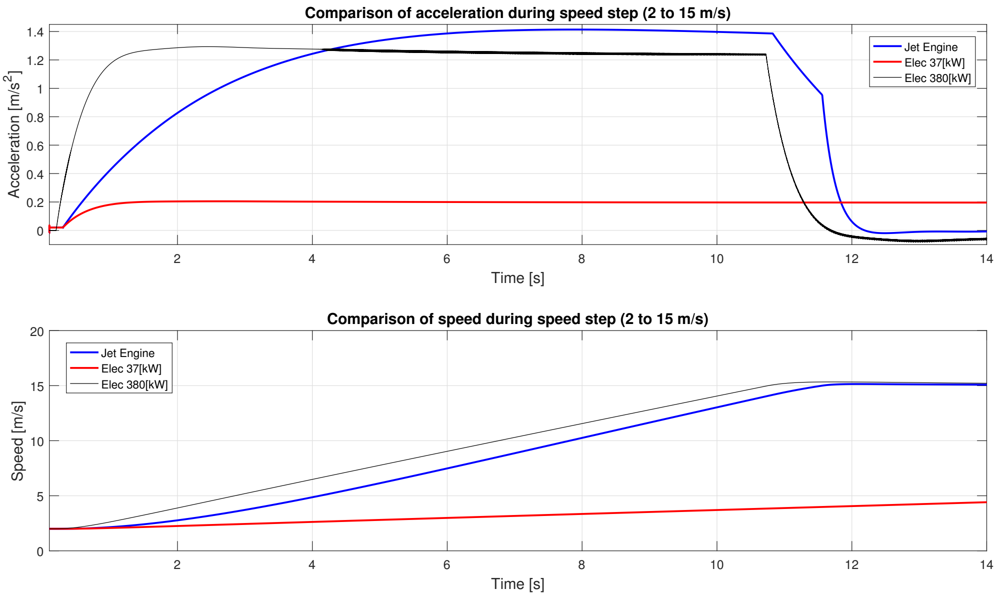

Figure 8.4: Acceleration and speed comparison between jet engines (blue), 37[kW] electrical motors (red), 380[kW] electrical motors (black).

It is interesting to observe the two step deceleration of the jet engine aircraft. The first step corresponds to the engine travelling to idle power, the second one highlights the activation of the brakes. These sequence is clearly visible in Figure 8.5.

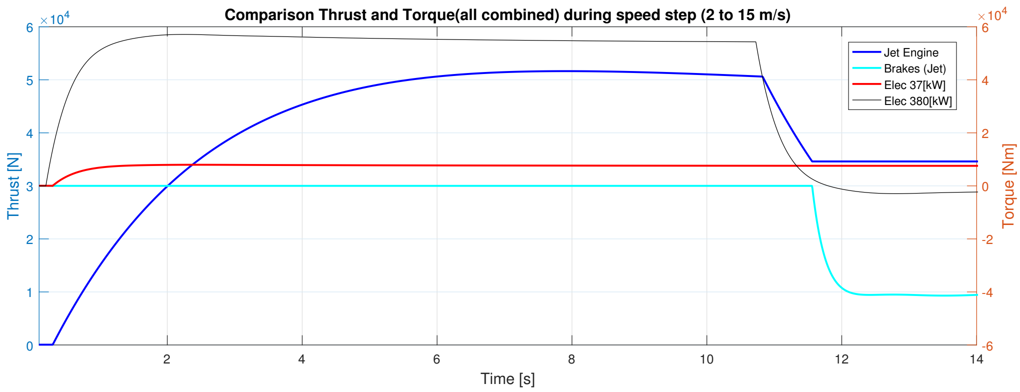

Figure 8.5: Thrust and torque comparison between jet engines (blue), jet brakes (cyan), 37[kW] electrical motors (red), 380[kW] electrical motors (black). The torques are all wheels combined.

As shown in Figure 8.5 on the right hand side of the graph, the jet engine aircraft is constantly using the brakes to maintain its speed constant (cyan). This is due to the constant thrust provided by the jet engines at idle thrust (blue). It means that the brake wear will become significant and that it could become a major maintenance and economical issue.

In opposition, the electrical motor equipped aircraft uses the brakes only for important decelerations. In other circumstances, its speed is maintained by the adjustment of the electrical motors torque. Due to the ability of the motors to turn both ways, the aircraft is also able to realize its pushback autonomously.

For potential future developments :

1. The acceleration limitation on the electrical motor powered aircraft is mainly due to the electrical output of the APU, 90kVA. Potential solutions to improve this acceleration constraint could be either to find higher performance 3-phase synchronous motors or to find a more powerful APU.

2. As we have seen, the brakes on the jet engine aircraft are often used in a continuous way. This would lead to significant wear and risk of overheat. Thus, another speed control system should be implemented. Nowadays, to avoid continuous brake application during taxi, pilots let the aircraft accelerate up to the maximum taxi speed (30[kts] in straight line) and then brake to slow down the aircraft until reaching a speed of around 10[kts]. To still be autonomous with that kind of braking method, a bang-bang speed controller could be implement, i.e. controller correcting the system when the upper or the lower limit is reached. However, the disadvantage of such a system is its constant speed variation which complicates ground traffic management on airports as it will be discussed in section 8.3.1.

8.1.3 Comparison summary

The major differences between the two viable aircraft configurations are the fuel consumption, the speed and acceleration performances and the ability to keep a constant speed. The other aspects are briefly stated in Table 8.1 and 8.2.

Advantages	Disadvantages
Aircraft jet engines not required	APU required
Less fuel consumption, less pollution, less noise	Complex power electronics (APU to motors)
Aircraft design untouched	Increased aircraft weight
Motors braking capability	Steering actuator to fit on actual system

Table 8.1: Electrical motor equipped aircraft : advantages and disadvantages

Advantages	Disadvantages
APU not required	Turbojet engines running
Lighter aircraft	High fuel consumption
Adaptative on older aircraft	Brake-Thrust controller
Aircraft design untouched	Steering actuator to fit on actual system

Table 8.2: Jet engine aircraft : advantages and disadvantages

8.2 Other possible next steps developments

8.2.1 Enhanced position determination

Up to now, the model presented is supposed to work with GPS localization (e.g. following a track which is a succession of geographic coordinates). This allows for a good level of accuracy - the US government guaranteeing an average user range error of $<$7.8m with 95 percent probability - but this precision is insufficient in the case we handle, even though Galileo system promise better performances [71].

As for smaller robots, it is good practice to compare data provided by different sensors to improve position accuracy. This comparison could be realized with a Karman filter[1] [72, 73].

A potential useful sensor (e.g. a camera) could detect the yellow line of the taxiway as well as the green and red led lights placed along the taxiway (see chapters 1 and 4). This sensor could be placed on the nose landing gear, between the two wheels, to be able to see the taxiway even in case of low visibility operations (i.e. to respect specifications of 3[m] visual range).

8.2.2 Collision avoidance

With the automated aircraft system developed in this project, a small step has to be made to implement a collision avoidance system.

Nowadays, this optimal awareness cannot be brought by human interventions, like visual controls, as pilots have difficulties estimating distances from the cockpit around them (e.g. wing tips) or even do not see parts of the aircraft from the cockpit (e.g the engines, the nose landing gear,...) [74, 75]. A famous example illustrating this fact is the collision that happened on a taxiway between an Air France A380 and a Delta Airlines regional jet. The left wing of the Airbus hit the backside of the small jet, which consequently did a 90° turn. Fortunately, only material damage occured and passengers were not wounded. [76, 77]

We thus need to integrate adequate sensors that allows to obtain a more accurate view of the position of the aircraft towards other ones, other ground vehicles and buildings. These information will then be processed to finally be used by our system, in order to automatically take corrective actions such as activating automatic emergency braking, following an avoidance track or adjusting speed.

Figure 8.6: Potential wings sensors [31]

This collision avoidance capability would be essential for improved traffic management during low visibility operations as we will discuss later on.

8.2.3 Interface pilots - autonomous system

All these additional information would need to be displayed to the pilots to be able to monitor the system and to intervene in case of emergency or system failure. Further, pilots should be able to give a taxi reference speed as they currently do with the *in flight* autopilot. The system could calculate the time the aircraft needs to reach a certain position along the track and even directly send it to ATC.

In this project we assumed that the taxiway database was providing a maximum taxiway reference speed. The pilot input would then be compared to that maximum speed and the lowest one would be taken.

8.2.4 Another energy source to power up the aircraft

If we go for the electrical motor solution, then the APU powers up the aircraft as it exists nowadays. However, some research is relentlessly carried on on new battery technologies. [78] It

[1] The Karman filter is an algorithm using several measurements which contain inaccuracies. It produces more accurate final value than the one captured by a single sensor.

will certainly tremendously evolve in the coming years and we can imagine that batteries will be able to store and provide more energy for aircraft along with retrieving and accumulating energy at landing for example.

8.3 Operational consequences on ground operations

An autonomous system, as described in this project, has multiple impacts on current ground operations that sometimes require some procedure adjustments. In the following section, we will quickly discuss some of them.

8.3.1 Enhanced traffic flow management

One of the major advantages of autonomous taxi operations is the reduction of waiting queues at the holding point (i.e. waiting at the beginning of the runway as shown in Figure 8.7). By knowing the exact time needed for taxiing, ATC could better manage traffic flow. The pushback clearance (or taxi clearance) can be given at a more appropriate time.

This solution can have a very strong impact if all aircraft on the airport are equipped with a taxi speed regulator.

Figure 8.7: London Heatrow traffic at the holding point [2]

8.3.2 Reduce delays and cancelled flights during low visibility operations

The collision avoidance system, with all the required sensors, increases safety drastically. It even offers the opportunity to decrease the distance between taxiing aircraft during low visibility operations. Nowadays, in such weather conditions, only one aircraft per taxiway section is allowed leading to important delays on busy airports (e.g. London Heathrow working at over 98% of its capacity during normal operations [79]).

Furthermore, the autonomous taxi system could allow to lower the landing minimum visibility from 75[m] to a few meters (e.g. 3[m] as mentioned in the specifications). This would reduce the number of in-flight diversions (i.e. change of destination airport in flight) and of cancelled flights.

8.3.3 Engine start before the flight

Nowadays, the engines are started during the pushback or on the parking stand to allow the aircraft to move on its own power for taxi. With our electrical powered aircraft, the taxi can be instantaneously done providing a gain of time (e.g. pushback and engine start up procedure takes about 5-10[min]). However, a minimum warm up time of 3 minutes is required before applying full take off power on the jet engines. This constraints us to start the engine during the taxi.

In case of jet engine start problem, the aircraft should be able to find a parking spot away from the departing one where maintenance personnel can assist pilots . One of the solution could be to use the de-icing platform, located close to the holding point on most of the airports.

Moreover, our system should be able to sustain the differential thrust provided during the sequential jet engine start (Engines are started one after the other) and the jet engine idle thrust while engines are started.

8.3.4 Positive ecological impact and fuel reduction

With the electrical motors, the engine fuel consumption will be reduced to an equivalent of 3[min] operation. To compare the electrical solution and the jet engine one on the base of a 15 minutes taxi time, we picked up data from another aircraft. We will also make the assumption that the whole taxi is done at idle power.

The airbus A300-600, an older and more powerful aircraft, has a jet engine fuel consumption of about 1.4[t/h] at idle power[2]. Thus, we obtain a fuel burned difference of 272[kg], which is equivalent to 340[L]. However, the APU consumption on this type of aircraft is about 284 [L/h] and has to be taken into account for the electrical motor equipped aircraft. We have to deduct an APU consumption of 71[L]. The difference between these two configurations is still 269[L].

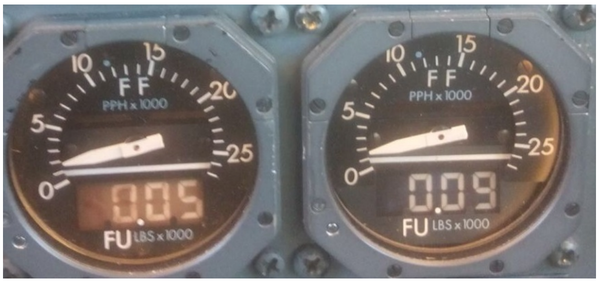

Figure 8.8: A300-600 : Fuel flow indicated by the arrows (x1000[lb/h]

Even if we approximate that the Airbus A320 consumption is half of the A300-600 one, the gain is still 134.5[L]. This has to be multiplied by the number of time the aircraft is taxiing (roughly 8 times per day for a short/medium haul aircraft).On top of that, with an improved traffic management, the fuel consumption can be further reduced by shorter taxi period and waiting time.

The EGTS program was announcing fuel saving up to $200,000 per aircraft per year with carbon emissions reduction by 75% and nitrogen oxide emissions drop by 50% [58].

[2]Data picked up directly from real cockpit information. See Figure 8.8.

Conclusion

Across the various aspects studied in this work, we come to the conclusion that automating an Airbus A320 for its taxi and pushback sequences is possible. This also means it could potentially be extended to any kind of existing plane.

Among the three potential aircraft configurations initially introduced, two emerged as being really viable for the automation purposes we had. The first one, called the *electrical motor equipped aircraft*, is a directional nose wheel complemented by 4 electrical motors powering the main gear wheels. The second one, referenced as the *jet engine equipped aircraft*, is constituted by a directional nose wheel as in the first solution, but where the necessary thrust is provided by the turbo jet engines of the plane.

Both solutions have their advantages and drawbacks. Only the electrical option allows for an automated pushback. However, this solution currently constraints the aircraft ground acceleration as it would be served by the on-board electrical power source, the APU, limited to 90kVA. As an immediate effect, the speed would also be limited to 20[kts] max. This first configuration would also require mechanical adjustments to install synchronous machines on the main landing gears, the modernization and optimization of procedures and an intensive user training. Main advantages are clear on this side : fuel saving and C02 emission reductions.

On the other side, the jet engine configuration does not require many mechanical adjustments, the total mass of the aircraft and impact on ground operations would not be significant. For those reasons, we could expect this option to be less expensive than the first one, opening opportunities for existing planes to test it in the short run. However, as a constant speed control is not recommended due to the constant brake applications counteracting the idle thrust of the jet engines, this thus limits the potential traffic management improvements.

Generally speaking, these 2 solutions already offer a common ground of benefits which encompass the continuity of air traffic in low visibility conditions, an improved air traffic sequencing and enhanced safety results, by a better control on the flow of planes navigating through airports. Because a conversion towards the electrical motor option is hard to imagine on existing planes, both configurations could be exploited, respectively for existing and new planes to come.

As we have seen, managing air traffic and flow on the ground have become key levers for airports to answer to the rising demand of carrying passengers and cargo. This automation of part of usual flight sequences could contribute to answer this need. However, before going further in the implementation of such a solution, we would advice to dig into several subjects in more details, including in-depth cost/benefit analyses, automation fine-tuning, electrical design options on the market and interest from the manufacturers and airports.

We hope you enjoyed the flight... And thank you again for flying UCLouvain!

Appendix

A.1 Nose wheel steering logic Airbus A320

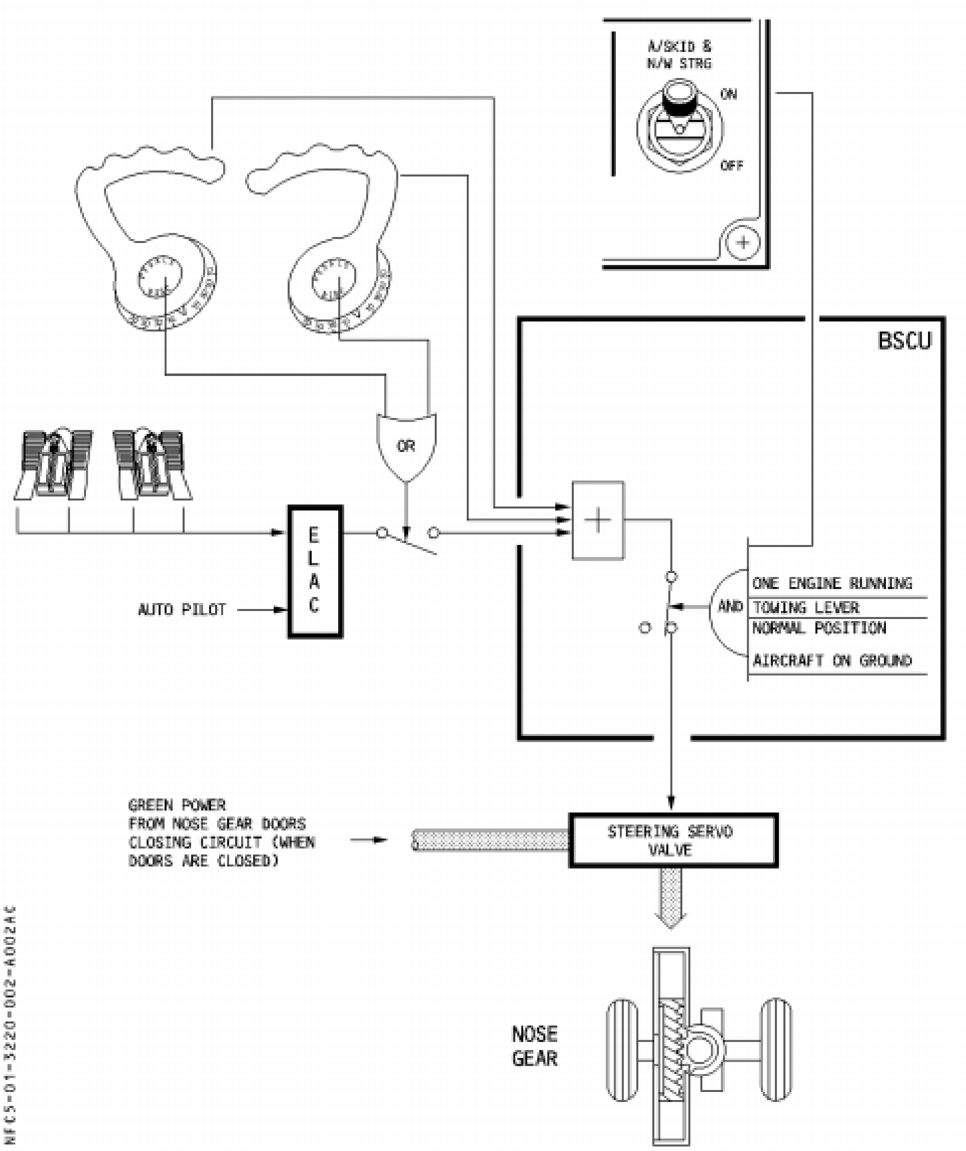

Figure A.1: Nose wheel steering schematics Airbus A320 [5]

Bibliography

[1] Airliners, aviation photography. http://www.airliners.net, Accessed on 18 of November 2016.

[2] Google image. https://lh4.googleusercontent.com, Accessed on 10 of February 2017.

[3] Jeppensen jepview london heathrow charts. http://www.pentekesti.com/sites/default/files/Charts/eggl.pdf, Accessed on 17 of February 2016.

[4] Air services australia - what is an instrument landing system. http://www.airservicesaustralia.com/projects/gold-coast-ils/what-is-an-instrument-landing-system/, Accessed on 22 of February 2016.

[5] A320 fcom landing gear. http://www.smartcockpit.com/aircraft-ressources/A320-Landing_Gear.html, Accessed on 15 of November 2016.

[6] Cockpit a320 side stick and hand wheel steering. http://i.stack.imgur.com/UxP7a.jpg, Accessed on 17 of February 2016.

[7] Heathrow embarks on holdover time pilot. http://airportfocusinternational.com/heathrow-embarks-on-holdover-time-pilot/, Accessed on 06 of April 2017.

[8] Helsinki oaci airport chart. http://www.canadianclassicairlines.com/CPC/index.php/schedules/brief/37685, Accessed on 06 of April 2017.

[9] Autobrake - rejected takeoff. http://www.flaps2approach.com/journal/2015/2/1/rejected-takeoff-rto-review-and-procedures.html, Accessed on 07 of April 2017.

[10] Eurotest enquête des automobile clubs sur le système de sécurité esp. https://www.automobile-club.org/actualites/la-vie-de-l-aca/eurotest-enquete-des-automobile-clubs-sur-le-systeme-de-securite-esp, Accessed on 07 of April 2017.

[11] Caster angle. https://www.quora.com/How-caster-angle-affects-to-the-vehicle-dynamics, Accessed on 7 of May 2017.

[12] Fisette Paul. *LMECA 2215 - Wheel/road contact Lecture - Vehicle Dynamics*. UCL, 2016.

[13] Motors for electric cars - electronic products. tp://www.airbus.com/fileadmin/media_gallery/files/tech_data/Pavement/HTPT_final_report_Aug2010.pdf, Accessed on 4 of December 2016.

[14] Abdurrhman A. Alroqi at Embry-Riddle Aeronautical Univsersity. Comparison of aircraft tire wear with initial wheel rotational speed. commons.erau.edu/cgi/viewcontent.cgi?article=1043&context=ijaaa, Accessed on 15 of October 2016.

[15] Georg Rill. *Road Vehicle Dynamics, Fundamentals and modeling*. Ground Vehicle Engineering Series. CRC Press, 2012.

[16] H. Olsson K.J. Åström C. Canudas de Wit M. Gäfvert P. Lischinsky. Friction models and friction compensation. http://cats-fs.rpi.edu/~wenj/ECSE446S06/astrom_friction.pdf, Accessed on 26 of December 2016.

[17] Models of friction. http://www.mogi.bme.hu/TAMOP/robot_applications/ch07.html#ch-8.4.1.1, Accessed on 27 of Mai 2017.

[18] Modeling multibody systems with robotran. http://www.robotran.be/images/files/Robotran_basics.pdf, Accessed on 8 of May 2017.

[19] Comfortable takeoff and soft landing - suspension. http://rostec.ru/en/research/tecnology/4513868, Accessed on 8 of May 2017.

[20] Egts train principal électrique. https://www.lavionnaire.fr/SiteImgTrain/TrainElectRouePrincipale.png, Accessed on 3 of May 2017.

[21] Cornerstone robotics. http://cornerstonerobotics.org/illustrator.php, Accessed on 11 of May 2017.

[22] Dochain Denis. *INMA 1510 - UCL - Syllabus d'Automatique Lineaire*. UCL, 2010.

[23] Top gear - bbc - jet blast experiments. https://www.youtube.com/watch?v=ZJ9uWsvR1l0, Accessed on 31 of Mai 2017.

[24] What's the difference between brush dc and brushless dc motors? http://electronicdesign.com/electromechanical/what-s-difference-between-brush-dc-and-brushless-dc-motors, Accessed on 21 of April 2017.

[25] Stator and rotor induction machine - encyclopedia-magnetica. http://www.encyclopedia-magnetica.com/lib/exe/fetch.php/stator_and_rotor_of_induction_motor_magnetica.jpg, Accessed on 21 of April 2017.

[26] Youtube - how does an induction motor work. https://www.youtube.com/watch?v=LtJoJBUSe28, Accessed on 22 of April 2017.

[27] Youtube - working of synchronous motor. https://www.youtube.com/watch?v=Vk2jDXxZIhs, Accessed on 22 of April 2017.

[28] Bruno Dehez. *Lecture 3 - Space vector transformations - LELEC 2313 UCL*. UCL Moodle, 2015.

[29] Emmanuel De Jaeger Bruno Dehez. *Lecture - Control of synchronous machine - LELEC 2313 UCL*. UCL Moodle, 2015.

[30] Super success technology corporation: Synchronous machine. http://www.servotech.com.tw/, Accessed on 19 of Mai 2017.

[31] Tnooz - could these five tech concepts change aviation forever? https://www.tnooz.com/article/could-these-five-tech-concepts-change-aviation-forever/, Accessed on 6 of June 2017.

[32] Icao annex 6 - operation of aircraft, chapter 1 : Definition. http://www.verifavia.com/bases/ressource_pdf/299/icao-annex-6-part-i.pdf, Accessed on 21 of February 2016.

[33] Transport distribution - face à la croissance du traffic aérien : les grands projets d'infrastructures des aéroports. http://transport.sia-partners.com/face-la-croissance-du-trafic-aerien-les-grands-projets-dinfrastructures-des-aeroports, Accessed on 7 of June 2017.

[34] Icao - traffic growth and airline profitability were highlights of air transport in 2016. https://www.icao.int/Newsroom/Pages/traffic-growth-and-airline-profitability-were-highlights-of-air-transport-in-2016.aspx, Accessed on 7 of June 2017.

[35] International air transport association - new iata passenger forecast reveals fast-growing markets of the future. http://www.iata.org/pressroom/pr/Pages/2014-10-16-01.aspx, Accessed on 7 of June 2017.

[36] International civil aviation organization - long-term traffic forecasts. https://www.icao.int/safety/ngap/NGAP8$%$20Presentations/ICAO-Long-Term-Traffic-Forecasts-July-2016.pdf, Accessed on 7 of June 2017.

[37] Icao - safety report 2016. https://www.icao.int/safety/Documents/ICAO_SR$%$202016_final_13July.pdf, Accessed on 7 of June 2017.

[38] Aviation alphabet. http://www.aviationalphabet.com/, Accessed on 17 of February 2016.

[39] Bbc news - air france a380 plane collides with jet at jfk. http://www.bbc.com/news/world-us-canada-13054205, Accessed on 22 of February 2016.

[40] Airbus - fly by wire. http://www.airbus.com/innovation/proven-concepts/in-design/fly-by-wire/, Accessed on 06 of April 2017.

[41] Aircraft ground de-icing/anti-icing operations - icao icao requirements and guidance. http://www.icao.int/safety/airnavigation/OPS/Pages/Aircraft-Ground-De-IcingAnti-Icing-Operations.aspx, Accessed on 06 of April 2017.

[42] Holdover time guidance - canada. http://www.tc.gc.ca/eng/civilaviation/standards/commerce-holdovertime-menu-1877.htm, Accessed on 06 of April 2017.

[43] Professor Dr. Valentin L. Popov. *Contact Mechanics and Friction, Physical Principles and Applications*. Springler, 2010.

[44] Talekar N. B. Lindsley, N. J. A tire model for air vehicle landing gear dynamics. http://web.mscsoftware.com/support/library/conf/adams/na/2000/18_USAF_tire_landing_gear.pdf, Accessed on 17 of December 2016.

[45] Karl Johanastrom Carlos Canudas de Wit. Revisiting the lugre friction model. http://ieeexplore.ieee.org/document/4653109/, Accessed on 17 of December 2016.

[46] Revisiting the lugre friction model.

[47] Experimental comparison of five friction models on the same test-bed of the micro stick-slip motion system. http://www.mech-sci.net/6/15/2015/ms-6-15-2015.pdf, Accessed on 27 of Mai 2017.

[48] Pacejka magic formula. http://www.edy.es/dev/docs/pacejka-94-parameters-explained-a-comprehensive-guide/, Accessed on 4 of May 2017.

[49] Robotran - symbolic generator of multibody systems. http://www.robotran.be/, Accessed on 20 of September 2016.

[50] Steiner theorem - parallel axis theorem. http://hyperphysics.phy-astr.gsu.edu/hbase/parax.html, Accessed on 30 of Mai 2017.

[51] Ode 45 mathworks. https://de.mathworks.com/help/matlab/ref/ode45.html, Accessed on 19 of Mai 2017.

[52] Lagrange multipliers introduction. https://fr.khanacademy.org/math/multivariable-calculus/applications-of-multivariable-derivatives/constrained-optimization/a/lagrange-multipliers-single-constraint, Accessed on 8 of May 2017.

[53] Masse volumique. http://www.deleze.name/~marcel//sec2/applmaths/pression-altitude/masse_volumique.pdf, Accessed on 20 of September 2016.

[54] A320 fcom1 chapter limitations. www.smartcockpit.com/aircraft-ressources/A_0_Limitations.html, Accessed on 19 of October 2016.

[55] Easa certification leap engines. https://www.easa.europa.eu/system/files/dfu/EASA$%$20E$%$20110$%$20TCDS$%$20Issue$%$203_LEAP_1A_20161107_1.0.pdf, Accessed on 19 of November 2016.

[56] Goodyear 467q02-3 flight leader 46x17r20-30 ply 225 mph tubeless aircraft tire for a320. http://www.skygeek.com/goodyear-467q02-3-tire-46x17r20-30-flt-rad-tl-308-017-020.html, Accessed on 8 of May 2017.

[57] Icao - aerodrome design manual part 2. https://www.bazl.admin.ch/dam/bazl/fr/dokumente/Fachleute/Flugplaetze/ICAO/icao_doc_9157_aerodromedesignmanual-part2.pdf.download.pdf/icao_doc_9157_aerodromedesignmanual-part2.pdf, Accessed on 30 of Mai 2017.

[58] Aviation week - egts program. http://aviationweek.com/awin/honeywellsafran-joint-venture-tests-electric-taxiing, Accessed on 31 of Mai 2017.

[59] Electric green taxiing system (egts) for aircraft. http://tec.ieee.org/newsletter/march-april-2014/electric-green-taxiing-system-egts-for-aircraft, Accessed on 3 of May 2017.

[60] Flight global : Honeywell and safran halt electric taxi project egts. https://www.flightglobal.com/news/articles/farnborough-honeywell-and-safran-halt-electric-tax-427400/, Accessed on 3 of May 2017.

[61] Richard M. Murray Karl Johan Aström. *Feedback Systems*. Princeton University Press, 2008.

[62] Time response of second order systems - university of lisboa. https://fenix.tecnico.ulisboa.pt/downloadFile/3779580204927/2ndorderresponseMSD.pdf, Accessed on 28 of Mai 2017.

[63] Matlab : Find minimum of single-variable function on fixed interval. https://de.mathworks.com/help/matlab/ref/fminbnd.html, Accessed on 9 of April 2017.

[64] Passenger stability within moving railway vehicles: Limits on maximum longitudinal acceleration - table 1. https://link.springer.com/article/10.1007/s40864-015-0012-y, Accessed on 17 of April 2017.

[65] Magnetic forces. http://hyperphysics.phy-astr.gsu.edu/hbase/magnetic/magfor.html, Accessed on 17 of May 2017.

[66] Carbon brush wear in dc motors and generators caused by silicone. http://www.idcon.com/resource-library/articles/best-practices/1028-carbon-brush-wear-in-dc-motors-and-generators-caused-by-silicone.html, Accessed on 17 of May 2017.

[67] Moteur électrique asynchrone - wehicles. https://wehicles.com/wiki/moteur_asynchrone, Accessed on 21 of April 2017.

[68] Electric generator. http://eolienne.f4jr.org/generateur_electrique, Accessed on 19 of May 2017.

[69] A320 fcom electrical. http://www.smartcockpit.com/docs/A320-Electrical.pdf, Accessed on 15 of Mai 2016.

[70] Motors for electric cars - electronic products. http://www.electronicproducts.com/Electromechanical_Components/Motors_and_Controllers/Motors_for_electric_cars.aspx, Accessed on 1 of June 2017.

[71] Us government - gps performance accuracy. http://www.gps.gov/systems/gps/performance/accuracy/, Accessed on 4 of June2017.

[72] Karman filter - wikipedia. https://en.wikipedia.org/wiki/Kalman_filter, Accessed on 4 of June 2017.

[73] Scaramuzza Siegwart, Nourbakhsh. *Autonomous Mobile Robots, second edition.* MIT, 2004.

[74] International airport review - follow the greens. https:https://www.internationalairportreview.com/news/16997/follow-the-greens/, Accessed on 4 of June 2017.

[75] Meggitt private company - aircraft security and safety. https://www.meggitt.com/capabilities/aerospace/aircraft-security-and-safety, Accessed on 4 of June 2017.

[76] Video - a380 airfrance collides with small aircraft. https://www.youtube.com/watch?v=5p1nZPAH1sA, Accessed on 4 of June 2017.

[77] Ntsb - air france flight 7 wing clipping incident with comair flight 293. https://www.ntsb.gov/investigations/pages/2011_jfk_airport_ny.aspx, Accessed on 4 of June 2017.

[78] Batteries and advanced airplines. http://787updates.newairplane.com/787-Electrical-Systems/Batteries-and-Advanced-Airplanes, Accessed on 4 of June 2017.

[79] Lhr - london heathrow. https://en.wikipedia.org/wiki/Heathrow_Airport, Accessed on 4 of June 2017.

Rue Archimède, 1 bte L6.11.01, 1348 Louvain-la-Neuve **www.uclouvain.be/epl**